JAEA-Conf

Proceedings of the 2007 Symposium on Nuclear Data
November 29-30, 2007, RICOTTI, Tokai, Japan

(Eds.) Taira HAZAMA and Tokio FUKAHORI

Reactor Physics Analysis and Evaluation Group
Advanced Nuclear System Research and Development Directorate

November 2008

Japan Atomic Energy Agency 日本原子力研究開発機構

Proceedings of the 2007 Symposium on Nuclear Data

November 29-30, 2007, RICOTTI, Tokai, Japan

(Eds.) Taira HAZAMA and Tokio FUKAHORI[+]

FBR System Technology Development Unit
Advanced Nuclear System Research and Development Directorate
Japan Atomic Energy Agency
Oarai-machi, Higashiibaraki-gun, Ibaraki-ken

The 2007 Symposium on Nuclear Data was held at RICOTTI in Tokai-mura, Ibaraki-ken, Japan, on 29th and 30th of November 2007, with about 80 participants. Nuclear Data Division of Atomic Energy Society of Japan organized this symposium with cooperation of North Kanto Branch of the society.

In the oral sessions, 10 papers were presented on topics of JEDNL-4, experiments, evaluations, applications, and research activity in China. In the poster session, presented were 12 papers concerning experiments, evaluations, benchmark tests, and so on. Tutorials on nuclear data, which were for cross section data creation process and PHITS code, were also done. Major part of those presented papers is compiled in this proceedings.

[+] Division of Nuclear Data and Reactor Engineering, Nuclear Science and Engineering Directorate

2007 年度核データ研究会報文集

2007 年 11 月 29～30 日、テクノ交流館リコッティ、東海村

日本原子力研究開発機構

次世代原子力システム開発部門　FBR 要素技術ユニット

（編）羽様　平、深堀　智生[+]

2007 年度核データ研究会が 2007 年 11 月 29 日と 30 日の両日、東海村のテクノ交流館リコッティにおいて約 80 名の参加の下で開催された。この研究会は日本原子力学会核データ部会の主催、日本原子力学会北関東支部の協力により開催されたものである。

口頭発表では、JENDL-4、核データの測定、評価、利用、および中国における核データ研究等について 10 件報告された。ポスター発表では、核データの測定、評価、およびベンチマークテスト等について 12 件報告された。また、断面積導出過程やPHITS コードの利用についてのチュートリアルも実施された。本報文集はそれらの論文の一部をまとめたものである。

大洗研究開発センター（駐在）：〒311-1393　茨城県東茨城郡大洗町成田町 4002
[+]原子力基礎工学研究部門 核工学・炉工学ユニット

Program Committee

Masayuki IGASHIRA (Chairman)	Tokyo Institute of Technology
Makoto ISHIKAWA (Co-chairman)	Japan Atomic Energy Agency
Mamoru BABA	Tohoku University
Go HIRANO	TEPCO Systems Co. (TEPSYS)
Shin-ya KOSAKA	TEPCO Systems Co. (TEPSYS)
Kazumi IKEDA	Mitsubishi Heavy Industries Ltd.
Hideo HARADA	Japan Atomic Energy Agency
Hiroshi NAKASHIMA	Japan Atomic Energy Agency
Tokio FUKAHORI	Japan Atomic Energy Agency
Yosuke IWAMOTO	Japan Atomic Energy Agency
Akira ICHIHARA	Japan Atomic Energy Agency
Osamu IWAMOTO	Japan Atomic Energy Agency
Nobuyuki IWAMOTO	Japan Atomic Energy Agency
Satoshi KUNIEDA	Japan Atomic Energy Agency

プログラム委員会

井頭　政之（委員長）	東京工業大学
石川　眞（副委員長）	日本原子力研究開発機構
馬場　護	東北大学
平野　豪	テプコシステムズ(株)
小坂　進矢	テプコシステムズ(株)
池田　一三	三菱重工業(株)
原田　秀郎	日本原子力研究開発機構
中島　宏	日本原子力研究開発機構
深堀　智生	日本原子力研究開発機構
岩元　洋介	日本原子力研究開発機構
市原　晃	日本原子力研究開発機構
岩本　修	日本原子力研究開発機構
岩本　信之	日本原子力研究開発機構
国枝　賢	日本原子力研究開発機構

This is a blank page.

Contents

目次

1. Introduction

The 2007 Symposium on Nuclear Data was held at RICOTTI at Tokai-mura, Ibaraki-ken, Japan, on 29th and 30th of November 2007, with about 80 participants. Nuclear Data Division of Atomic Energy Society of Japan organized this symposium with cooperation of North Kanto Branch of the society.

In the oral sessions, 10 papers were presented on topics of JENDL-4, experiments, evaluations, applications, and research activity in China. In the poster session, presented were 12 papers concerning experiments, evaluations, benchmark tests, and so on. Tutorials on nuclear data, which were for cross section data creation process and PHITS code, were also done. Major part of those presented papers is compiled in this proceedings.

Program of Symposium on Nuclear Data 2007

Nov. 29 (Thr.)
10:20-10:30

1. Opening Address　　　　　　　　　　　　　　　　　　　　　　T. Yoshida (Musashi Tech.)

10:30-12: 00

2. Development of JENDL-4　　　　　　　　　　　　　　　　Chaired by M. Igashira (TIT)

　2.1 Present status of JENDL-4 [20+10]　　　　　　　　　　　　　　K. Shibata (JAEA)

　2.2 Nuclear Data Evaluation for MA [20+10]　　　　　　　　　　　T. Nakagawa (JAEA)

　2.3 Integral test for JENDL-4 [20+10]　　　　　　　　　　　　　　K. Okumura (JAEA)

13:00-14:45

3. Nuclear Data Tutorial (1)

　Measurement of neutron cross sections − from obtaining raw data to deriving cross sections −

　　　　　　　　　　　　　　　　　　　　　　　　　　　　　　　H. Harada (JAEA)

15:00-16:45

4. Nuclear Data Tutorial (2)

　Use of PHITS　　　　　　　　　　　　　　　　　　　　　　　　K. Niita (RIST)

16:45-17:00

5. Q&A and Anquete

Nov. 30 (Fri.)

10:20-12:00

6. Poster Presentation

13:00-14:30

7. Domestic Nuclear Data Measurements and Evaluations   Chaired by M. Ishikawa (JAEA)

   7.1 Neutron cross section measurement of MA [20+10]   H. Harada (JAEA)

   7.2 Nuclear data measurement project at J-PARC MLF [20+10]   Y. Kiyanagi (Hokkaido U.)

   7.3 Evaluation of covariances for self-shielding factor and its temperature coefficients [20+10]

                           N. Ohtsuka (JAEA)

14:50-16: 40

8. Nuclear Data Activities   Chaired by T. Fukahori (JAEA)

   8.1 Measurement plan for the (n, γ) cross sections using surrogate reaction at JAEA [20+10]

                           H. Makii (JAEA)

   8.2 Nuclear data activities at China [20+10]   Sun Weili (IAPCM)

   8.3 Recent nuclear data needs from innovative reactor design [20+10]   M. Ishikawa (JAEA)

   8.4 Status of LWR fuel design and future usage of JENDL [15+5]   T. Ito (NFI)

16:40-17:00

9. Poster Award and Closing Address   M. Igashira (TIT)

Poster Presentation
10:20-12:00

P1. Motivation for the determination of the ^{244}Cm effective neutron capture cross-section

S. Nakamura (JAEA)

P2. Measurement of activation cross section of (n, p) and (n,α) reactions in the energy range of 3.5 to 5.9 MeV using a deuterium gas target

M. Furuta MASATAKA (Nagoya U.)

P3. Neutron-induced proton production from carbon at 175 MeV

M. Hayashi (Kyushu U.)

P4. Study of a new crystal array detector to measure double differential cross sections of proton-actinide reactions in 600-MeV region

Y. Koba (Kyushu U.)

P5. Nucleon Optical Potentials for the CDCC analysis of Deuteron Elastic Scattering from ^{6,7}Li

Ye Tao (Kyushu U.)

P6. Developments of a simulation model describing both elastic and inelastic scatterings

Y. Fukui (Kyushu U.)

P7. Paramagnetic Scattering of Neutrons by Rare-Earth Oxides

T. Murata

P8. Impact of Cross Section Library Update from ENDF/B-VI.8 to ENDF/B-VII.0 on BWR Fuel Burnup Characteristics

A. Toishigawa (GNF-J)

P9. Analysis of irradiated UO_2 and MOX fuel composition data measured in REBUS program

Y. Ando (JNES)

P10. Comments to iron data in JENDL-3.3

C. Konno (JAEA)

P11. Nuclear data benchmark for sodium voided reactivity worth with improved neutronics simulation method

G. Chiba (JAEA)

P12. CBGLIB: A multi-group neutron library for accurate neutronics simulation

G. Chiba (JAEA)

This is a blank page.

2. Papers Presented at Oral Sessions

This is a blank page.

2.1 Present Status of JENDL-4

Keiichi SHIBATA

Nuclear Data Center

Japan Atomic Energy Agency

Email: shibata.keiichi@jaea.go.jp

Abstract

The fourth version of Japanese Evaluated Nuclear Data Library (JENDL-4) is being developed at the Nuclear Data Center of JAEA in cooperation with the Japanese Nuclear Data Committee. Much emphasis is placed on the improvement of fission product (FP) and minor actinide (MA) data in JENDL-4. For this purpose, nuclear model codes were newly developed. As for FP, resolved resonance parameters were updated for 107 nuclei. Moreover, a new set of global coupled-channel optical model parameters was obtained in the incident neutron and proton energy region up to 200 MeV. Evaluation for JENDL-4 is almost on schedule.

1. Introduction

Following the discussion at the Ad Hoc Committee on Next JENDL under the Japanese Nuclear Data Committee (JNDC), we decided to start developing JENDL-4. The objective of JENDL-4 is to provide a reliable evaluated data set for various fields such as the development of innovative reactors, high burn-up and the use of MOX fuels for LWR, criticality safety with burn-up credit, and basic science. Several subjects are regarded as important: resolving open problems with JENDL-3.3[1], improvements of FP and MA data, generation of more covariances and gamma-ray production data, reexamination of FP yields, carrying out more benchmarks, and production of reactor constants. Nuclear model codes have been developed to raise the reliability of FP and MA data. This paper focuses on the code development and evaluations of medium nuclei including FP. The activities on actinides are presented by Nakagawa *et al.* in this symposium.

2. Nuclear Model Codes

In the evaluations for JENDL-3 series, we had used nuclear model codes made in foreign countries, although there existed activities on code development in the early days. However, our own nuclear model codes were required in order to reflect advanced physical

knowledge on the codes and to carry out efficient evaluation work. Under such circumstances, two nuclear model codes were newly developed: POD[2] and CCONE[3]. Both
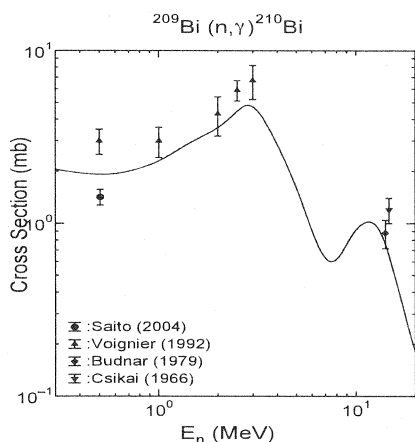
Fig. 1 ^{209}Bi(n,γ) cross section
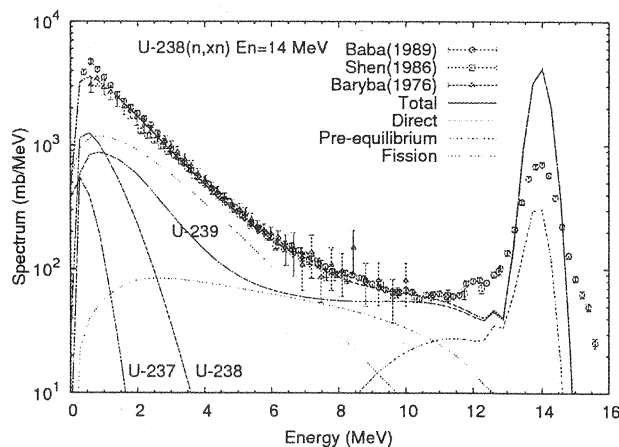
Fig.2 ^{238}U(n,xn) spectra at 14 MeV

codes are based on the Hauser-Feshbach theory with preequilibirum effects. Direct reaction processes (DWBA or coupled-channel) are also contained in the codes. POD is mainly used for medium and FP nuclei, although CCONE is for actinide nuclei. **Figure 1** shows the capture cross section of ^{209}Bi calculated by POD with default parameters. The calculations reproduce experimental data. The neutron emission spectra from ^{238}U were calculated with CCONE at 14 MeV and are illustrated in **Fig.2**.

3. Evaluation of FP Data

There are 213 nuclei regarded as FP having a half life of more than 10 days and a fission yield of more than 0.1%. We set up a priority for each nucleus by considering the following items: needs from LWR, FBR and ADS, availability of differential measurements, comparison of JENDL-3.3 cross sections with measurements, benchmark results[4] of JENDL-3.3, and recommendation[5] by WPEC Subgroup 21 which selected the best FP data for individual nuclei. As a result, top priorities were assigned to 63 nuclei.

1) Low-energy Region

Resolved resonance parameters are needed to represent complicated resonance structure in the low-energy region. Updates of the parameters were done by considering new experimental data. In cases where L or J value is missing, a certain value is assumed by using the Porter-Thomas distribution or the level density formula. Thermal cross sections and resonance integrals were calculated and compared with experimental data after compiling

the resonance parameters. So far, data for 107 nuclei were updated; 51 nuclei remain unchanged from JENDL-3.3; 13 nuclei were newly evaluated; 42 nuclei have no resolved resonance parameters since there are no experimental values. The parameters for ^{157}Gd are pending, because the new parameters obtained by Leinweber et al.[6] yield 10% smaller capture cross section than JENDL-3.3 as shown in **Fig. 3**. A resonance at 0.032 eV exhibits a non 1/v shape in the low energy region. The difference between the new results and JENDL-3.3 should be examined by benchmark tests.

2) High-energy Region

In non-resonance energy region, the statistical model based on the Hauser-Feshbach theory is applied to calculate energy-averaged cross sections. Though there are many parameters required for statistical-model codes, the most important ones are optical model parameters which give an average interaction field for particle transmission. Kunieda et al.[7] obtained a global optical-model parameter set for a wide mass range in the incident neutron and proton energy up to 200 MeV by using the coupled-channel method. It should be noted that this parameter set reproduces measured s-wave neutron strength functions as seen in **Fig. 4**, where the present calculations (red circles) are more consistent with measured data than the spherical optical-model calculations
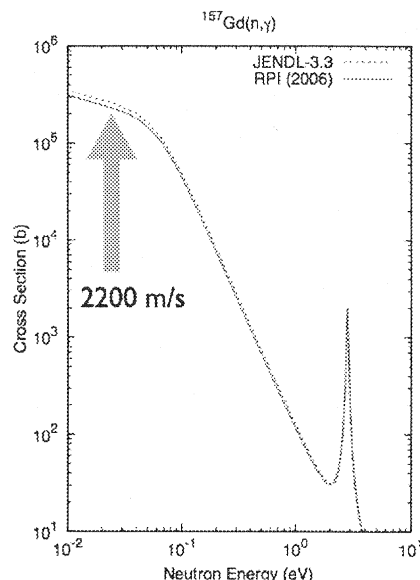
Fig. 3 ^{157}Gd(n,γ) cross section
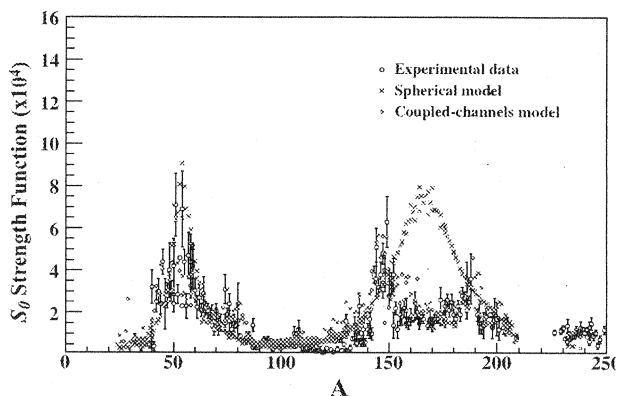
Fig. 4   s-wave neutron strength function
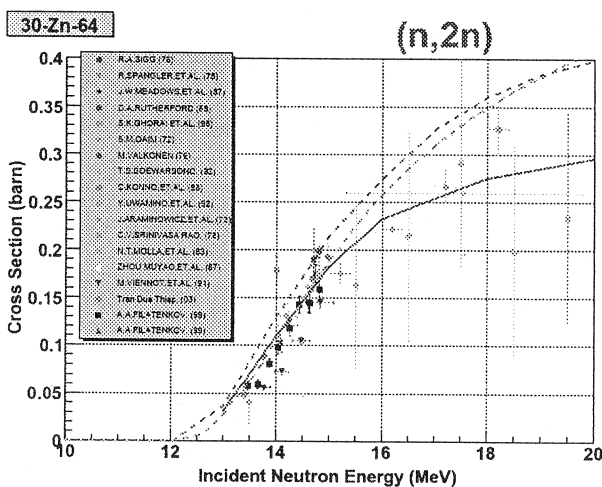
Fig. 5 ^{64}Zn(n,2n) cross section

(blue crosses). Evaluation of FP data is in progress by using these optical model parameters. As an example of the evaluation, the ^{64}Zn(n,2n) cross section is illustrated in **Fig. 5**, where the solid line stands for the present evaluation, the purple dashed one for JENDL/A-96[8], and the green dashed one for JEFF-3.1/A.[9] Moreover, data for Ag, Sn, Nd, Pm, Tb and Dy were already evaluated.

4. Evaluation of Light and Medium Nuclei

Data for Si and Ca isotopes were evaluated[10,11], since the elements are ingredients of concrete and their cross sections are important from the viewpoints of shielding. Evaluation of ^{197}Au, of which capture cross sections is used as a standard, is under way. We plan to reexamine data for ^{1}H, ^{16}O, Cr, Fe, and Ni.

5. Issues Carried Over After JENDL-4

There are several issues mentioned in the report[12] made by the Ad Hoc Committee on Next JENDL. One of them is related to the development of home-made nuclear model codes. This issue was obviously resolved by the recent activities on code development. However, some issues still remain and they will be probably carried over after JENDL-4.

Thermal scattering law data are required for LWR, but there exists no activity in JNDC. The activity is shrinking in the world, since the specialists are retiring without replacements. Lack of the scattering law data is a weak point of JENDL. We should do something to make JENDL a standard library in Japan.

Resolved resonance parameters play an important role are for applications to nuclear reactors. However, the parameters of major actinides and structural materials were taken from the resonance analyses mostly made by a group in the Oak Ridge National Laboratory. We should bring up a specialist who can deal with resonance data.

Many people use NJOY[13] to process evaluated nuclear data. Users requested the Nuclear Data Center to keep a specialist who can take care of NJOY in Japan, although the request is not satisfied yet. This may be the issue that should be resolved by the joint responsibility of our group and the reactor physics community in Japan.

6. Concluding Remarks

The fourth version of JENDL, JENDL-4, is now under development. In JENDL-4, it is important to raise the reliability of FP and MA data for applications to innovative nuclear

reactors. Much effort was made to develop nuclear model codes based on the Hauser-Feshbach theory. Consequently, two codes POD and CCONE were produced and they are being used for evaluations. As for FP, resolved resonance parameters were updated for 107 nuclei. In the higher energy region of FP, we obtained a set of global coupled-channel optical model parameters, which reproduce available experimental data very well. Using the set of parameters, evaluations were performed for Zn, Ag, Sn, Nd, Pm, Tb and Dy. Furthermore, cross sections of other nuclei are being evaluated. In the light and medium mass region, data on Si and Ca isotopes were re-evaluated. The data on ^{1}H, ^{16}O, Cr, Fe, and Ni will be examined. Evaluation for JENDL-4 is almost on schedule.

References

1) K. Shibata, T. Kawano, T. Nakagawa *et al.*, "Japanese Evaluated Nuclear Data Library Version 3 Revision-3: JENDL-3.3," *J. Nucl. Sci. Technol.*, **39**, 1125 (2002).

2) A. Ichihara, O. Iwamoto, S. Chiba *et al.*, Program POD; *A Computer Code to Calculate Cross Sections for Neutron-Induced Nuclear Reactions*, JAEA-Data/Code 2007-012 (2007).

3) O. Iwamoto, "Development of a comprehensive code for nuclear data evaluation, CCONE, and validation using neutron-induced cross sections for uranium isotopes," *J. Nucl. Sci. Technol.*, **44**, 687 (2007).

4) M. Kawai, T. Watanabe, A. Zukeran *et al.*, "Interpretation of integral test results of FP cross sections in JENDL-3.2 by analyzing the STEK experiments," *J. Nucl. Sci. Technol.*, **Suppl. 2**, 982 (2002).

5) P. Oblozinsky, *Assessment of Neutron Cross-Section Evaluations for the Bulk of Fission Products*, NEA/WPEC-21 (2005).

6) G. Leinweber, D.P. Barry, M.J. Trbovich *et al.*, "Neutron capture and total cross-section measurements and resonance parameters of gadolinium," *Nucl. Sci. Eng.*, **154**, 261 (2006).

7) S. Kunieda, S. Chiba, K. Shibata *et al.*, "Coupled-channels optical model analyses of neutron-induced reactions for medium and heavy nuclei in the energy region from 1 keV to 200 MeV," *J. Nucl. Sci. Technol.*, **44**, 838 (2007).

8) Y. Nakajima, JNDC WG on Activation Cross Section Data, "JENDL activation cross section file," *Proc. 1990 Symposium on Nuclear Data*, JAERI-M 91-032, p.43 (1991).

9) A. Koning, R. Forrest, M. Kellet *et al.*, *The JEFF-3.1 Nuclear Data Library*, JEFF

Report 21, OECD/NEA (2006).

10) K. Shibata, "Calculation of neutron nuclear data on calcium isotopes for JENDL-4," *J. Nucl. Sci. Technol.*, **44**, 1 (2007).

11) K. Shibata, S. Kunieda, "Calculation of neutron nuclear data on silicon isotopes for JENDL-4," to be published in *J. Nucl. Sci. Technol.*

12) K. Shibata, M. Igashira, M. Ishikawa *et al.*, "A database supporting nuclear energy," a report made by *the Ad Hoc Committee on Next JENDL* (2003) [in Japanese].

13) R.E. MacFarlane, "Recent progress on NJOY," LA-UR-96-4688 (1996).

2.2 Nuclear Data Evaluation for Actinoid Nuclides

Tsuneo NAKAGAWA[*], Osamu IWAMOTO, Naohiko OTUKA,

Satoshi CHIBA

Japan Atomic Energy Agency

Tokai-mura, Naka-gun, Ibaraki-ken 319-1195

*) nakagawa.tsuneo@jaea.go.jp

Abstract

New evaluation of nuclear data for JENDL Actinoid File (JENDL/AC) is in progress. JENDL/AC will contain the data for 79 nuclides. The energy range of incident neutrons is from 10^{-5}eV to 20 MeV. Data in the smooth region were calculated with CCONE code. Fission cross sections of important nuclides were evaluated with the simultaneous evaluation method. GMA code was used to evaluate the fission cross sections for other nuclides. Resonance parameters were revised from JENDL-3.3 for many nuclides. JENDL/AC will be released in FY2007.

1. Introduction

The current Japanese evaluated nuclear data library JENDL-3.3 [1] was released in 2002. The data of actinoid nuclides in JENDL-3.3 are being revised to JENDL Actinoid File (JENDL/AC) which will contain revised data of neutron-induced reactions for 62 nuclides from Ac to Fm already given in JENDL-3.3 and 17 new nuclides which were selected on a criterion of a half-life longer than 1 day. The energy range of incident neutrons is from 10^{-5} eV to 20 MeV. The status of JENDL/AC is shortly described in this presentation.

2. Resonance parameters

Recent results of SAMMY [2] analyses were adopted to ^{232}Th, ^{233}U, ^{238}U and ^{241}Pu from ENDF/VII.0 [3]. For ^{239}Pu, results of new analysis by Derrien et al.[4] were adopted. The parameters of ^{236}Np and ^{238}Np were analyzed by Furutaka [5] with SAMMY code.

For ^{235}U, the same parameters as JENDL-3.3 were adopted. However the upper boundary of the resolved resonance region was lowered from 2.25 keV to 500 eV. It was pointed out that the capture cross section of JENDL-3.3 was probably too large in the resolved resonance region. This problem is investigated in the WPEC subgroup 29. For JENDL/AC, the ^{235}U cross sections in the energy range from 500 eV to 2.25 keV were determined as follows: The cross sections were calculated from the resonance parameters given in JENDL-3.3 and broadened by adopting an energy resolution of 3% ($\Delta E=0.03\times E$). The capture cross section was lowered by multiplying an energy dependent factor so that the average cross section became to be almost the same as JENDL-3.2 [6]. The elastic scattering cross section was calculated as differences between total and non-elastic scattering cross sections.

For the other nuclides, cross sections calculated from resonance parameters given in JENDL-3.3 were compared with experimental data. For the resonances of which cross section had large discrepancies, their resonance parameters were revised. The fission cross section of ^{243}Cm shown in

Fig. 1 is an example of such cases.

Average thermal cross sections were obtained from experimental data. Resonance parameters of negative and low-lying resonances were adjusted to reproduce the thermal cross sections. For example, the thermal capture cross section of ^{241}Am was summarized in Table 1. The average cross section is 697 b which is 9% larger than JENDL-3.3. Experimental data of the total cross section are smaller than present evaluation, but they were ignored because they were old measurements reported in 1955.

Table 1 ^{241}Am(n,γ) cross sections at 0.0253 eV

JENDL-3.3	639.5 b
Kalebin (1976)	624 ± 20 b
Shinohara+ (1997)	854 ± 58 b
Fioni+ (2001)	696 ± 48 b
Bringer+ (2006)	714 ± 23 b
Present	697.1 b

Unresolved resonance parameters were re-evaluated for many nuclides. Upper boundaries of the unresolved resonance region were determined to be high enough for calculation of self-shielding factors. Parameters were determined with ASREP code [7] so as to reproduce the cross sections evaluated in the unresolved resonance region. The option of ENDF format (LSSF=1) that means those parameters are used only for self-shielding calculations was selected.

For minor nuclides which have no experimental data of resonance parameters, no resolved and unresolved resonance parameters were given. If no experimental data are available at the thermal neutron energy, thermal capture and fission cross sections were estimated from their systematic trend. Cross-section shape of 1/v was assumed for the both reaction. The elastic scattering cross section was calculated from scattering radius obtained from CCONE calculation. Upper boundaries of the 1/v region were estimated to be a half of average level spacing.

3. Smooth cross sections above the resonance region

3.1 Theoretical calculation with CCONE code

Above the resonance region, theoretical calculation was widely performed with CCONE code [8] developed by O.Iwamoto. CCONE code is based on the coupled channel optical model, DWBA, pre-equilibrium exciton model and statistical model, and calculates the fission cross sections for evaluation of actinoid nuclides. Figure 2 is an example of fission cross sections calculated with CCODE code. The experimental data of ^{243}Am fission cross section are fairly well reproduced with CCONE calculation.

Since the fission cross section is calculated well, results for the other reactions could be expected to be reliable. An example is the ^{238}U(n,2n) reaction cross section shown in Fig. 3. The cross section of JENDL-3.3 was determined from the experimental data of Frehaut et al.[9,10] In the present work, the data of Frehaut et al. were considered by multiplying a factor of 1.1 to normalize them to recent experimental data around 14 MeV, because they were systematically smaller than other experimental data. A CCONE calculation reproduced quite well the modified Frehaut's data. Therefore,

the result of CCONE calculation was adopted for JENDL/AC.

The capture cross sections calculated with CCONE code are also in good agreement with experimental data as shown in Fig. 4. The results of CCONE calculation were adopted for many nuclides.

The isomeric ratio (IR) of ^{241}Am(n,γ) reaction was also calculated with CCONE code, and the IR to the ground state (IR$_g$) was normalized to 0.85 at 500 keV. At the thermal neutron energy, several experimental data are available. An average value of the experimental data (0.896) was adopted below 0.1 eV, and straightly connected to the normalized CCONE calculation at 1 eV. An average IR$_g$ is 0.878 in a typical PWR and 0.850 in an FBR. Nakamura et al. [11] measured the thermal cross section of ^{241}Am(n,γ)^{242g}Am reaction, and reported the value of 628±22b. Present evaluation for IR and thermal cross section gives a value of 625b which is consistent with their new measurement.

Calculated with CCONE code were also the angular distributions of elastically scattered neutrons, double differential cross sections, and fission neutron spectra. Concerning the fission spectra of important nuclides, the data of JENDL-3.3 were adopted below about 5 MeV, and CCONE calculation above that energy.

3.2 Fission cross sections

The fission cross section can be calculated well with CCONE code by adjusting model parameters. However, it was evaluated based on available experimental data as much as possible. For the main actinides of ^{233}U, ^{235}U, ^{238}U, ^{239}Pu, ^{240}Pu and ^{241}Pu, the simultaneous evaluation method was applied. SOK code [12] developed by Kawano for JENDL-3.3 evaluation was used for this purpose. Comparison of ^{235}U fission cross section with recent experimental data (Fig. 5) shows that JENDL-3.3 may be too large. This means that recent experimental data are smaller than old ones. Only the recent experimental data reported after 1980 were used for the ^{235}U fission cross section in the present simultaneous evaluation.

For minor actinoid nuclides having experimental data, they were determined by using GMA code [13,14] which is a code based on the least-squares method. Ratio data to ^{235}U or ^{239}Pu fission cross sections were transformed to the cross sections by using JENDL-3.3 data for ^{235}U and ^{239}Pu. An example is given in Fig. 6.

For the other minor nuclides which have no or less experimental data, results of CCONE calculation were adopted.

4. Conclusion

The current data for JENDL/AC are certainly better than JENDL-3.3. They are in better agreement with experimental data, and with integral experimental data such as k-eff of reactors and critical assemblies. Prediction of number of nuclides measured by post-irradiation experiments has been improved. The data of JENDL/AC will be further improved before its release. For example, the model parameters of CCONE calculation for important nuclides will be improved by adjusting them to integral experiments.

References

[1] K. Shibata et al. : *J. Nucl. Sci. Technol.*, **39**, 1125 (2002).

[2] N.M.Larson: "Updated Users' Guide for SAMMY: Multilevel R-Matrix Fits to Neutron Data Using Bays' Equations, " ORNL/TM-9179/R7 (2006).

[3] M.B. Chadwick et al.: *Nucl. Data Sheets*, **102**, 2931 (2006).

[4] H.Derrien et al.: Proceeding of International Conference on Nuclear Data for Science and Technology, Nice, 22 - 27 April, 2007, ADI#374 (2007).

[5] Furutaka: private communication.

[6] T.Nakagawa et al. : *J. Nucl. Sci. Technol.*, **32**, 1259 (1995).

[7] Y.Kikuchi et al.: "ASREP: A Computer Program for Automatic Search of Unresolved Resonance Parameters," JAERI-Data/Code 99-025 (1999).

[8] O.Iwamoto: *J. Nucl. Sci. Technol.*, **44**, 687 (2007).

[9] J.Frehaut et al.: *Nucl. Sci. Eng.*, **74**, 29 (1980).

[10] J.Frehaut et al.: BNL-NCS-51245, vol.1, p.399 (1980).

[11] S.Nakamura et al.: *J. Nucl. Sci. Technol.*, **44**, 1500 (2007).

[12] T.Kawano et al.: "Evaluation of Fission Cross Sections and Covariances for U-233, U-235, U-238, Pu-239, Pu-240 and Pu-241,"JAERI-Research 2000-004 (2000).

[13] W.P.Poenitz: BNL-NCS-51363, Vol.I, p.249 (1981).

[14] S.Chiba and D.L.Smith: "A Suggested Procedure for Resolving An Anomaly in Least-Squares Data Analysis Known as "Peelle's Pertinent Puzzle" and The General Implications for Nuclear Data Evaluation," ANL/NDM-121 (1991).
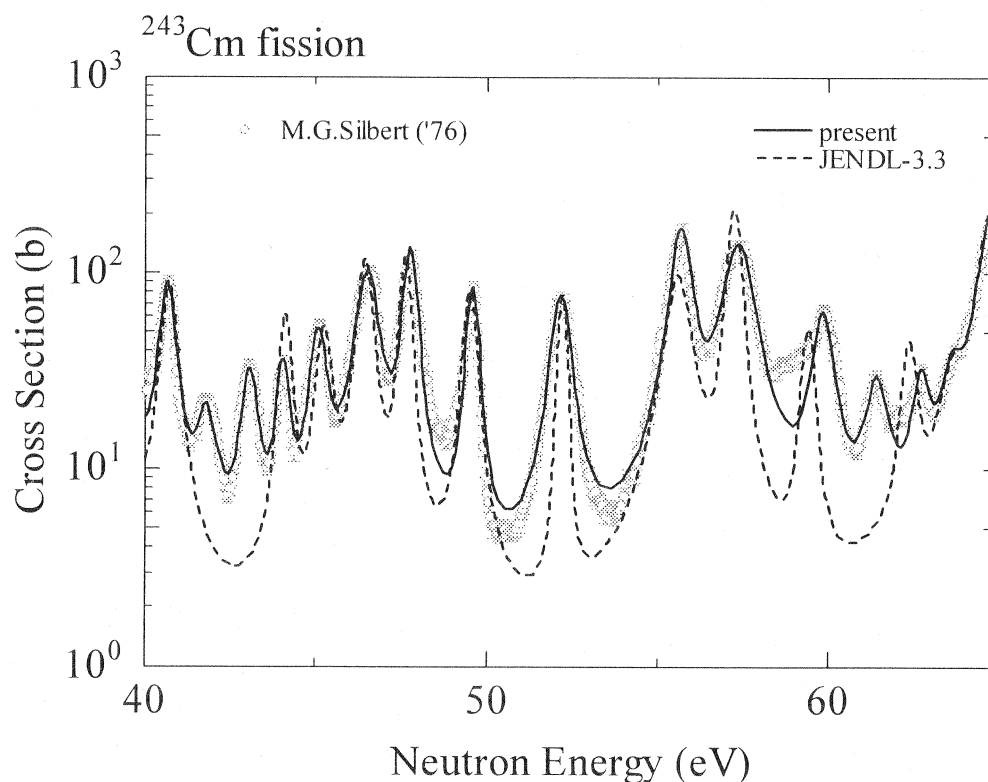
Fig. 1 ^{243}Cm fission cross section in the resonance region
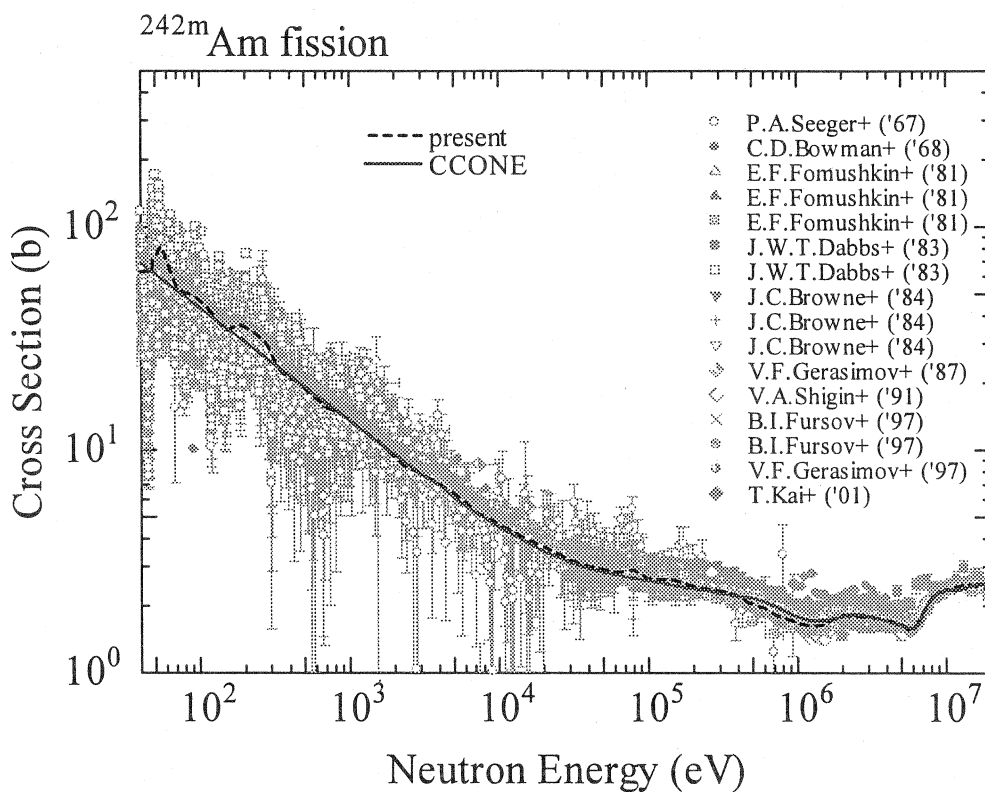
^{242m}Am fission

Fig.2 ^{242m}Am fission cross section

^{238}U (n,2n)

Fig.3 ^{238}U(n,2n) reaction cross section

^{241}Am capture

present (=CCONE)
JENDL-3.3
ENDF/B-VII

G.N.Flerov+ ('67)
D.B.Gayther+ ('77)
K.Wisshak+ ('80)
K.Wisshak+ ('80)
K.Wisshak+ ('80)
K.Wisshak+ ('80)
K.Wisshak+ ('80)
K.Wisshak+ ('82)
G.Vanpraet+ ('85)
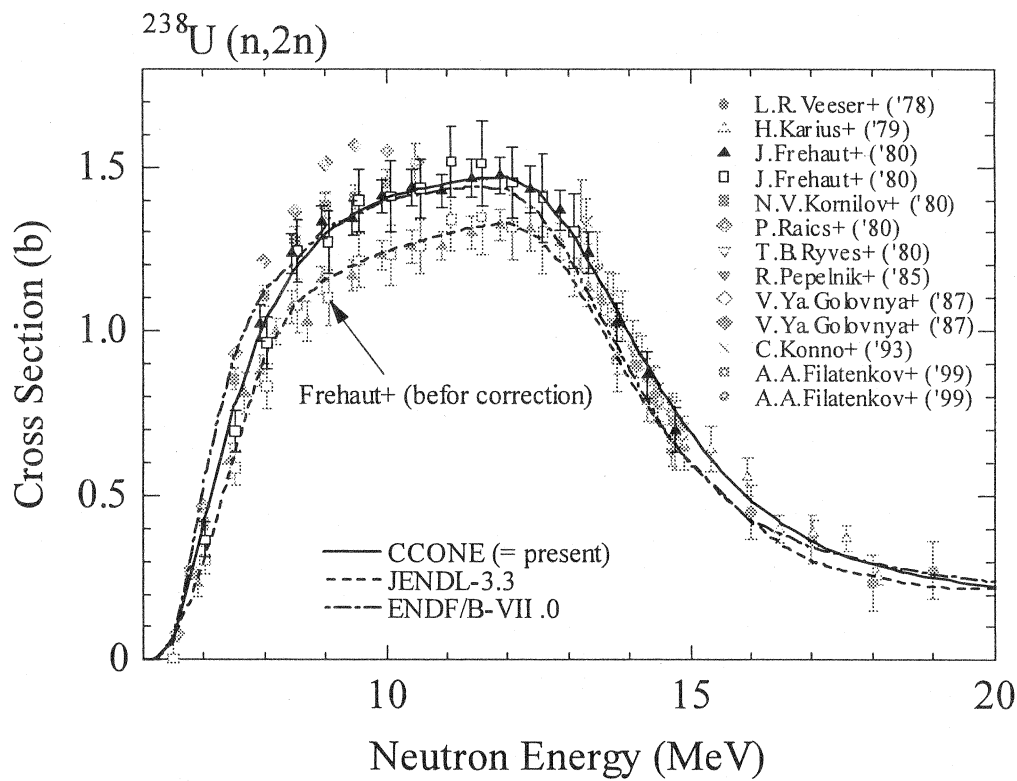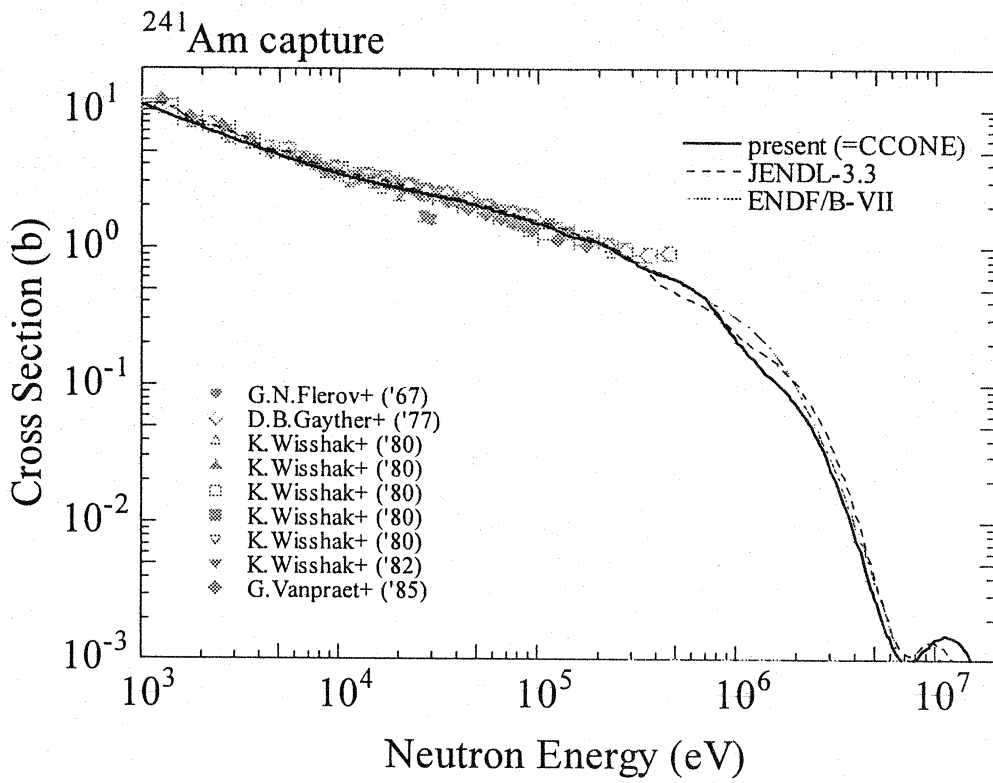
Fig.4 ^{241}Am capture cross section

^{235}U fission

A.D.Carlson ('83)
I.D.Alkhazov+ ('83)
A.D.Carlson+ ('84)
L.W.Weston+ ('84)
C.M.Herbach+ ('85)
C.M.Herbach+ ('85)
R.Arlt+ ('85)
R.Arlt+ ('85)
I.D.Alkhazov+ ('86)
Li Jingwen+ ('86)
J.Rapaport+ ('87)

I.D.Alkhazov+ ('88)
I.D.Alkhazov+ ('88)
N.N.Buleeva+ ('88)
R.G.Johnson+ ('88)
T.Iwasaki+ ('88)
K.Merla+ ('91)
K.Merla+ ('91)
R.G.Johnson+ ('91)
V.A.Kalinin+ ('91)
D.Rochman+ ('05)

JENDL-3.3
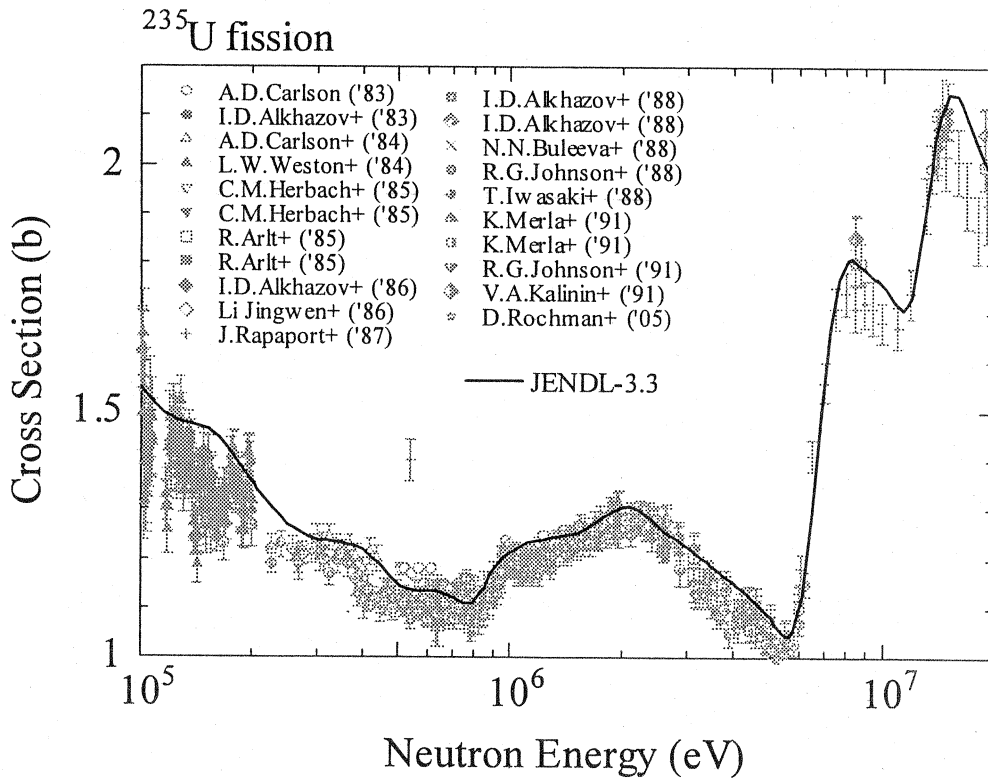
Fig.5 ^{235}U fission cross section
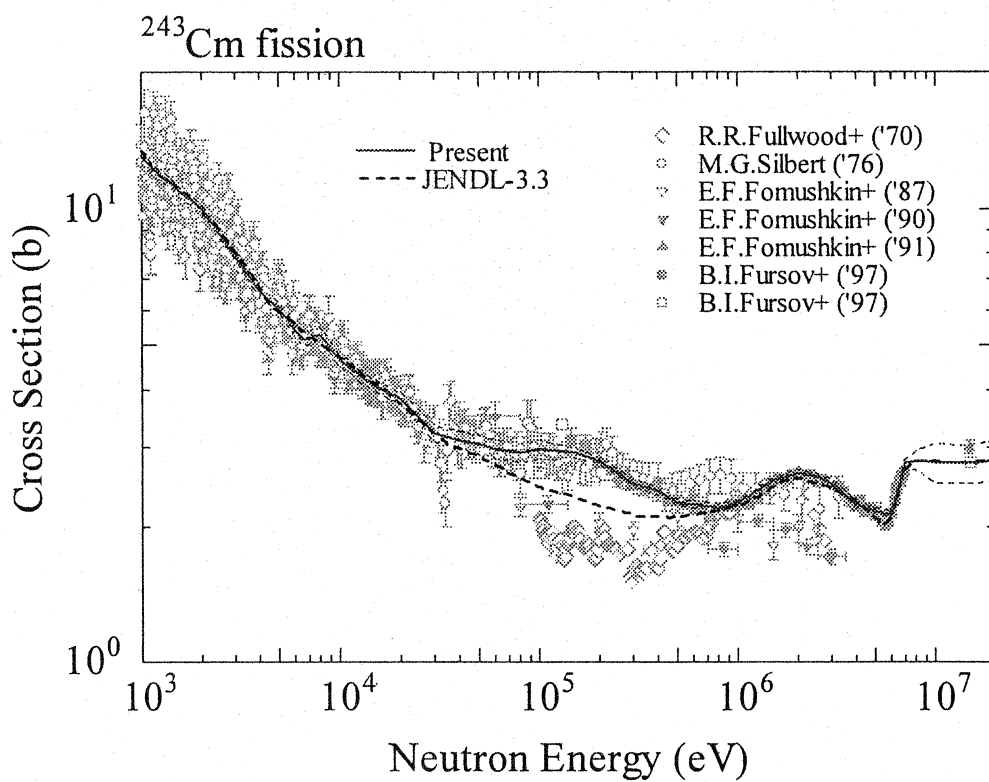
Fig.6 ^{243}Cm fission cross section

2.3 Neutron Cross Section Measurement of MA

Hideo HARADA

Nuclear Science and Engineering Directorate, Japan Atomic Energy Agency

Tokai-mura, Naka-gun, Ibaraki-ken 319-1195

e-mail: harada.hideo@jaea.go.jp

Obtaining accurate neutron cross sections of minor actinides (MAs) is one of the most important issues in current nuclear data field. Over the last decade, various progresses have been done on the measurements of MAs. The new measurements made it clear that there are still unacceptable discrepancies between the measurements. Current situation on these problems is reviewed using the example of ^{237}Np. To solve the problems clearly, further efforts should be done to reduce the experimental uncertainties and then compare the high quality results obtained independently each others.

1. Introduction

Accurate neutron cross sections of minor actinides (MAs) are required for the quantitative studies of a nuclear transmutation system or an innovative nuclear fuel cycle system, in which huge amount of MAs are transmuted or treated [1,2]. Over the last decade, significant efforts have been done on the measurements of MA in Japan and in the world. In this report, the recent progresses of this decade are reviewed focusing on the measurements of the neutron capture cross section of ^{237}Np as one of the most important nuclear data of MAs, and then future issues to be solved are discussed.

2. Neutron capture cross section of ^{237}Np for thermal neutrons

Short history on the measurement of the neutron capture cross section of ^{237}Np for thermal neutrons was summarized in **Table 1**. Brown and Hall[3] measured the thermal neutron capture cross section of ^{237}Np by counting α particles emitted from ^{237}Np and ^{238}Pu, and obtained a value of 172 ± 7 b. Smith *et al.* [4] measured the total cross section of ^{237}Np by a transmission method and reported a value of 170 ± 22 b, where the contribution of the scattering cross section was calculated and subtracted from the total cross section. Tattersall *et al.* [5] obtained it as 169 ± 3 b by a pile oscillation method. Schuman and Berreth [6] measured it as 185 ± 12 b by an activation method by counting α particles emitted from ^{237}Np and ^{238}Pu as Brown *et al.* did.

Since 1984, three independent measurements of the cross section have been performed by an activation method with high-resolution Ge detectors for counting γ rays. Jurova et al. [7] reported the value as 158±4 b. Kobayashi et al. [8] obtained almost the same value as Jurova et al. Katoh et al. [9] deduced the thermal neutron capture cross section as 141.7±5.4 b. All of three data measured by a γ ray spectroscopic method are much smaller than those measured by other methods. To deduce the neutron capture cross section by an activation method with γ ray spectroscopy, the relevant γ-ray emission probabilities are used. Harada et al. [10] pointed out that these decay data could be an origin of the discrepancies on the neutron capture cross section of ^{237}Np shown in Table 1. To examine the hypothesis, they measured the relevant emission probabilities of the 312-keV γ ray from the decay of ^{233}Pa and the 984-keV γ ray from the decay of ^{238}Np. The obtained emission probabilities were used to correct the thermal neutron capture cross section of ^{237}Np reported previously. For example, the value reported by Katoh et al. becomes 168±6 b. The cross section was also independently determined [10] as 169±6 b by irradiating ^{237}Np sample in the research reactor of Kyoto University (KUR) and counting α rays emitted from ^{237}Np and ^{238}Pu with a Si detector. Here, we need to note that Harada et al. measured the effective capture cross section and needed to use 0.982 as the Westcott g factor and 6.27 ±0.41 [9] as the s_0 value to deduce the thermal neutron capture cross section of ^{237}Np. The careful evaluations of the g and also the s_0 factors are important, as well as the accurate measurements of these quantities by TOF measurement methods. The comparison of the s_0 determined by activation methods and TOF methods will be valuable.

Table 1 Summary of ^{237}Np capture cross section measurements for thermal neutrons

Authors	(year)	σ_0 (b)	Methods
Harada et al.	(2006)	169±4	Activation, α&γ
Katoh et al.	(2003)	141.7±5.4	Activation, γ
Kobayashi et al.	(1994)	158±3	Activation, γ
Jurova et al.	(1984)	158±4	Activation, γ
Schuman et al.	(1969)	185±12	Activation, α
Tattersall et al.	(1960)	169±3	Pile Oscillation
Smith et al.	(1957)	170±22	σ_{TOT} - σ_{SCA}(CAL)
Brown et al.	(1956)	172±7	Activation, α

3. Neutron capture cross section in keV region

The measurements of the neutron capture cross section of [237]Np in keV region published in this decade are reviewed here. In 2002, Kobayashi et al. have measured the cross section [11] for the energy range between 0.004 eV and 10 keV using a pair of C_6D_6 scintillation detector and 1 g of [237]Np sample at 12 m neutron flight path at the Kyoto electron linear accelerator facility. Shcherbakov *et al.* measured it [12] for the energy range between 0.02 eV and 1 keV using a 4π BGO scintillation detector and the same sample at 22 m neutron flight path. Esch *et al.* measured it [13] for the energy range between 0.02 eV and 200 keV using a 4π BaF_2 scintillation detector and the [237]Np sample of 0.44 mg at 20 m neutron flight path at the Manuel Lujan Jr. Neutron Scattering Center at the Los Alamos Neutron Science Center (LANSCE). These data are compared in Fig. 1. The data published before 1997 are not included in Fig. 1. The discrepancies between these data are within about 15 % for the energy region below 100 eV. Although the cross section has been measured in the n-TOF project [14] for the energy range between 10 eV and 1 keV using a 4π BaF_2 scintillation detector at 185 m neutron flight path at the proton synchrotron in CERN, the absolute cross section is not shown in ref. [14]. Recently, Mizumoto *et al.* have measured [15] the cross section using a 4π Ge spectrometer [16] for the energy range between 0.02 eV and 1 keV using two kind of [237]Np samples at 10 m neutron flight path at the Kyoto electron linear accelerator facility. The data are expected to be evaluated and contribute to reduce furthermore the uncertainties for the energy range below 100 eV.
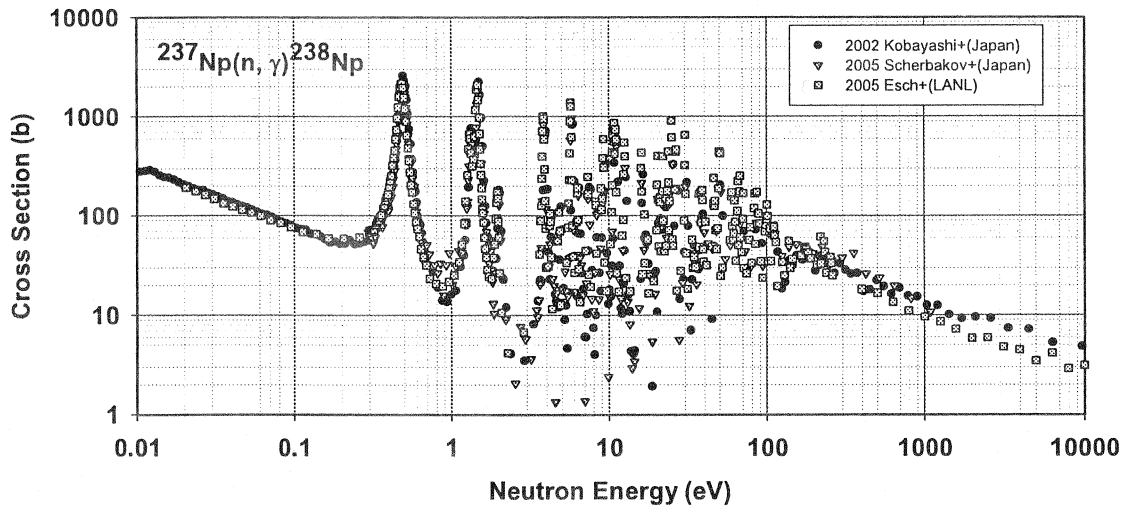

Fig. 1   Recent measurements of the capture cross section of [237]Np by TOF methods

On the other hand, the discrepancy increases for higher energy region, and also the data available is very limited as was shown in Fig. 1. Accurate measurements and evaluations of the cross section above a few hundred eV will be a very important issue to be solved.

4. New Possibilities in Japan

A new beam line for the nuclear data measurement [17] is under construction at J-PARC. The line enables the measurement of nuclear data with a small amount of sample as a function of neutron energy by a TOF method, which is expected to be a powerful tool for the measurements of nuclear data on MAs.

For the measurement of neutron cross sections for MeV neutrons, a utilization of an activation method using fast reactor neutrons supplied by the Yayoi reactor is under investigation by Nakamura *et al*[18]. On the other hand, quasi-mono energy neutrons have been available since 2007 at the 4 MeV Pelletron accelerator laboratory in the facility of radiation standards of JAEA tokai center. The measurement system of neutron capture cross sections for keV-MeV neutrons is under development by Segawa *et al*[19].

In order to deduce the neutron capture cross section, the inverse reaction cross section of neutron capture, that is, the photo-neutron cross section could be used by combining with the statistical model calculation. The precise measurement method of the photo-neutron cross section is under development using laser-Compton scattering photons in Japan [20]. This method will be an especially important tool in the case that the sample for the neutron capture cross section is not available, for example, ^{79}Se. On the other hand, the surrogate reactions have been utilized to deduce the fission and capture cross sections in the world [21]. The possibility utilizing the reaction with the JAEA-tokai tandem accelerator has been discussed by Makii *et al.* [22].

5. Summary

Current status on the neutron cross sections of MAs has been reviewed. Various efforts on the measurements of neutron cross sections of MAs have been done to overcome the inherent experimental difficulties. Although different measurement methods sometimes gave discrepant results, studies on the origins of these discrepancies are effective to reduce experimental ambiguities, as was discussed using an example.

In second, the severe situation of the cross section of MAs above a few hundred eV has been pointed out. However, many new approaches are under development and new facilities will be soon available in Japan. It is highly expected that the high quality experimental data of MAs being superior to the present ones will be obtained utilizing the new approaches and new facilities in the next decade, which will be a fundamental data for realizing a full-scale management of MAs.

References

1) OECD/NEA, "Accelerator-driven systems (ADS) and fast reactors (FR) in advanced nuclear fuel cycles, a comparative study," (2002).

2) M. Salvatores, "Nuclear fuel cycle strategies including Partitioning and Transmutation", Nuclear Engineering and Design, 235 [7] 805 (2005).

3) F. Brown, G. R. Hall, "The thermal neutron capture cross-section of Np^{237} ", J. Inorg. Nucl. Chem., 2, 205 (1956).

4) M. S. Smith, R. R. Smith, E. G. Joki, J. E. Evans, " Neutron total cross section of Np^{237} from 0.02 to 2.8 eV", Phys. Rev., 107, 525(1957).

5) R. B. Tattersall, H. Rose, S. K. Pattenden, D. Jowitt, "Pile oscillator measurement of resonance absorption integrals", J. Nuclear Energy, Part A: Reactor Science, 12, 33 (1960).

6) R. P. Schuman, J. R. Berreth, "Resonance integral measurement", IN-1296 (Prog. Report of Idaho Nuclear Corp.), (1969).

7) L. N. Jurova, A. A. Poljakov, V. P. Rukhlo, et al., Yadernye Konstranty, 1/55, 3 (1984).

8) K. Kobayashi, A. Yamanaka, I. Kimura, "Measurement of thermal neutron cross section and resonance integral for ^{237}Np(n, γ)^{238}Np reaction", J. Nucl. Sci. Technol., 31 [12], 1239 (1994).

9) T. Katoh, S. Nakamura, K. Furutaka, et al., "Measurement of thermal neutron capture cross section and resonance integral of the ^{237}Np(n, γ)^{238}Np reaction", J. Nucl. Sci. Technol., 40 [8], 559 (2003).

10) H. Harada, S. Nakamura, M. Ohta, et al., "Emission Probabilities of Gamma Rays from the Decay of ^{233}Pa and ^{238}Np, and the Thermal Neutron Capture Cross Section of ^{237}Np", J. Nucl. Sci. Technol., 43 [11], 1289 (2006).

11) K. Kobayashi, S. Lee, S. Yamamoto et al., "Measurement of Neutron Capture Cross Section of ^{237}Np by Linac Time-of-Flight Method and with Linac-driven Lead Slowing-down Spectrometer", J. Nucl. Sci. Technol., 39 [2], 111 (2002).

12) O. Sherbakov, K. Furutaka, S. Nakamura et al., "Measurement of Neutron Capture Cross Section of ^{237}Np from 0.02 to 100 eV", J. Nucl. Sci. Technol., 42 [2], 135 (2005).

13) E.I.Esch, R.Reifarth, A.Alpizar-Vicente, et al., "The ^{237}Np(n, γ) cross section between 20 meV and 200 keV", Los Alamos Scientific Lab. Reports No.05, p.6885 (2005), and EXFOR #14032.002.

14) D. Cano-Ott, U. Abbondanno, G. Aerts, et al., "Neutron Capture Cross Section Measurements at n_TOF of ^{237}Np, ^{240}Pu, and ^{243}Am for the Transmutation of Nuclear Waste", Symp. on Capt. Gamma Ray Spectroscopy, Notre Dame 2005, p.318 (2005)

15) M. Mizumoto, M. Igashira, T. Katabuchi, et al., "Data analyses of ^{237}Np neutron capture cross section measurements", 日本原子力学会「2007 秋の大会」予稿集　M14

(2007).

16) M. Koizumi, A. Osa, Y. Toh, *et al.*, "Minor actinide neutron capture cross-section measurements with a 4π Ge spectrometer", *Nucl. Instru. Method.* **A562**, 767 (2006).

17) Y. Kiyamnagi, in this proceeding.

18) S. Nakamura, Y. Toh, A. Kimura *et al.*, "Study on Fast-Neutron Capture Cross-Section by an Activation Method", 日本原子力学会「2007 秋の大会」予稿集 M16 (2007).

19) M. Segawa, Y. Toh, H. Harada, *et al.*, "A New Detection System for Neutron Capture Reactions at JAEA", 日本物理学会「2007秋の大会」講演概要集　第62巻　第2号　第一分冊　65ページ (2007).

20) K. Y. Hara, H. Harada, F. Kitatani *et al.*, "Measurements of the ^{152}Sm(γ,n) Cross Section with Laser-Compton Scattering γ Rays and the Photon Difference Method", *J. Nucl. Sci. Technol.*, **44** [7], 938 (2007).

21) C. Forssen, F.S. Dietrich, J. Escher, *et al.*, "Determining neutron capture cross sections via the surrogate reaction technique", Phys. Rev. C **75**, 055807 (2007).

22) H. Makii, in this proceeding.

2.4 Nuclear data measurement project at J-PARC MLF

Yoshiaki Kiyanagi

Graduate School of Engineering, Hokkaido University, Japan

E-mail:Kiyanagi@qe.eng.hokudai.ac.jp

Abstract: Nuclear data of LLFP and MA are important for the future nuclear systems. J-PARC MLF is one of the most intense pulsed neutron sources in the world and can be utilized for the nuclear data measurements. A project to install a beam line for the nuclear data measurements is under progress. Here, the outline of the project and the present status of the beam line development is described.

1. Introduction

Advanced reactor systems such as fast breeder reactors and accelerator driven systems which are used for transmutation of long lived fission products (LLFP) and minor actinide (MA) are now under planning, which will be very useful for reducing MA and LLFP, and also for public acceptance if considering the increasing use of the nuclear power plants in future. For the optimum design of the advanced reactor systems, precise nuclear data are indispensable.

In Japan now being constructed is the high intensity neutron source, 1MW power JSNS (Japan Spallation Neutron source) in the material and life science facility (MLF) at J-PARC (Japan-Proton Accelerator Research Complex). The produced neutron intensity is very high and expected to be a little bit lower than 1.4 MW power SNS in USA, which is under commissioning now. Therefore, it is good opportunity to utilize JSNS for the nuclear data measurements. We are promoting a project, "Study on nuclear data by using a high intensity pulsed neutron source for advanced nuclear systems" entrusted by MEXT in order to measure the nuclear data of MA, LLFP and relating nuclides. Outline of this project will be described next chapter.

Major part of this project is the measurements of the neutron capture cross section of MA and LLFP at J-PARC MLF. So, we are now preparing the experimental equipments and shields for the measurements. The samples we are now considering are Cm as MA, and Zr-93, Tc-99 and so on as LLFP. Main detector is the high resolution Ge detector system covering large solid angle and the improvement of this system is being performed and shields for neutrons and gamma-rays are also being placed. The sample preparation is important part of this kind of measurements, so the MA and LLFP samples are carefully designed, purchased and inspected. In 2008 the first beam will be provided at J-PARC MLF. We are preparing the experimental setup to start the commissioning just after the first beam.

Here, I would like to explain the outline of the project and present status of the project concerning mainly to the J-PARC nuclear data measurements.

2. Outline of the project

The project is being performed by 8 organizations, Hokkaido University, Tokyo Institute of Technology, JAEA, Tohoku University, Kyoto University, Nagoya University, AIST, and Konan University. This project consists of (1) J-PARC experiments, (2) Experiments at other facilities, (3) Sample preparation, and (4) Evaluation of nuclear data, construction of sensitivity analysis system, and benchmark calculation. The experiments at other facilities are divided into two categories. One is cross section measurements complementally supporting the J-PARC experiments, namely, the thermal neutron capture cross section for stable nuclei, the neutron cross section relating LLFP, and the capture cross section measurements using the inverse reaction, (γ,n). The last one is unique method to get the capture cross section information of the samples which can not be prepared. The other is the fission experiments, namely, the first part of this is fission cross section measurements of MA and mass distribution measurements, and the second is decay heat measurements. The sample preparation is executed for the capture cross section measurements and also the fission cross section measurements of MA. Concerning to the last item, we are aiming at construct the user friendly sensitivity analysis systems to supply the new and existing reliable cross section data for the design of the advanced nuclear systems.

3. Structure of J-PARC

J-PARC is consisted of several facilities as shown in Fig. 1(1), hadron experimental facility, neutrino facility, and materials and life science facility (MLF). In future accelerator-driven transmutation experimental facility is also planed to construct. Neutron and muon beam experiments will be performed at MLF. There are three hydrogen moderators in JSNS. Two moderators for the high resolution experiments, a decoupled and a decoupled-poison moderator, sit above the mercury target, and a high intensity type moderator, a coupled hydrogen moderator, is placed under the target. The target-moderator-reflector system is shown in Fig.2(1). The moderators and the target are surrounded by beryllium reflector. 23 independent neutron beams are supplied for the experiments. The beam line No.4, BL04 was assigned to the nuclear data measurements, and BL04 is looking at the high intensity type moderator(2-4).
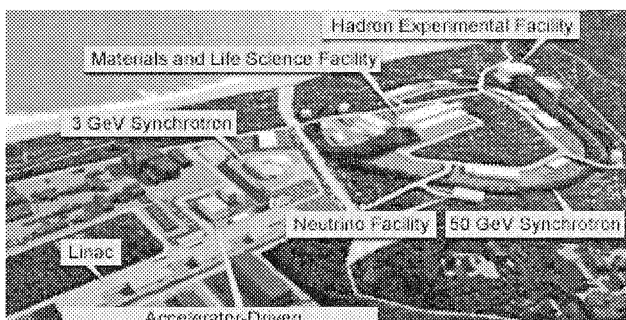

Fig. 1 Bird's eye view of J-PARC. JSNS is in the Material and Life Science Facility.
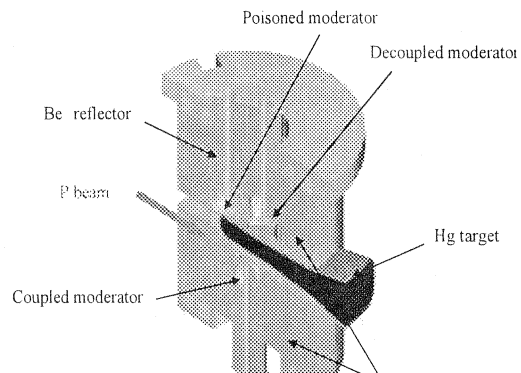
Fig. 2 Target-moderator-reflector system of JSNS. The coupled moderator under the target supplies the neutron to BL04.

4. Present status of the preparation concerning to J-PARC experiments

The moderator used is placed under the target, so the spatial distribution of neutrons on the moderator surface is expected to be asymmetric. We performed a simulation experiments at the electron linac facility at Hokkaido University to know the spatial distribution and to verify the simulation calculations. The simulation experiments showed the asymmetric feature of the spatial distribution, where the intensity decreased with increasing the distance from the target, and become flatter with decreasing the energy. The same tendency was observed in the simulation results obtained for the experimental setup, indicating that the simulation calculation gave correct answer for the spatial distribution. After then, we performed simulation calculation on the JSNS moderator. Figure 3 shows the results of the spatial distribution of the neutrons from the coupled moderator. The results clearly show the higher intensity toward the target side and that the tendency become mild with decreasing the energy as discussed above. Further study on the intensity distribution at the sample position was performed, and the beam line height was determined by using these data.
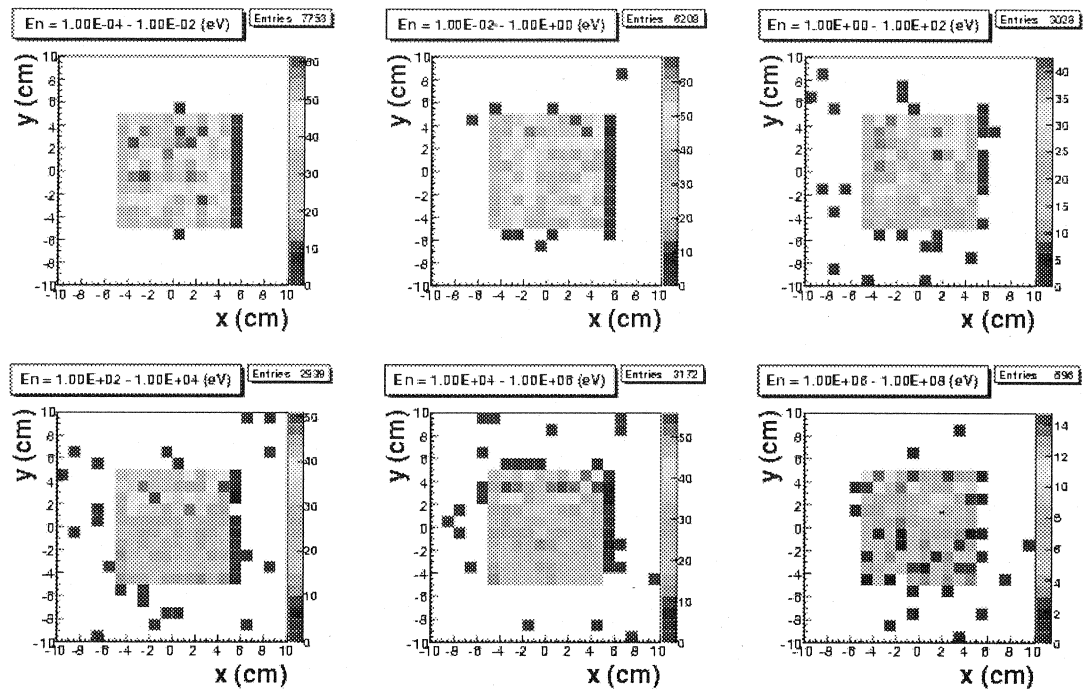
Fig. 3 Intensity map near the moderator surface of the coupled moderator. x is horizontal orientation and y is vertical orientation. The target sit over the top of the y axis. Upper part intensity is higher in the higher energy case (see lower 3 cases) and the asymmetry become mild with decreasing the energy (see upper 3 case).

The shield calculation of beam line is very important, so we performed the Monte Carlo calculation by using the Phits code(5). The outline of the beam line shield is shown in Fig. 4. The Ge detector system will be placed in the middle part of the shield, and a scintillation detector and beam monitor systems will be set in the downstream part. The shielding calculation was done in many cases, and the results shown in

Fig. 5 is the case where a sample was set at the proper position on the beam line, which indicated that the shield including iron, borax-resin and concrete in the upstream and the middle part and the borax-resin and concrete in the downstream part had enough shielding performance.

The Ge detector system was used to be utilized at the electron linac at Kyoto University. However, the neutron intensity at MLF is much higher than this facility, and also it is expected that the sample to be measured may include other nuclei as impurities. Therefore, some improvements are required for the detector system. The existing 4 cluster detectors are exchanged by 8 coaxial Ge detectors to improve the accuracy identifying the nuclei, a detector shield is placed around the detector to get good S/N, and high-speed data acquisition systems are being developed for high counting rate measurements at MLF. The improvement will be scheduled to be completed at the beginning of FY 2009.

Complementary measurements were performed for the stable nuclei at Kyoto University.

Fig. 4 Structure of the shield of BL04 beam line. This consists of mainly three parts: Upstream, middle part and downstream fundamental shield. Beam stop is placed at the end of beam line.
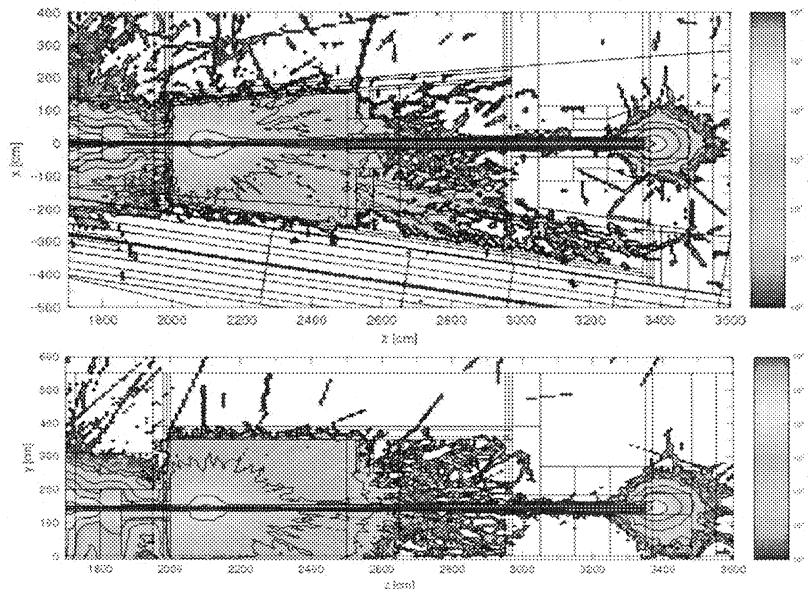
Fig. 5 Calculated results of neutron shield. Upper figure is for horizontal and lower for vertical case.

Figure 6 shows examples of cross section data for Pd-105 and Pd-108. There exists difference between the present results and JENDL data and detailed analysis is under progress. Furthermore, it is verified that by

using time gate applied at a certain region of time-of-flight we can identify the γ-ray signals from each nucleus.

The samples are being carefully prepared and the impurities are analyzed. Samples prepared are
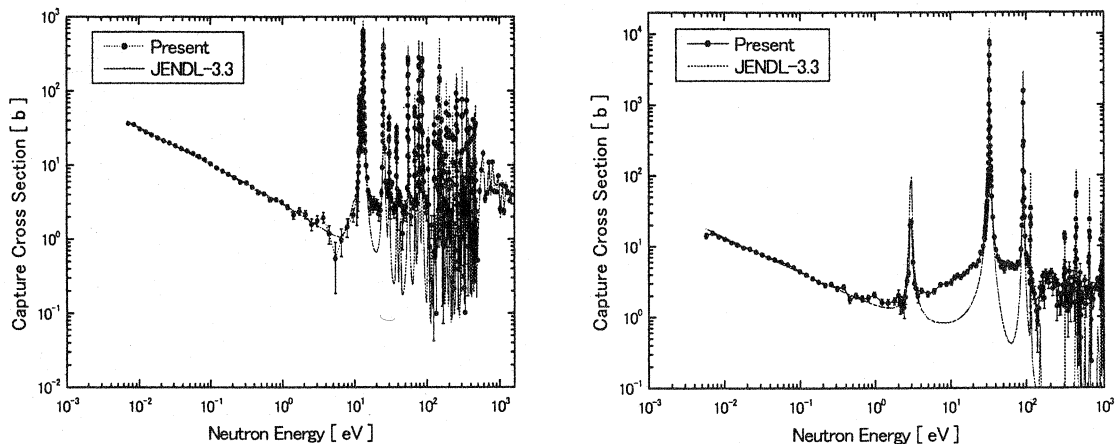
Fig.6 Capture cross section data for Pd-105 and Pd-108 compared with JENDL-3.3

following: Cm-244, Cm-246, Tc-99, Zr-93, Zr-96, Pd-105 and Pd-108 for the capture experiments, and Cm-245 and Cm-248 for the fission cross section measurements. Tc-99 sample was analyzed as shown in Fig. 7 and found was that the effect of the impurity on the cross measurement was very small, since no peaks other than Tc-99 were observed. It was
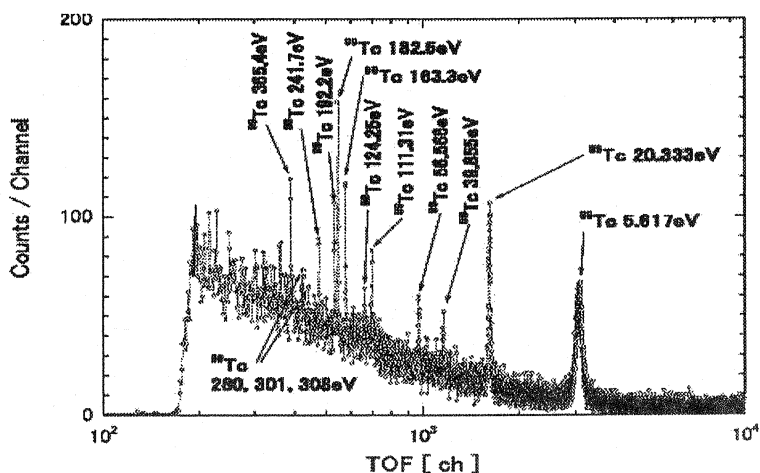
Fig. 7 Time of flight spectra of Tc-99 neutron capture.

indicated that the Cm-244 sample included Cm-243 and Cm-245 by γ-ray analysis and a method to decrease these γ-rays from impurity nuclei is discussed.   The preparation is still continuing.

5. Conclusion

The fundamental shield of BL04 will be completed until end of FY 2007.   The detector improvement and the sample preparation are also under progress.   We will start the commissioning after the beam delivery scheduled in 2008, and have to perform many things before the sample measurements.

The instruments for the measurements at other facilities are almost prepared and the measurements are Fig.

now under progress. The last items concerning to the nuclear data evaluation and so on are proceeding according to schedule or earlier.

References

(1) J-PARC home page, http://j-parc.jp/.

(2) Y.Kiyanagi, N. Watanabe and H. Iwasa, Nuclear Instrument and Methods in Physics Research, A312, 561-570 (1992).

(3) Y. Kiyanagi, M. Ooi, H. Ogawa and M. Furusaka, J. Neutron Res., 11, 3-11(2003).

(4)N. Watanabe, M. Harada, T. Kai, M. Teshigawara, Y. Ikeda, J. Neutron Res., 11, 13-23(2003).

(5)H. Iwase, K. Niita and T. Nakamura, J. Nucl. Sci. Technol. 39,1142-1151(2002).

2.5 Covariance Evaluation of Self-Shielding Factor and Its Temperature Gradient for Uncertainty Evaluation of Doppler Reactivity

Naohiko OTSUKA[1,2,†] , Atsushi ZUKERAN[3], Hideki TAKANO[3], Go CHIBA[4,5], and Makoto ISHIKAWA[4]

[1] *Nuclear Data Center, Japan Atomic Energy Agency, Tokai-mura, Naka-gun, Ibaraki 319-1195, Japan*
[2] *Nuclear Reaction Data Centre, Faculty of Science, Hokkaido University, Sapporo 060-0810, Japan*
[3] *Nippon Advanced Information Service Co. Ltd., Tokai-mura, Naka-gun, Ibaraki 319-1112, Japan*
[4] *Reactor Physics Analysis and Evaluation Group, Japan Atomic Energy Agency, O-arai-machi, Higashi-Ibaraki-gun, Ibaraki 311-1393, Japan*
[5] *Reactor Physics Group, Japan Atomic Energy Agency, Tokai-mura, Naka-gun, Ibaraki 319-1195, Japan*
e-mail: n.otsuka@iaea.org

Abstract

Covariances of the self-shielding factor and its temperature gradient for the uranium-238 neutron capture reaction have been evaluated from the resonance parameter covariance matrix and the sensitivity of the self-shielding factor and its temperature gradient to the resonance parameters. The resonance parameters and their covariance matrix for uranium-238 were taken from JENDL-3.3, while the sensitivity coefficients were calculated by varying resonance parameters and temperature. A set of computer code modules has been developed for the calculation of the sensitivity coefficients at numerous resonance levels. The present result shows that the correlation among resonance parameters yields a substantial contribution to the standard deviations of the self-shielding factor and its temperature gradient. In addition to the standard deviations of these quantities, their correlation matrices in the JFS-3 70 group structure are obtained. The covariance is applied to evaluation of the Doppler reactivity uncertainty for a typical 600 MWe-class sodium-cooled fast breeder reactor core.

1 Introduction

Doppler reactivity has been recognized as one of the most important safety parameters among the self-regulation characteristics of reactors, and a high accuracy in the prediction of the reactivity has been vigorously sought in reactor design. To improve the prediction accuracy in fast reactor systems, Doppler reactivities at various critical assemblies have been measured [1, 2, 3, 4, 5, 6] and analyzed [7, 8, 9].

In standard sensitivity analyses of nuclear characteristics, the relative sensitivity of a nuclear characteristic R to the infinite dilution cross section $\hat{\sigma}_\infty$, $S_{R,\sigma} = (\hat{\sigma}_\infty/R)(\partial R/\partial \hat{\sigma}_\infty)$ has been used. The sensitivity analysis system SAGEP [10] has used this relative sensitivity coefficient for improving the adjusted reactor constants with fixed self-shielding factors. This formalism is not applicable to temperature-related nuclear characteristics such as Doppler reactivity, however, because such characteristics depend on the self-shielding factor as well as the infinite dilution cross section. Regarding the temperature gradient of the self-shielding factor as a "pseudo cross section", the relative sensitivity of the temperature-related nuclear characteristic R to the temperature gradient of the self-shielding factor α, $S_{R,\alpha} = (\alpha/R)(\partial R/\partial \alpha)$, can be introduced. If the temperature gradient is defined using the logarithmic derivative of the self-shielding factor with respect to temperature, $\alpha = (1/f)(\mathrm{d}f/\mathrm{d}T)$, the coefficients $S_{R,\alpha}$ can be obtained from the sensitivity coefficients of effective neutron multiplication factor k_{eff} to the infinite dilution cross section $S_{k_{\mathrm{eff}},\sigma}$ [11].

In this background, the SAGEP system was extended to temperature-related nuclear characteristics, and an adjusted reactor constant ADJ2000 was obtained by using the coefficients $S_{R,\alpha}$ for the Doppler reactivities measured in ZPPR-9 and FCAXVII-1 experiments [11, 12].

Much effort has been devoted to evaluating nuclear data covariance [13, 14, 15, 16] for two data libraries of JENDL-3.2 [17] and JENDL-3.3 [18], and the resonance parameter covariance matrix of ^{238}U is also available for the present study. Therefore, a more precise evaluation of the uncertainty in Doppler reactivity is now possible and should be done on the basis of recent progress in nuclear data evaluation.

We report an evaluation of the covariances in the self-shielding factor f and its temperature gradient α in relation to the ^{238}U neutron capture reaction on the basis of microscopic nuclear data and newly developed computer code modules taking into account the correlation among resonance parameters [1]. We also demonstrate Doppler reactivity uncertainty for a typical 600 MWe-class sodium-cooled fast breeder reactor core evaluated with our covariances.

2 Evaluation of Covariances of the Self-Shielding Factor and its Temperature Gradient

We evaluate the covariances of the self-shielding factor $\delta f_{i,c}^g(T)/f_{i,c}^g(T)$ and its temperature gradient $\delta\alpha_{i,c}^g(T)/\alpha_{i,c}^g(T)$ for the ^{238}U neutron capture reaction. Hereafter, we omit the suffix i for isotope and c for reaction channel. Error propagation from resonance parameters to the self-shielding factor and its temperature gradients are

$$\theta_{gg'}\frac{\delta f^g}{f^g}\frac{\delta f^{g'}}{f^{g'}} = \sum_{i,j}\frac{x_i}{f^g}\frac{\partial f^g}{\partial x_i}\frac{x_j}{f^{g'}}\frac{\partial f^{g'}}{\partial x_j}\rho_{ij}\frac{\delta x_i}{x_i}\frac{\delta x_j}{x_j} = \sum_{i,j}s_i^g s_j^{g'}\rho_{ij}\frac{\delta x_i}{x_i}\frac{\delta x_j}{x_j}, \tag{1}$$

$$\tau_{gg'}\frac{\delta\alpha^g}{\alpha^g}\frac{\delta\alpha^{g'}}{\alpha^{g'}} = \sum_{i,j}\frac{x_i}{\alpha^g}\frac{\partial\alpha^g}{\partial x_i}\frac{x_j}{\alpha^{g'}}\frac{\partial\alpha^{g'}}{\partial x_j}\rho_{ij}\frac{\delta x_i}{x_i}\frac{\delta x_j}{x_j} = \sum_{i,j}S_i^g S_j^{g'}\rho_{ij}\frac{\delta x_i}{x_i}\frac{\delta x_j}{x_j}, \tag{2}$$

where

$\theta_{gg'}$: Correlation matrix of self-shielding factor $\{f^g\}$
$\tau_{gg'}$: Correlation matrix of temperature gradient $\{\alpha^g\}$
x_i : Resonance parameter $\boldsymbol{x}=\{x_i\}=(E_{r,1},\Gamma_{n,1},\Gamma_{\gamma,1},...)$
ρ_{ij} : Correlation matrix of resonance parameter $\boldsymbol{x}$
δx_i : Absolute standard deviation of resonance parameter x_i
s_i^g : Relative sensitivity coefficient of self-shielding factor f^g to resonance parameter x_i
S_i^g : Relative sensitivity coefficient of temperature gradient α^g to resonance parameter x_i

The relative sensitivity coefficients s_i^g and S_i^g are defined as

$$s_i^g(\boldsymbol{x},T) = \frac{x_i}{f^g(\boldsymbol{x},T)}\frac{\partial f^g(\boldsymbol{x},T)}{\partial x_i}, \tag{3}$$

$$S_i^g(\boldsymbol{x},T) = \frac{x_i}{\alpha^g(\boldsymbol{x},T)}\frac{\partial\alpha^g(\boldsymbol{x},T)}{\partial x_i}. \tag{4}$$

The summations in Eqs. (1) and (2) are taken over all resolved resonance parameters. By equating g and g' in Eqs. (1) and (2), we obtain the relative standard deviations of the self-shielding factor and its temperature gradient in the g-th group,

$$\left(\frac{\delta f^g}{f^g}\right)^2_{\text{tot}} = \sum_{i,j}s_i^g s_j^g\rho_{ij}\frac{\delta x_i}{x_i}\frac{\delta x_j}{x_j}, \tag{5}$$

$$\left(\frac{\delta\alpha^g}{\alpha^g}\right)^2_{\text{tot}} = \sum_{i,j}S_i^g S_j^g\rho_{ij}\frac{\delta x_i}{x_i}\frac{\delta x_j}{x_j}. \tag{6}$$

---

[1] See [19] for details in methods and results of this work.

From Eqs. (1) and (2), the correlation matrices $\theta_{gg'}$ and $\tau_{gg'}$ can be expressed as

$$\theta_{gg'} = \left(\sum_{i,j} s_i^g s_j^{g'} \rho_{ij} \frac{\delta x_i}{x_i} \frac{\delta x_j}{x_j} \right) \bigg/ \left(\frac{\delta f^g}{f^g} \frac{\delta f^{g'}}{f^{g'}} \right), \tag{7}$$

$$\tau_{gg'} = \left(\sum_{i,j} S_i^g S_j^{g'} \rho_{ij} \frac{\delta x_i}{x_i} \frac{\delta x_j}{x_j} \right) \bigg/ \left(\frac{\delta \alpha^g}{\alpha^g} \frac{\delta \alpha^{g'}}{\alpha^{g'}} \right). \tag{8}$$

In the present work, the resonance parameter set $x = \{x_i\}$ and its covariance matrix V ($V_{ij} = \rho_{ij} \delta x_i \delta x_j$) are taken from the evaluated nuclear data library JENDL-3.3, while the sensitivity coefficients s_i^g and S_i^g are obtained using a newly developed code system ERRORF [20].

In the current evaluation, we take the resonance parameter set x and its covariance matrix V from evaluated nuclear data files compiled in the ENDF-6 format [21]. Among the major evaluated nuclear data libraries, JENDL-3.3 is the unique solution in the present study because the other libraries do not include the resonance parameter covariance matrix in their ^{238}U data evaluation. [2]

Sensitivity coefficients of the self-shielding factor f^g and its temperature gradient α^g with respect to the i-th resonance parameter, s_i^g and S_i^g are calculated according to their definition in Eqs. (3) and (4). We modify Eq. (3) for numerical calculation of S_i^g,

$$S_i^g(x, T) = \frac{x_i}{\alpha^g(x, T)} \frac{\partial \alpha^g(x, T)}{\partial x_i} = \frac{1}{\alpha^g(x, T)} \frac{\partial s_i^g(x, T)}{\partial T}. \tag{9}$$

The self-shielding factor $f^g(x, T)$ is obtained from the resonance parameter set x using NJOY [22]. The neutron flux $\phi(E, T, \sigma_b)$ is calculated according to the Bondarenko model,

$$\phi(E, T, \sigma_b) = \frac{C(E)}{\sigma(x, E, T) + \sigma_b}, \tag{10}$$

where $C(E)$ is a weighting function (a priori flux) for which we take an analytic form of the Maxwell distribution + $(1/E)$ + fission neutron distribution.

Calculation is done from the upper boundary of the thermal region (~ 3 eV) to the upper boundary of the resolved resonance region (10 keV) in the 70 group structure defined in the JFS-3 (JAERI-Fast Set Ver.3) format [7, 23]. Energies of upper boundaries in the 70 group structure are tabulated in **Table 1** for fast reactors.

3   Results and Discussions

3.1   Self-Shielding Factor and Temperature Gradient

The self-shielding factor f^g and its temperature gradient α^g for ^{238}U neutron capture reaction are shown in **Fig. 1**. The neutron capture cross section of ^{238}U at 300 K in JENDL-3.3 is also plotted in Fig. 1. In the figure, the correlation between the position of the resonance level and the self-shielding factor is clearly seen below 200 eV, where level spacing is wider than the energy widths of groups. Then f^g takes unity if there is no resonance level in the group except a small resonance tail effect. On the other hand, level spacing is narrower than the energy widths of groups above 200 eV, and number of levels per group gradually increases with neutron energy. The self-shielding factor then increases monotonically with neutron energy and approaches unity. Temperature gradient α^g is in the order of 10^{-4} if resonance levels exist in the g-th energy group. Below 200 eV, the temperature gradient is enhanced around positions of the resonance levels although the self-shielding factor f^g shrinks due to neutron absorption by resonance. However, the trend is masked by many resonance levels above 200 eV.

3.2   Uncertainties in Self-Shielding Factor and Temperature Gradient

The relative standard deviation (1σ) of self-shielding factor $\delta f^g / f^g$ and its temperature gradient $\delta \alpha^g / \alpha^g$ are shown in **Fig. 2** (labeled "tot"). The correspondence of the position of resonance level to $\delta f^g / f^g$ and $\delta \alpha^g / \alpha^g$ is still visible, as we see in Fig. 1; however, $\delta f^g / f^g$ and $\delta \alpha^g / \alpha^g$ are also affected by the resonance levels outside the g-th group.

---

[2]The resonance parameter set and its covariance matrix of ^{238}U evaluated for JENDL-3.2 is adopted in JENDL-3.3

Table 1: Upper energy boundaries in the JFS-3 70 group structure [23]. "1.00000E+07" means "1.00000×10^7 eV".

| Group	Energy	Group	Energy	Group	Energy	Group	Energy
1	1.00000E+07	21	6.73795E+04	41	4.53999E+02	61	3.05902E+00
2	7.78801E+06	22	5.24752E+04	42	3.53575E+02	62	2.38237E+00
3	6.06531E+06	23	4.08677E+04	43	2.75365E+02	63	1.85539E+00
4	4.72367E+06	24	3.18278E+04	44	2.14454E+02	64	1.44498E+00
5	3.67879E+06	25	2.47875E+04	45	1.67017E+02	65	1.12535E+00
6	2.86505E+06	26	1.93045E+04	46	1.30073E+02	66	8.76425E-01
7	2.23130E+06	27	1.50344E+04	47	1.01301E+02	67	6.82560E-01
8	1.73774E+06	28	1.17088E+04	48	7.88932E+01	68	5.31579E-01
9	1.35335E+06	29	9.11882E+03	49	6.14421E+01	69	4.13994E-01
11	8.20850E+05	30	7.10174E+03	50	4.78512E+01	70	3.22419E-01
12	6.39279E+05	31	5.53084E+03	51	3.72665E+01		
13	4.97871E+05	32	4.30743E+03	52	2.90232E+01		
14	3.87742E+05	33	3.35463E+03	53	2.26033E+01		
15	3.01974E+05	34	2.61259E+03	54	1.76035E+01		
16	2.35177E+05	35	2.03468E+03	55	1.37096E+01		
10	1.05399E+06	36	1.58461E+03	56	1.06770E+01		
17	1.83156E+05	37	1.23410E+03	57	8.31529E+00		
18	1.42642E+05	38	9.61117E+02	58	6.47595E+00		
19	1.11090E+05	39	7.48518E+02	59	5.04348E+00		
20	8.65170E+04	40	5.82947E+02	60	3.92786E+00		
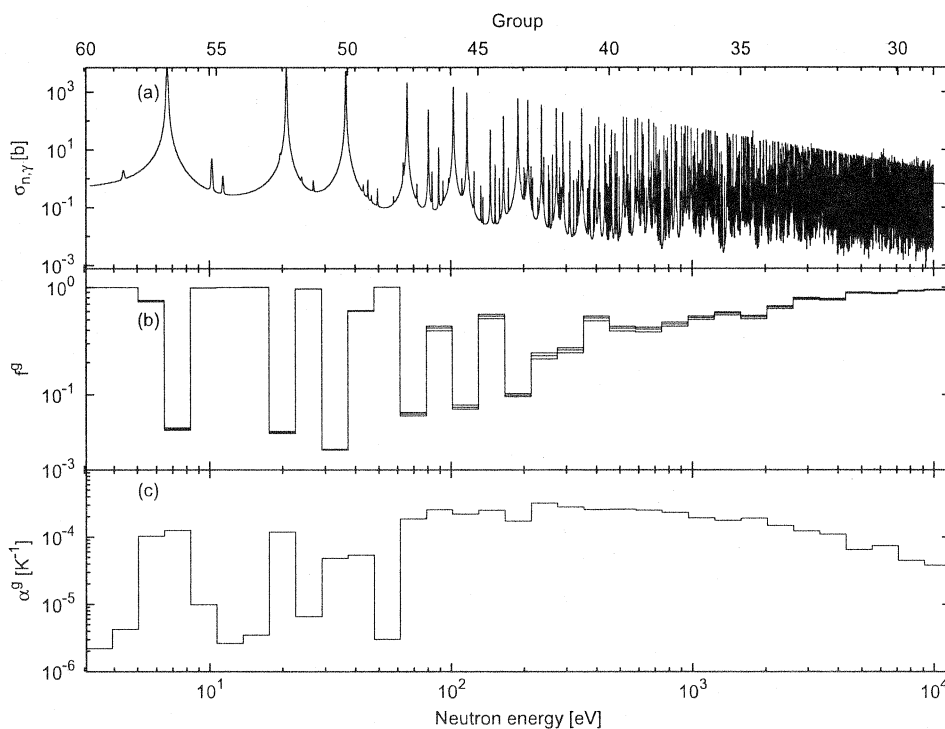
Figure 1: (a) Neutron capture cross section of ^{238}U in JENDL-3.3 at 300 K. (b) Self-shielding factor f^g for ^{238}U neutron capture reaction in the JFS-3 group structure (T=600, 800, 1000 K, σ_b=37 barn). (c) Same as (b), but for temperature gradient α^g at 800 K.
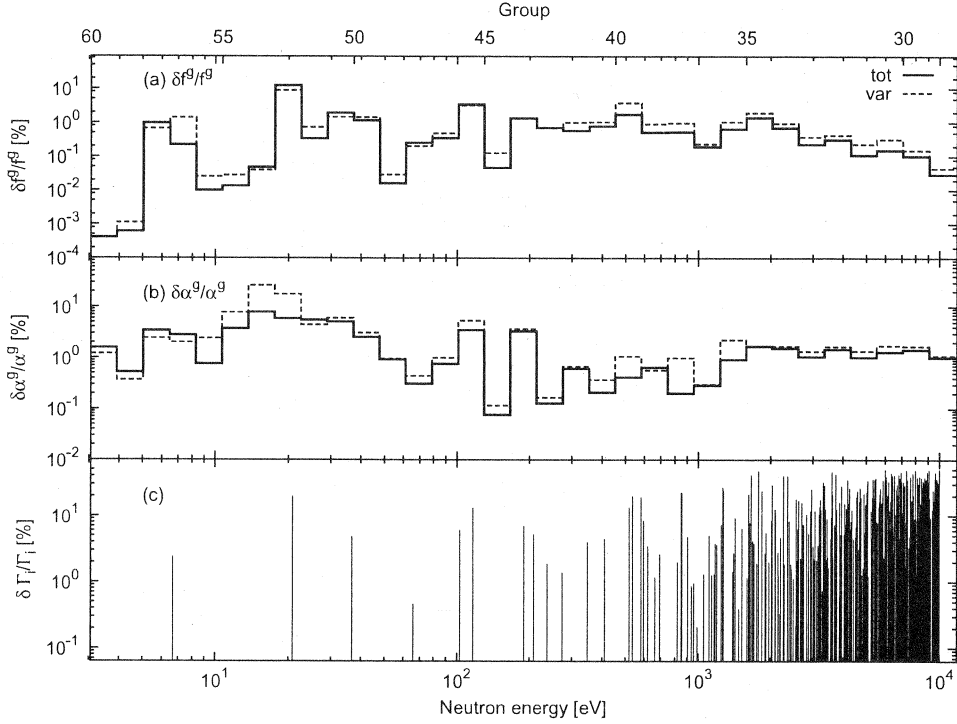
Figure 2: (a) Relative standard deviation (1σ) in self-shielding factor $\delta f^g/f^g$ for ^{238}U neutron capture reaction in the JFS-3 group structure (T=800 K, σ_b=37 barn). "tot" gives the contribution of both variances and covariances of all resonance parameters. "var" is the same as "tot", except that correlations are ignored. (b) Same as (a), but for temperature gradient $\delta\alpha^g/\alpha^g$. (c) Relative standard deviations (1σ) in neutron width $\delta\Gamma_{n,i}/\Gamma_{n,i}$ (upper) and capture width $\delta\Gamma_{\gamma,i}/\Gamma_{\gamma,i}$ (lower) compiled in JENDL-3.3 [14] for neutron-induced ^{238}U reaction.

Above 200 eV, fluctuations in $\delta f^g/f^g$ and $\delta\alpha^g/\alpha^g$ are smaller than those at lower energy, and they are less than several percent.

In order to investigate the contributions of diagonal elements (variance) and off-diagonal elements (covariance) in matrix V to $(\delta f^g/f^g)^2_{\rm tot}$ and $(\delta\alpha^g/\alpha^g)^2_{\rm tot}$, we decompose them to two terms:

$$\left(\frac{\delta f^g}{f^g}\right)^2_{\rm tot} = \left(\frac{\delta f^g}{f^g}\right)^2_{\rm var} + \rho_{\rm cov}[s^g \delta x/x], \tag{11}$$

$$\left(\frac{\delta\alpha^g}{\alpha^g}\right)^2_{\rm tot} = \left(\frac{\delta\alpha^g}{\alpha^g}\right)^2_{\rm var} + \rho_{\rm cov}[S^g \delta x/x], \tag{12}$$

where the terms "var" and "cov" for the self-shielding factor f^g are defined as

$$\left(\frac{\delta f^g}{f^g}\right)^2_{\rm var} = \sum_{l\in L_g}\sum_{i,j\in M_l} s^g_i s^g_j \rho^l_{ij}\frac{\delta x_i}{x_i}\frac{\delta x_j}{x_j}\delta_{ij} = \sum_i (s^g_i)^2\left(\frac{\delta x_i}{x_i}\right)^2, \tag{13}$$

$$\rho_{\rm cov}[s^g \delta x/x] = \sum_{l\in L_g}\sum_{i,j\in M_l} s^g_i s^g_j \rho^l_{ij}\frac{\delta x_i}{x_i}\frac{\delta x_j}{x_j}(1-\delta_{ij}) \tag{14}$$

(δ_{ij} is Kronecker's delta). Note that $\rho^l_{ij} = 1$ if $i = j$. Similar terms can also be defined for the temperature gradient α^g. The contribution of variance is shown in Fig. 2, labeled "var." The significant contribution of correlation between resonance parameters is visible in the deviation of "tot" from "var." This shows that the correlation among resonance parameters should be taken into account in the evaluation of the uncertainties.

In the evaluation of uncertainty in Doppler reactivity, the correlation matrices of self-shielding factor and its temperature gradient among groups are required. The obtained correlation matrices $\theta_{gg'}$ and $\rho_{gg'}$ given in Eqs. (7) and (8) are tabulated in the main publication [19].
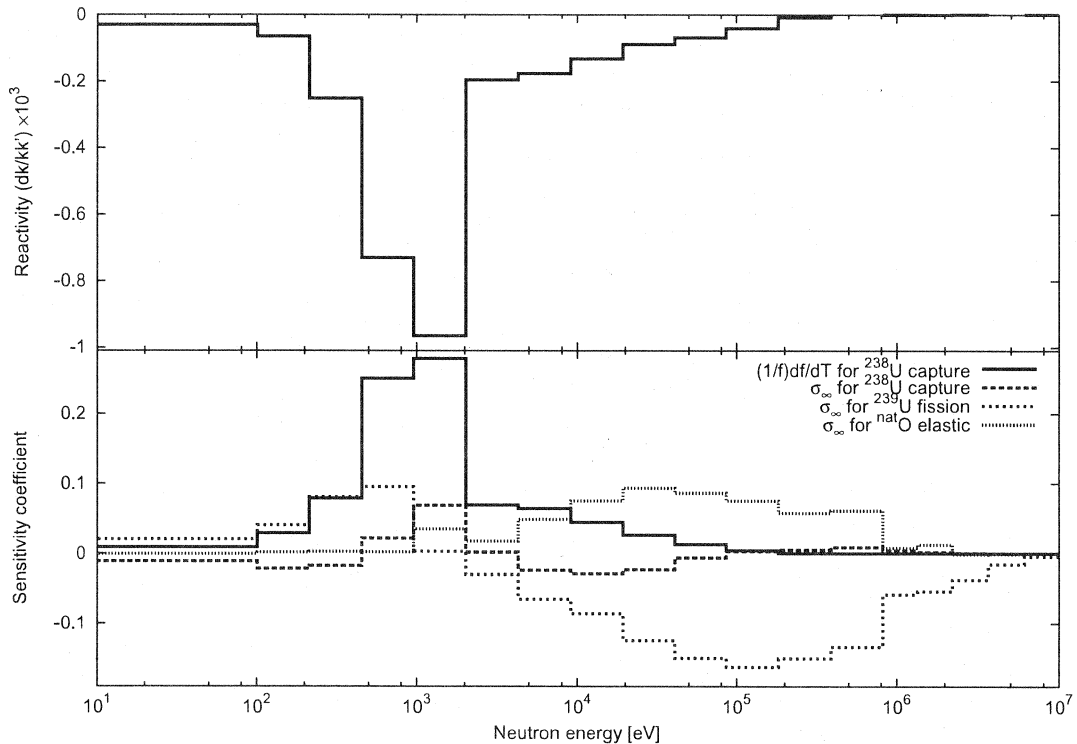
Figure 3: Upper: Energy break down of the whole-core Doppler reactivity for the 600 MWe-class sodium-cooled fast breeder reactor core. Lower: Sensitivity coefficients of the Doppler reactivity for the 600 MWe-class sodium-cooled fast breeder reactor core.

4   Evaluation of Doppler reactivity uncertainty for a 600 MWe-class sodium-cooled fast breeder reactor core

The covariance obtained in the present work is applied to evaluation of Doppler reactivity uncertainty of a typical sodium-cooled fast breeder reactor core which specification is as follows (BOEC - beginning of equilibrium cycle):

- Thermal power: 1,600 MWt

- Operating cycle: 365 days

- Pu ratio: 16.5% (inner core) / 20.5% (outer core)

- Pu composition: 3%(238) / 53%(239) / 25%(240) / 12%(241) / 7%(242)

- Burn-up reactivity loss: 2.5% dk/kk'/cycle

- Doppler coefficient: $-8.0 \times 10^{-3} \, Tdk/dT$ (BOEC)

- Sodium void reactivity: 4.6\$ (whole core, BOEC)

- Prompt neutron lifetime: 0.41 μs (BOEC)

- Beta effective: 3.8×10^{-3} (BOEC)

The energy break down of the whole-core Doppler reactivity obtained with the ordinary exact perturbation theory is shown in the upper panel of **Fig. 3**, where we found that the most of the Doppler reactivity occurs in the energy range from 500 eV to 2 keV. The sensitivity coefficients of the Doppler reactivity related to the temperature gradient of ^{238}U capture as well as infinite dilution cross sections of major nuclides and reactions are depicted in the lower panel of Fig. 3, which were calculated by the generalized perturbation theory [24, 25, 26]. The sensitivity of the temperature gradient and the energy break down of the reactivity show similar energy dependence but it is not for infinite dilution cross sections, because the temperature gradient and infinite dilution cross sections mainly cause the direct and indirect effect to the reactivity, respectively.

The nuclide- and reaction-wise contributions to the Doppler reactivity uncertainty for the core evaluated with the present covariance of the temperature gradient are shown in **Table 2**. The total uncertainty of the Doppler reactivity is

Table 2: Nuclide- and reaction-wise contributions to the whole-core Doppler reactivity for the 600 MWe-class fast breeder reactor core (σ_∞: Infinite dilution cross section, β: Delayed fission neutron multiplicity, χ: Fission neutron spectrum, ν: Prompt fission neutron multiplicity, μ: Cosine of outgoing neutron)

Nuclide	Reaction	Quantity	$\Delta R/R$ (%)	Contribution
^{239}Pu	Fission	σ_∞	1.84	29.3
^{241}Pu	Fission	β	1.36	16.0
^{238}U	Inelastic	σ_∞	1.15	11.4
^{239}Pu	Fission	χ	1.06	9.7
^{238}U	Fission	β	1.00	8.7
^{239}Pu	Fission	β	0.74	4.7
^{239}Pu	Capture	σ_∞	0.70	4.2
^{23}Na	Elastic	σ_∞	0.63	3.4
^{nat}Fe	Inelastic	σ_∞	0.57	2.8
^{16}O	Elastic	σ_∞	0.56	2.7
^{240}Pu	Fission	β	0.35	1.1
^{nat}Fe	Elastic	σ_∞	0.34	1.0
^{239}Pu	Inelastic	σ_∞	0.27	0.6
^{23}Na	Capture	σ_∞	0.26	0.6
^{241}Pu	Fission	σ_∞	0.26	0.6
^{238}U	Capture	σ_∞	0.24	0.5
^{242}Pu	Fission	β	0.23	0.5
^{238}U	Capture	$(1/f)\mathrm{d}f/\mathrm{d}T$	0.23	0.5
^{240}Pu	Fission	σ_∞	0.22	0.4
^{239}Pu	Fission	ν	0.15	0.2
^{nat}Fe	Capture	σ_∞	0.14	0.2
^{238}U	Fission	ν	0.14	0.2
^{240}Pu	Fission	ν	0.14	0.2
^{240}Pu	Capture	σ_∞	0.13	0.1
^{238}U	Fission	σ_∞	0.11	0.1
^{238}U	Elastic	σ_∞	0.11	0.1
^{241}Pu	Capture	σ_∞	0.08	0.1
^{23}Na	Inelastic	σ_∞	0.07	0.0
^{nat}Fe	Elastic	μ	0.05	0.0
^{235}U	Fission	σ_∞	0.05	0.0
^{235}U	Fission	β	0.04	0.0
^{23}Na	Elastic	μ	0.03	0.0
^{235}U	Capture	σ_∞	0.03	0.0
^{16}O	Elastic	μ	0.02	0.0
^{241}Pu	Fission	ν	0.02	0.0
^{235}U	Fission	χ	0.02	0.0
^{16}O	Inelastic	σ_∞	0.01	0.0
^{nat}Cr	Elastic	μ	0.01	0.0
^{nat}Ni	Elastic	μ	0.01	0.0
^{235}U	Fission	ν	0.01	0.0
^{235}U	Inelastic	σ_∞	0.01	0.0
^{238}U	Elastic	μ	0.01	0.0
^{12}C	Capture	σ_∞	0.00	0.0
^{239}Pu	Elastic	μ	0.00	0.0
FP(^{239}Pu)	Capture	σ_∞	0.00	0.0
Total			3.40	100.0

3.4% (1σ). where the major contributions come from ^{239}Pu fission and ^{238}U inelastic cross sections, delayed neutron fractions of ^{241}Pu and ^{238}U (β), and ^{239}Pu fission spectrum (χ). The temperature-gradient of ^{238}U capture contributes to the total Doppler reactivity uncertainty only by 0.5% in the present case.

5 Conclusions

We have derived covariances of self-shielding factors and their temperature gradients from the resonance parameter covariance matrix and the sensitivity coefficients of the self-shielding factor and its temperature gradient with respect to resonance parameters in JENDL-3.3. In order to calculate the sensitivity coefficients for nuclides with numerous resonance levels according to the derived equations, a new system ERRORF has been developed to obtain covariance matrices of self-shielding factor and its temperature gradient. This system was then applied to the evaluation of covariances in the self-shielding factor and its temperature gradient for ^{238}U neutron capture reaction at T=800 K and background cross section σ_b=37 barn in the JFS-3 70 group structure. We have shown that uncertainties in both the self-shielding factor and temperature gradient are substantially reduced if we include the correlation among resonance parameters. Thus, we can conclude that the correlation among resonance parameters has a crucial role in the precise evaluation of uncertainty in the self-shielding factor and its temperature gradient. Note that these values will not directly influence the uncertainty in Doppler reactivity due to the fact that the uncertainty of each group is weighted using the averaged flux and other quantities of the group.

We also evaluate the Doppler reactivity uncertainty for a 600 MWe-class sodium cooled fast breeder reactor core. This results in rather small contribution induced from the temperature gradient of the ^{238}U capture self-shielding factor, compared with those from other nuclear data such as some infinite dilution cross sections, delayed neutron fraction, and fission spectrum.

Acknowledgments

References

[1] G. J. Fischer, H. H. Hummel, J. R. Folkrod, D. A. Meneley, *Experimental Results for U^{238} Doppler Measurements in Fast Reactor Spectra*, ANL-6792, 885 (1963).

[2] G. J. Fischer, D. A. Meneley, R. N. Hwang, E. F. Groh, C. E. Till, "Doppler effect measurements in plutonium-fueled fast power breeder reactor spectra," *Nucl. Sci. Eng.*, **25**, 37 (1966).

[3] R. B. Pond, J. W. Daughtry, C. E. Till, E. F. Groh, C. D. Swanson, P. H. Kier, *Plutonium and ^{238}U Doppler Measurements in ZPR-9 Assembly 26, FTR-3*, ANL-7710, 73 (1971).

[4] L. Barleon, E. A. Fischer, "Small-sample Doppler effect measurements and their interpretation in fast reactor spectra," *Nucl. Sci. Eng.*, **47**, 247 (1972).

[5] S. K. Bhattacharyya, R. B. Pond, "Measurement of the uranium-238 Doppler effect in gas-cooled fast reactor critical assemblies," *Nucl. Sci. Eng.*, **65**, 548 (1978).

[6] T. Mukaiyama, S. Okajima, "Neutron spectrum dependence of natural UO$_2$ Doppler effect measured in FCA," *J. Nucl. Sci. Technol.*, **22**, 243 (1985).

[7] H. Takano, A. Hasegawa, M. Nakagawa, Y. Ishiguro, S. Katsuragi, *JAERI Fast Reactor Group Constants Set, Version II*, JAERI 1255 (1978).

[8] K. Yokoyama, M. Ishikawa, H. Oigawa, S. Iijima, *Development of a Standard Database for FBR Core Nuclear Design (IX) - Analysis of FCA XVII-1 Experiments -*, JNC TY 9400 98-001 (1998).

[9] M. Ishikawa, "Consistency evaluation of JUPITER experiment and analysis for large FBR cores," *Proc. Int. Conf. Physics of Reactors (PHYSOR96)*, Mito, Japan, Sept. 16–20, 1996, Vol. 2, E-36 (1996).

[10] A. Hara, T. Takeda, Y. Kikuchi, *SAGEP: Two-Dimensional Sensitivity Analysis Code Based on Generalized Perturbation Theory*, JAERI-M 84-027 (1984).

[11] M. Ishikawa, K. Sugino, W. Sato, K. Numata, "Development of a unified cross-section set ADJ2000 based on adjustment technique for fast reactor analysis," *J. Nucl. Sci. Technol. Suppl.*, **2**, 1073 (2002).

[12] M. Ishikawa, K. Numata, W. Sato, K. Sugino, *Development of the Unified Cross-Section Set ADJ2000 for Fast Reactor Analysis*, JNC TN9400 2001-071 (2001).

[13] T. Kawano, K. Shibata, "Uncertainty analyses in the resolved resonance region of ^{235}U, ^{238}U, and ^{239}Pu with the Reich-Moore *R*-matrix theory for JENDL-3.2," *J. Nucl. Sci. Technol.*, **39**, 807 (2002).

[14] T. Kawano, K. Shibata, *Evaluation of Covariances for Resolved Resonance Parameters of ^{235}U, ^{238}U, and ^{239}Pu in JENDL-3.2*, JAERI-Research 2003-001 (2003).

[15] T. Nakagawa, K. Shibata, "Estimation of covariance matrices for nuclear data of ^{237}Np, ^{241}Am and ^{243}Am," *J. Nucl. Sci. Technol.*, **42**, 984 (2005).

[16] K. Shibata, T. Nakagawa, "Uncertainty analyses of neutron cross sections for nitrogen-15, lead-206, 207, 208, bismuth-209, plutonium-238, americium-242m and curium-244 in JENDL-3.3," *J. Nucl. Sci. Technol.*, **44**, 1 (2007).

[17] T. Nakagawa, K. Shibata, S. Chiba, T. Fukahori, Y. Nakajima, Y. Kikuchi, T. Kawano, Y. Kanda, T. Ohsawa, H. Matsunobu, M. Kawai, A. Zukeran, T. Watanabe, S. Igarasi, K. Kosako, T. Asami, "Japanese Evaluated Nuclear Data Library Version 3 Revision-2: JENDL-3.2," *J. Nucl. Sci. Technol.*, **32**, 1259 (1995).

[18] K. Shibata, T. Kawano, T. Nakagawa, O. Iwamoto, J. Katakura, T. Fukahori, S. Chiba, A. Hasegawa, T. Murata, H. Matsunobu, T. Ohsawa, Y. Nakajima, T. Yoshida, A. Zukeran, M. Kawai, M. Baba, M. Ishikawa, T. Asami, T. Watanabe, Y. Watanabe, M. Igashira, N. Yamamuro, H. Kitazawa, N. Yamano, H. Takano, "Japanese Evaluated Nuclear Data Library Version 3 Revision-3: JENDL-3.3," *J. Nucl. Sci. Technol.*, **39**, 1125 (2002).

[19] N. Otuka, A. Zukeran, H. Takano, G. Chiba, M. Ishikawa, "Covariance analyses of self-shielding factor and its temperature gradient for uranium-238 neutron capture reaction," *J. Nucl. Sci. Technol.*, **45**, 195 (2008).

[20] N. Otuka, A. Zukeran, T. Takano, G. Chiba, M. Ishikawa, *ERRORF - A Code to Calculate Covariance of Self-Shielding Factor and its Temperature Coefficient* (to be published in JAEA-Data/Code). All modules except NJOY are available on request.

[21] M. Herman (ed.), *ENDF-6 Formats Manual*, BNL-NCS-44945-05-Rev (2005).

[22] R. E. MacFarlane, D. W. Muir, *The NJOY Nuclear Data Processing System, Version 91*, LA-12740-M (1994).

[23] H. Takano, K. Kaneko, *Revision of Fast Reactor Group Constant Set JFS-3-J2*, JAERI-M 89-141 (1989).

[24] L. N. Usachev, "Perturbation theory for the breeding ratio and for other number ratios pertaining to various reactor processes," *J. Nucl. Energy A/B*, **18**, 571 (1964).

[25] A. Gandini, M. Salvatores, G. Senza, *Analysis of fast reactors by the CIAP and GLOBPERT codes using improved perturbation methods* , ANL-7320, 304 (1966).

[26] A. Gandini, "A generalized perturbation method for Bi-linear functionals of the real and adjoint neutron fluxes," *J. Nucl. Energy*, **21**, 755 (1967).

2.6 Recent Nuclear Data Needs from Innovative Reactor Design

Makoto ISHIKAWA

Japan Atomic Energy Agency (JAEA)
4002, Narita-cho, O-arai-machi, Ibaraki 311-1393, Japan
e-mail: ishikawa.makoto@jaea.go.jp

Abstract

The Working Party on International Nuclear Data Evaluation Cooperation (WPEC) of the OECD Nuclear Energy Agency Nuclear Science Committee (NEA/NSC) has established an International Subgroup (Subgroup 26) to perform an activity in order to develop a systematic approach to define data needs for Gen-IV and, in general, for advanced reactor systems. A comprehensive sensitivity and uncertainty study has been performed to evaluate the impact of neutron cross-section uncertainty on the most significant integral parameters related to the core and fuel cycle of a wide range of innovative systems, even beyond the Gen-IV range of systems. In the present study, the integral parameter uncertainties previously calculated have been revised by the use of preliminary covariance data developed by joint efforts of several Labs within the Subgroup 26. As general features, the calculated integral parameters uncertainties, resulting from the presently assessed uncertainties on nuclear data are probably acceptable in the early phases of design feasibility studies. However, later conceptual and design optimization phases of selected reactor and fuel cycle concepts, will need improved data and methods, in order to reduce margins, both for economical and safety reasons. For this purpose, a target accuracy assessment has been also performed in order to give a preliminary quantitative evaluation of nuclear data improvement requirements (isotopes, nuclear reaction, energy range). The results of the assessment indicated that a careful analysis is needed in order to define the most appropriate and effective strategy for data uncertainty reduction. Priority issues are pointed out, and the role of integral experiments in order to meet requirements is underlined.

1. Introduction

Recently, several movements to develop innovative reactors and related fuel cycle systems are arising with strong international cooperation:

1) Generation IV (Gen-IV, hereafter)[1]: Concerns over energy resource availability, climate change, air quality, and energy security suggest an important role for nuclear power in future energy supplies. While the current Generation II and III nuclear power plant designs provide a secure and low-cost electricity supply in many markets, further advances in nuclear energy system design can broaden the opportunities for the use of nuclear energy. To explore these opportunities, the U.S. Department of Energy's Office of Nuclear Energy, Science and Technology has engaged governments, industry, and the research community worldwide in a wide ranging discussion on the development of next generation nuclear energy systems known as "Gen-IV" from 2001. The members of the Gen-IV International Forum (GIF) are totally 11 countries or areas in 2006: Argentina, Brazil, Canada, Euratom, France, Japan, the Republic of Korea, the Republic of South Africa, Switzerland, the United Kingdom, and the United States. The mile stone of Gen-IV project is approximately 2030, by the time, the Gen-IV reactor system would be deployable and introduced.

2) Global Nuclear Energy Partnership (GNEP, hereafter)[2]: As a part of President Bush's Advanced Energy Initiative which was declared at the beginning of 2006, GNEP seeks to develop worldwide consensus on enabling expanded use of economical, carbon-free nuclear energy to meet growing electricity demand. This will use a nuclear fuel cycle that enhances energy security, while promoting non-proliferation. It would achieve its goal by having nations with secure, advanced nuclear capabilities provide fuel services — fresh fuel and recovery of used fuel — to other nations who agree to employ nuclear energy for power

generation purposes only. The closed fuel cycle model envisioned by this partnership requires development and deployment of technologies that enable recycling and consumption of long-lived radioactive waste. GNEP would demonstrate the critical technologies needed to change the way used nuclear fuel is managed – to build recycling technologies that enhance energy security in a safe and environmentally responsible manner, while simultaneously promoting non-proliferation. By the end of 2007, the number of joined countries with GNEP increased up to 19, China, France, Japan, Russia and the United States, who are original GNEP partners, as well as Australia, Bulgaria, Ghana, Hungary, Jordan, Kazakhstan, Lithuania, Poland, Romania, Slovenia, Ukraine, Italy, Canada and Korea, signed a "Statement of Principles" in 2007, which addresses the prospects of expanding the peaceful uses of nuclear energy, including enhanced safeguards, international fuel service frameworks, and advanced technologies .

3) Fast Reactor Cycle Technology Development Project in Japan (FaCT, hereafter)[3]: In Japan, a joint team of Japan Atomic Energy Agency (JAEA) and Japan Atomic Power Company (JAPC) had conducted a comprehensive study on fast reactor cycle named "Feasibility Study on Commercialized Fast Reactor Cycle Systems (FS)" since 1999. The Phase II of the FS was finalized in Mar. 2006 by selecting a promising concept of fast reactor cycle system, namely a combination of the sodium-cooled fast reactor (SFR) with oxide fuel, the advanced aqueous reprocessing and the simplified pelletizing fuel fabrication systems. Thirteen innovative technologies were identified for further R&D to realize the concept of the commercialization FRs, and twelve for fuel cycle facilities. After the process of check and review by Japanese government, the results of the FS were confirmed. At the same time, a policy of FR cycle introduction was discussed at governmental committees the documents of which state a start-up of a demonstration fast reactor by 2025 and deployment of a commercial fast reactor cycle before 2050. Based on all of these results, a new project, the FaCT Project was launched from Apr. 2006 by the joint Japanese team focusing on development of the selected concepts.

Under these circumstances around innovative reactor development, an international expert group, "Subgroup 26 (SG26, hereafter): Nuclear Data Needs for Advanced Reactor Systems[4]" was organized in the framework of OECD/NEA Working Party on International Nuclear Data Evaluation and Cooperation (WPEC) in Sep.2005. The activity period of SG26 is Sep.2005 – Mar.2008 (Report submission to WPEC.) The final members of SG26 are, Salvatores (Coordinator, ANL, INL, CEA, FZK), Palmiotti (INL), Aliberti, Taiwo, McKnight, Don Smith (ANL), Oblozinsky (BNL), Dunn, Leal (ORNL), Kawano, Talou (LANL), Mills, Zimmerman (Nexiasolutions), Jacqmin, Rimpault (CEA), Ignatyuk (IPPE), Hogenbirk, Koning (NRG), Plompen (JRC), Ishikawa (JAEA), Kodeli, and Rugama (NEA).

The objectives of WPEC/SG26 activity are as follows:

A. Compilation of an agreed set target accuracies on relevant design parameters for the Gen-IV concepts. Required target accuracies should be justified in terms of impact on different phases of a specific design (feasibility, pre-conceptual and conceptual design etc.).

B. Definition of a set of data uncertainties and covariance data. These data should be as complete as possible. At this stage, it is not expected to have a "final" set, in particular of covariance data, but an agreed "first iteration" set.

C. Production of a set of quantitative data needs by isotope, reaction type, energy range.

D. Proposal for an approach to meet the needs and relative timeframe.

The present paper summarizes the conclusions of NEA/WPEC/SG26 about the four survey themes above, in order to inform readers of the recent nuclear data needs from innovative reactor design, especially, for sodium-cooled fast reactors.

2. Design Target Accuracy (Objective: A)

To fully define priority issues, besides the nuclear data (isotope, reaction type, energy range) that need improvement, it is essential to quantify target accuracies of reactor core design parameters, and to select a strategy to meet the requirements needed, e.g. by new differential measurements or by the use of integral experiments.

As the first step of the SG26 discussion, the covariance evaluations have been used within a formal procedure to assess the current uncertainty of design parameters induced by nuclear data errors. Next, the target accuracy of design parameters was gathered from the participants of SG26, and the comprehensive agreement was achieved as shown in Table 1, after making the definition of core parameters clear. As well-known, the quantitative values of target accuracy of core parameters strongly depend on the policy of the plant designer with the balancing consideration between economy and reliability, therefore, the target accuracy values in Table 1 should not be taken as the rigorous global standards, but only as rough measures proposed by the SG26 participants, in order to make the discussion move to the next step. An important point found from Table 1 is the SG26 members consider that the current accuracy of some core parameters does not reach the target accuracies, so we need some remedy for that.

Table 1 Current and Targeted Uncertainties for Some SFR Design Parameters (1 sigma)

Parameter	Current Uncertainty (for Sodium-cooled Fast Reactor)		Target Uncertainty assumed by SG26
	Nuclear data origin (a priori)	Analytical modeling origin	
Multiplication factor, keff: Beginning of cycle (dk/k)	1 %	0.5 %	0.3 %
Power peak	1 %	3 %	2%
Burnup reactivity swing (dk/k)	0.7 %	0.5 %	0.3 %
Reactivity coefficients (Sodium void, Doppler): total	7 %	15 %	7 %

3. Covariance Data (Objective: B)

At the starting time of SG26, Sep.2005, JENDL-3.3 was only one general purpose file which equipments the complete covariance data for important nuclides in FBR core.

Therefore, ANL people prepared so-called "educated-guess covariance." This "home made" ANL covariance matrix has been obtained by updating the covariance matrix used in the ADS study by taking into account the results of clean integral experiment analysis. The uncertainty values, have been given by "energy band", consistent with multigroup energy structures used for deterministic calculations both of thermal and fast reactors. Fifteen energy groups have been selected between 20 MeV and thermal energy. At first, only "diagonal" values of the full covariance matrices have been used. Their use implies to neglect all type of correlation (in energy, between different isotopes, among reactions, etc.) and, consequently, to underestimate uncertainties. In a second step, Partial Energy Correlations (PEC) have been introduced. As first guess, the same correlations for all isotopes and reactions, under the form of full energy correlation in 5 energy bands were used.

However, this "home made" ANL covariance matrix was considered to be too rough and insufficient for the SG26 activity by many members. Therefore, preliminary cross-section covariances have been recently developed within the WPEC Subgroup by joint efforts of several laboratories. The new set of uncertainties is called "BOLNA" (standing for BNL, ORNL, LANL, NRG, ANL, from the Labs where the covariances were produced). Energy correlations have been used, but practically no reaction cross-correlations.

BNL has developed cross-section covariances for 45 out of 52 requested materials. The cross-section covariances have been produced in 15- and 187-group representations as follows:

- 36 isotopes (O-16; F-19; Na-23; Al-27; Si-28; Cr-52; Fe-56,57; Ni-58; Zr-90,91,92,94; Er-166,167,168,170; Pb-206,207,208; Bi-209; U-233,234,236; Np-237, Pu-238,240,241,242; Am-241,242m,243; Cm-242,243,244,245) were evaluated using the BNL-LANL methodology, based on the ENDF/B-VII.0 library, the Atlas of Neutron resonances, the nuclear model code EMPIRE and the Bayesian code Kalman;
- 6 isotopes (Gd-155,156,157,158,160 and Th-232) were taken from ENDF/BVII.0;
- 3 isotopes (H-1, U-238 and Pu-239) were taken from JENDL-3.3.

Covariances for the average number of neutrons per fission, total nu-bar, have been provided for 16 actinides identified as priority by the Subgroup.

LANL has evaluated the covariance matrices for U-235, U-238 and Pu-239, in the fast energy region, using only differential measurements and nuclear model calculations. A generalized-least-squares technique is used to evaluate a global covariance matrix based solely on experimental differential information. Since nuclear model calculations are used to complement experimental data, a Kalman filter is then used to combine experimental data and model calculations covariance matrices. This procedure has been used for the three isotopes U-235, U-238, and Pu-239, for the reaction cross-sections of (n,fission), (n,capture), (n,total), (n,elastic), (n,inelastic), and (n,xn). The covariance matrices related to the average number of neutrons have been obtained from experimental data only.

To complete these data, at ORNL resonance-parameter covariance evaluations have been performed for U-235, U-238, and Pu-239 with the computer code SAMMY. For U-235 the covariance evaluations have been done in the resolved and unresolved energy regions whereas for U-238 and Pu-239 only the resolved resonance covariance evaluations have been done. Experimental uncertainties are incorporated directly into the evaluation process in order to propagate them into the resonance parameter results.

Finally, covariance data files for Pb isotopes have been produced at NRG by a purely stochastic approach. This is accomplished by subjecting the nuclear model code TALYS to a Monte Carlo scheme for perturbing the input parameters of the various nuclear models, such as level densities, gamma-ray strength functions and the optical model.

The future improvement of BOLNA covariance was assessed as below:
a) Improvement of the present covariance data, and consolidation of the very low values presently assessed for the major actinides. This is needed for the further phase of "data adjustments".
b) Covariance data assessment for the major fission product, for some selected structural materials, for fission spectra.
c) Introduction of cross correlations among nuclides and reactions.
d) Investigation of potential effects of mu-bar uncertainty.

4. Quantitative Data Needs by Isotope, Reaction Type, Energy Range (Objective: C)

To establish priorities and target accuracies on data uncertainty reduction, G.Aliberti of ANL adopted a formal approach by defining target accuracies on design parameters and finding out the required accuracy on cross-section data. The unknown uncertainty data requirements d_i can be obtained by solving the following minimization problem:

$$\sum_i \lambda_i / d_i^2 = \min \qquad i = 1 \ldots I$$

(I is the total number of parameters) with the following constraints:

$$\sum_i S_{ni}^2 d_i^2 < \left(R_n^T\right)^2 \qquad n = 1 \ldots N$$

(N is the total number of integral design parameters) where S_{ni} are the sensitivity coefficients for the integral parameter R_n, and R_n^T are the target accuracies on the N integral parameters.

λ_i are "cost" parameters related to each σ_i and should give a relative figure of merit of the difficulty of improving that parameter (e.g., reducing uncertainties with an appropriate experiment). The important

assumption of this ANL approach is that only the diagonal values of the BOLNA covariance matrix have been the object of the present target accuracy study.

Further, the following three assumptions are adopted. Part results of nuclear data needs are demonstrated in Table 2.

1) Simultaneous target accuracy over the ensemble of reactors.
2) $\lambda = 1$.
3) To avoid the introduction of meaningless parameters, we have chosen as unknown "d" parameters only those cross-sections which globally account at least for 98% of the overall uncertainty on each integral parameter that does not meet the accuracy requirements.

Table 2 Uncertainty Reduction Requirements Needed to Meet Integral Parameter Target Accuracies (a part) (for Advanced Burner Test Reactor (ABTR), Sodium-cooled Fast Reactor (SFR), and European Fast Reactor (EFR))

Isotope	Reaction	Energy range	Uncertainty (1sigma)	
			Current	Required
U-238	Capture	24.8-9.12 keV	9.4 %	3.8 %
	Inelastic	2.23-1.35 MeV	20.6 %	4.5 %
Pu-239	Capture	67.4-24.2 keV	10.1 %	6.3 %
Pu-240	Fission	1.35-0.498 MeV	5.8 %	1.8 %
Pu-241	Fission	183-67.4 keV	19.9 %	2.6 %
O-16	Capture	6.07-2.23 MeV	100.0 %	39.5 %
Na-23	Inelastic	1.35-0.498 MeV	28.0 %	4.0 %
Fe-56	Inelastic	1.35-0.498 MeV	16.1 %	3.2 %

5. Approach to Meet the Needs (Objective: D)

From the conclusion of Objective: C, it seems very difficult to reach the design target accuracy by improving only differential nuclear data in near future. The Chair of SG26, M.Salvatores, finally proposed the approach to meet the design targets as below:

The statistical adjustment method can provide a powerful and robust tool to improve uncertainties in key design parameters. The method makes use of:
a) "A priori" nuclear data covariance information,
b) Integral experiments analysis to define C/E values
c) Integral experiment uncertainties
in order to:
- Evaluate „a priori" uncertainties on reference design performance parameters,
- Reduce these uncertainties using integral experiments („a posteriori" uncertainties on performance parameters)
- Define "adjusted" nuclear data and associated „a posteriori" covariances

Then, it is needed:
1) Selection of a set of relevant experiments (more on that later),
2) Sensitivity analysis of selected configurations including reference design configurations for a wide range of integral parameters related to the core performances (critical mass, reactivity coefficients, control rod worth, power distributions etc.), and fuel cycle parameters (reactivity loss/cycle, decay heat, transmutation rates, neutron sources and doses of spent fuel etc),
3) Use of science based covariance data for uncertainty evaluation and target accuracy assessment,
4) Analysis of experiments using the best methods available, with some redundancy to avoid systematic errors,
5) Use of calculation/experiment discrepancies (and associated uncertainties) in a statistical adjustment.

Here, we have to seriously recognize that the credibility of an adjustment is dependent on the credibility of the experimental uncertainties.

6. Next Steps and Concluding Remarks

As the continuation of the SG26 activity, it is proposed to WPEC to consider the setting-up of two new subgroups:

- A new specific subgroup on "Methods and issues for the combined use of integral experiments and covariance data". Participation of evaluators (to account for feedbacks to files) and a close link to related activities like the ones coordinated at the Uncertainty Analysis of Criticality Safety Assessment expert group (UACSA) should be clearly established.
- A new subgroup that should organize the work needed to meet the requirements for microscopic nuclear data as they have been pointed out, that is, share of work on different installations and different projects, evaluation etc. However, this proposal of nuclear data experimental expert group is now under discussion since the mission seems to be duplicated that of the existing Subgroup-C, the High Priority Request List.

As a summary of the present report, the author makes short comments for the four themes treated in the NEA/SG26 activity as below:

A) Design Target Accuracy: the agreed table seems suitable as rough reference values for designers,
B) Covariance Data: though there was lots of discussion on the approach, it seems to have taken the right methodology finally,
C) Quantitative data needs by isotope, reaction and energy: it seems to be resulted only to demonstrate the needs of integral information, and,
D) Approach to meet the needs: it seems to take the same direction with that of Japan.

References

1. Gen-IV Homepage: http://nuclear.energy.gov/genIV/neGenIV1.html (Oct. 2007)
2. GNEP Homepage: http://www.gnep.energy.gov/gnepProgram.html (Oct. 2007)
3. H.Niwa, et al.: "Current Status and Perspective of Advanced Loop Type Fast Reactor in Fast Reactor Cycle Technology Development Project," Proceedings of International meeting on Advanced Nuclear Fuel Cycles and Systems (GLOBAL 2007), Boise, Idaho, USA (Sep. 2007)
4. NEA/WPEC/SG26 Homepage: http://www.nea.fr/html/science/wpec/meeting2007/SG26/ (Nov. 2007)

2.7 Status of LWR fuel design and future usage of JENDL

Takuya ITO

Fuel Engineering and Development Department, Tokai Works, Nuclear Fuel Industries, Ltd.

3135-41, Muramatsu, Tokai-mura, Naka-gun, Ibaraki-ken, 319-1196

e-mail: t-itoh@nfi.co.jp

For all conventional LWR fuel design codes of LWR fuel manufactures in Japan, the cross section library are based on the ENDF/B. Recently we can see several movements for the utilization of JENDL library for the LWR fuel design. The latest version of NEUPHYS cross section library is based on the JENDL-3.2. To accelerate this movement of JENDL utilization in LWR fuel design, it is necessary to prepare a high quality JENDL document, systematic validation of JENDL and to appeal them abroad effectively.

1. Introduction

One of the most important activities in the development of the nuclear power system is improvement of the nuclear data. Japanese serious activity has contributed to the many fields of the evaluation in the world ever. Japanese nuclear data activity is admitted as the one of the highest level in the world. At a glance of the latest evaluated nuclear data file ENDF/B-VII[1], considerably much contribution from Japan is found in the evaluations. On the other hand, one of the fruits of Japanese nuclear data activity is the Japanese Evaluated Nuclear Data Library, JENDL. Status of nuclear data library from the view point of usage of JENDL was reported by Hirano, 2006[2]. For all conventional LWR fuel design code of LWR fuel manufactures in Japan, the cross section library are based on the ENDF/B-IV / V/ VI. Recently several movements for the utilization of JENDL library for the LWR fuel design. It is important to appeal abroad for worldwide its usage.

2. New movement of JENDL utilization in LWR fuel design

The cross section library of the latest version of NEUPHYS[3] is generated from the JENDL-3.2[4]. The validation of NEUPHYS was performed from various viewpoints. For example, Figure 1 shows the comparison of fission rate distribution between NEUPHYS calculation results and the measurement data at the NBN-VENUS critical experiment[5]. Addition to NBN-VENUS experiment, the BASALA critical[6] experiments and a MOX loaded commercial reactor analysis[7] had been reported for the NEUPHYS validation. From various view points, as criticality, fission rate

Figure 1

distribution, void reactivity, poison reactivity in the critical experiments and three dimensional power distribution in the commercial reactor, nuclear data processed from JENDL-3.2 show excellent performance in combination with NEUPHYS code. From now on additional new validations of JENDL-3.2 and NEUPHYS will be reported, these activity shall be linked to application of JENDL-3.2 and NEUPHYS to LWR fuel design.
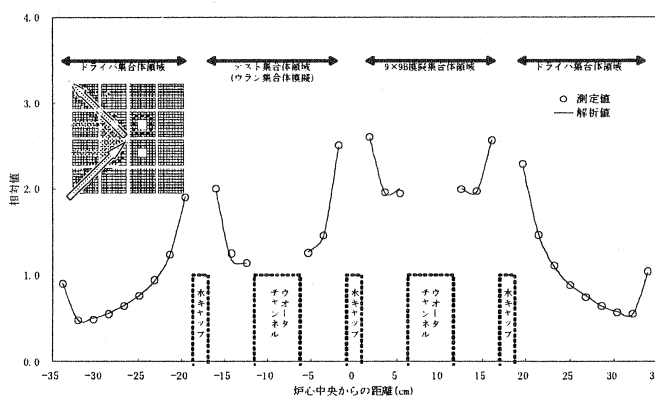
3. Future usage of JENDL

We can see the movement of the JENDL utilization in the field of LWR fuel design in Japan. It is important to enlarge this wave for keeping Japanese nuclear data evaluation activity in high level. In the other countries also, nuclear data evaluation work is located in the highest priority work, and evident productions are generated as ENDF/B-VII.0. It is necessary to appeal abroad for worldwide JENDL usage through an effective documentation, a systematic preparation of benchmarking of JENDL and cooperation with international organizations. Followings are remarks for three key points for JENDL future usage in the world wide.

- **Documentation**: ENDF/B-VII.0 paper[1] is an example of the best documentations. In the paper, much information is included and is organized very well. For example, the history of ENDF/B, the organization for development ENDF/B-VII, description for the all 14 sub libraries, methodology of evaluations, specific descriptions for major nuclides and massive validation of evaluated data. In addition, a paper on the Benchmarking of ENDF/B-VII[8] was issued at the same time of above mentioned paper.

- **Benchmarking**: Benchmarking systematic and covering various user needs is important. For example, for criticality ICSBEP is the basic validation of nuclear data library. It is desirable that results of such benchmark calculations should be published at the same time of a release of JENDL new version.

- **Appeal**: It is important to improve performance of JENDL library itself, but to appeal to foreign users is more important to prevail among LWR fuel design field soon. Because, historically, in LWR and LWR fuel developments, the international technical cooperation had played major roles.

4. Conclusion

For all conventional LWR fuel design codes of LWR fuel manufactures in Japan, the cross section library are based on the ENDF/B. Recently we can see several movements for the utilization of JENDL library for the LWR fuel design. NEUPHYS cross section library is based on the JENDL-3.2. A combination of JENDL-3.2 and NEUPHYS is validated from various angle for the purpose of LWR fuel design and reported excellent results. To accelerate this movement of JENDL utilization in LWR fuel design, it is necessary to prepare a high quality JENDL document, systematic validation of JENDL and to appeal them abroad effectively.

References

[1]　M. B. Chadwick, et. al., "ENDF/B-VII.0: Next Generation Evaluated Nuclear Data Library for Nuclear Science and Technology", *Nuclear Data Sheets*, **107**, 2931-3060 (2006)

[2]　G. Hirano, S. Kosaka, "Nuclear data library in design calculation," *Proc. the 2005 Sympo. Nucl. Data*, Tokai, Japan, Feb. 2-3 (2006)

[3]　T. Ito, *et. al.*, "Applicability of NEUPHYS/COS3D to MOX Loaded BWR Core Design (1)," *Proc. 2007 Fall Mtg. AESJ*, Sept. 27-29, M21, Japan, (2007) [in Japanese] [CD-ROM]

[4]　T. Nakagawa, *et. al.*, "Japanese Evaluated Nuclear Data Library Version 3 Revision-2: JENDL-3.2," *J. Nucle. Sci. Technol.*, **32**[12], 1259-1271 (1995)

[5]　Y. Kanayama, *et. al.*, "Applicability of NEUPHYS/COS3D to MOX Loaded BWR Core Design (2)," *Proc. 2007 Fall Mtg. AESJ*, Sept. 27-29, M21-M23, Japan, (2007) [in Japanese] [CD-ROM]

[6]　K. Ishii, et al, "Analysis of High Moderation Full MOX BWR Core Physics Experiments BASALA," *Trans. At. Energy Soc. Japan*, **4**, No.1, 45-65 (2005) [in Japanese]

[7]　M. Tokashiki, *et. al.*, "Applicability of NEUPHYS/COS3D to MOX Loaded BWR Core Design (3)," *Proc. 2007 Fall Mtg. AESJ*, Sept. 27-29, M21-M23, Japan, (2007) [in Japanese] [CD-ROM]

[8]　Steven C. van der Marck, "Benchmarking ENDF/B-VII.0", *Nuclear Data Sheets*, **107**, 3061-3118 (2006)

3. Papers Presented at Poster Sessions

This is a blank page.

3.1 Motivation for the determination of the ^{244}Cm effective neutron capture cross-section

Shoji NAKAMURA, Yuichi Hatsukawa, Hideo HARADA

Japan Atomic Energy Agency

2-4 Shirakata-Shirane, Tokai-mura, Naka-gun, Ibaraki, 319-1195, Japan

E-mail: shoji.nakamura@jaea.go.jp

Measurement of the effective neutron capture cross-section of ^{244}Cm was tried, and the irradiation test of the ^{244}Cm sample was performed for 1 cycle. Gamma- and alpha-rays measurements were performed to analyze the productions from the ^{244}Cm(n,γ) and fission reactions.

1. Introduction

The social acceptability of nuclear power reactors is related to the waste management of long-lived fission products (LLFP) and minor actinides (MAs) existing in spent nuclear fuels. The MAs (^{241,243}Am, ^{244,245}Cm, *etc.*) are important in the nuclear waste management, because the presence of these nuclides induces long-term radiotoxicity because of their relatively long half-lives. **Figure 1** illustrates the section of the chart of the nuclides displaying the relevant reactions and decays of Am and Cm isotopes. The Am isotopes generate the higher actinides as the Cm isotopes through neutron capture reactions. Moreover, the Cm isotopes also generate the higher actinides. The partitioning and transmutation of MAs have some merits in the reprocessing of spent nuclear fuels.[1] When considering transmutation, the accurate data of neutron capture cross-sections are necessary. In this view point, the cross-section measurements have been made by the activation method. The ^{243}Am effective cross-section was measured in the past.[2] It was found that the obtained result would affect the ^{244}Cm production by about 10% in comparison with that predicted by the evaluated data. Therefore, our concern was focused to measure the cross-section for ^{244}Cm to discuss the production of higher Cm isotopes.
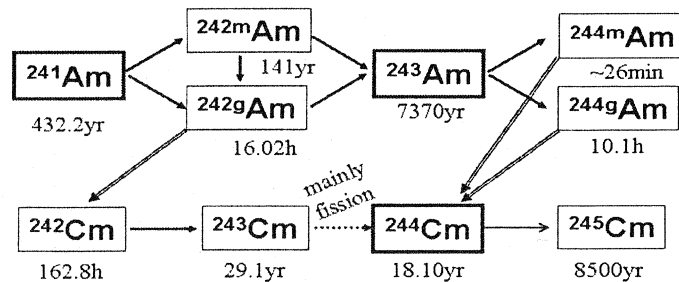

Fig. 1   Schematic view of the reaction chain of Am and Cm isotopes.

Figure 2 plots the measured and evaluated data for the thermal-neutron capture cross-section and the resonance integrals of ^{244}Cm. As seen in Fig.2, there are only a few of data. It seems that the value of the thermal neutron capture cross-section by Gavrillov[3] would be adapted as the evaluated data[4]. This situation would show the necessity of re-measurement of the ^{244}Cm cross-section.
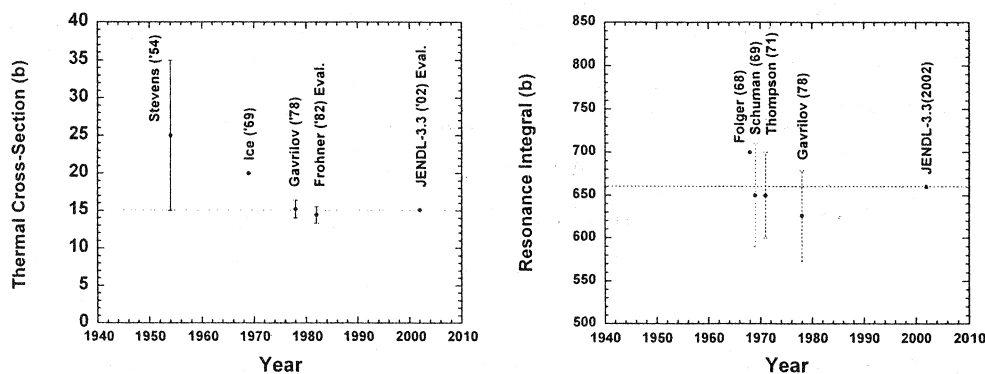
Fig.2   Measured and evaluated data for the thermal-neutron capture cross-section
and the resonance integral of ^{244}Cm

2. Experiments

A ^{244}Cm standardized solution (Amersham International plc., 1 mol/L(M) HNO_3) was prepared as Cm samples.   The Cm solution contained 239+240Pu of 0.19 % as one of impurities.   The ^{244}Cm standardized solutions equivalent to 5μCi, was dropped into the bottom of high-purity quartz tubes (8 mm in inner diameter, 50 mm in length).   After drying of solutions, quartz tubes were flame-sealed under evacuation.

Wires of Co/Al alloy (Co: 0.46±0.1 wt%, 0.381 mm in diameter), Au/Al alloy (Au: 0.112±0.01 wt%, 0.510 mm in diameter) and Mo (Mo: 99.945%, 0.5mm in diameter) were used to monitor neutron fluxes at the irradiation position.   Two set of Co, Au and Mo wires were rapped with a high purity aluminum foil.

The irradiation was performed for 1 cycle (555 hours) in the HR-2 of the JRR-3M, of which thermal-neutron flux as the nominal value was $1.0 \times 10^{14} n/cm^2 s$ at 20-MW operating.   Each set of Co, Au and Mo wires were irradiated for 1 hour at the same position before and after the 1 cycle irradiation.

After 70 days fro the end of the irradiation, the Cm sample was dissolved by adding 100 μl of 6M HCl solution.   About 20 μl was extracted from the solvent solution, and was dropped onto the center of a Pt dish (20mmφ in diameter, 0.5mm in thickness).   After dryness, measurement samples were prepared.
Alpha rays emitted from ^{244}Cm (5.805 and 5.763 MeV[5]) and ^{245}Cm (5.362 and 5.304 MeV[5]) were measured with a silicon surface-barrier alpha-spectrometer as shown in **Figure 3**.

Figure 4shows typical α-ray spectra obtained with the Am check source and ^{244}Cm sample.   The measured system resolution for the α-ray peaks of ^{241}Am and ^{242}Cm was 18 keV.   The position of alpha -ray peak from ^{245}Cm which we aim at was around 2200ch in Fig.4.   Since sufficient resolution was obtained, it was expected that alpha rays from ^{245}Cm would be measured when the Cm sample could be processed like the test sample.

The γ rays from irradiated monitor wires were measured by a high-purity Ge-detector, of which performance was characterized by a relative efficiency of 25 % to a 7.6 cm×7.6 cmφ NaI (Tl) detector and an energy resolution of 2.0 keV full width at half-maximum (FWHM) at the 1.33 MeV peak of ^{60}Co. The peak detection efficiencies were determined with ^{152}Eu and ^{60}Co sources.   The error of the detection efficiency due to the uncertainties of the calibration γ source intensities was estimated as 1.5%.

Radioactivities of Au, Co and Mo monitor wires were measured at a distance of 100.-mm from the center of the detector head.
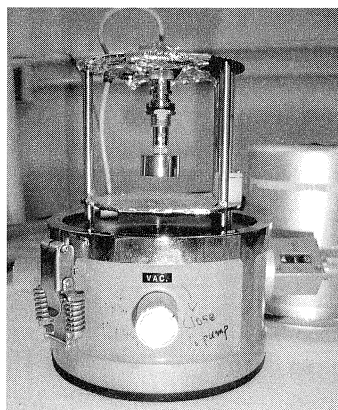

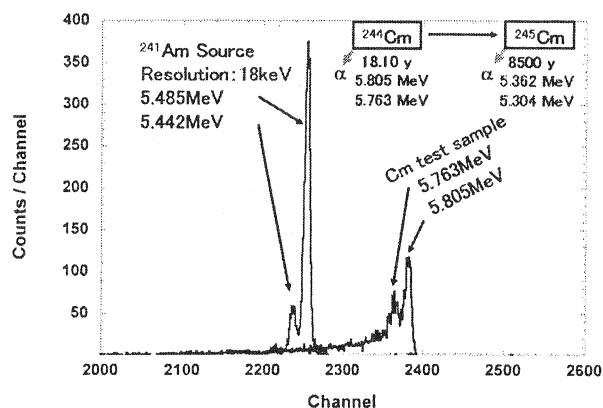Fig.3 a silicon surface-barrier alpha-spectrometer

Fig.4 typical α-ray spectra obtained with an [244]Am check source and [244]Cm sample

3. Analysis

The effective cross-section $\hat{\sigma}$ is defined by equating the reaction rate R to product of $\hat{\sigma}$ and $n\upsilon_0$, where $n\upsilon_0$ is the "neutron flux" in Westcott's convention[6] with the neutron density n, including thermal and epithermal neutrons, and with the velocity of neutron $\upsilon_0 = 2,200$ m/s, so that

$$R = n\upsilon_0\hat{\sigma} .\tag{1}$$

When the cross-section departs from the $1/\upsilon$ law, a simple relation for $\hat{\sigma}$ can be obtained as:

$$\hat{\sigma} = \sigma_0\left(gG_{th} + r(T/T_0)^{1/2}s_0G_{epi}\right),\tag{2}$$

where σ_0 is the thermal-neutron capture cross-section; g is a function of the temperature related to departure of the cross-section from the $1/\upsilon$ law; r is an epithermal index in Westcott's convention.; T is neutron temperature and T_0 is 293.6 K; the quantity $r(T/T_0)^{1/2}$ gives the fraction of epithermal neutron in the neutron spectrum; the G_{th} and G_{epi} denote self-shielding coefficients for thermal and epithermal neutrons, and are taken as unity in this analysis under the present sample conditions. The parameter s_0 is defined by:

$$s_0 = \frac{2I_0'}{\sqrt{\pi}\sigma_0},\tag{3}$$

where I_0' is the reduced resonance integral, i.e. the resonance integral with the $1/\upsilon$-component subtracted.

Substituting Eq.(3) into Eq.(1), reaction rates can be written in the simplified forms as:

$$R\big/\sigma_0 = gG_{th}\phi_1 + G_{epi}\phi_2 s_0 .\tag{4}$$

Here the ϕ_1 and ϕ_1' are neutron fluxes in the low (thermal) energy region. The values of ϕ_1 and ϕ_2 at the irradiation position were obtained by using the data of s_0 and σ_0, and reaction rates R for the monitor wires. The reaction rates were calculated from peak counts of γ rays from ^{60}Co, [198]Au and [99]Mo. **Figure 5** shows the experimental relation between R/σ_0 and s_0 obtained by the flux monitor wires. The thermal-neutron

flux at the irradiation position was 7.9×10^{13} n/cm^2/s. The slope of the solid line gives the epithermal flux component, i.e. ϕ_2. Westcott's index [6] was only 0.5%, it means that the neutron flux was well-moderated.
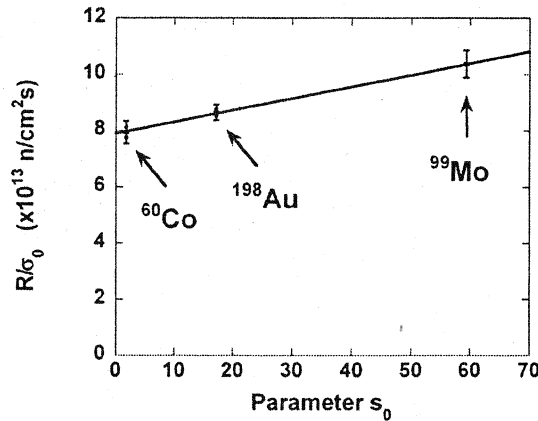

Fig.5 Experimental relation between R/σ_0 and s_0
obtained by the flux monitors.

4. Results and discussions

Gamma-ray measurement of the irradiated ^{244}Cm sample was performed for 6 days after 70 days from the end of the irradiation. As fission products of 244Cm, the nuclides whose half-lives were tens of days or more were observed such as ^{95}Zr, ^{103}Ru, ^{124}Sb, ^{131}I, ^{134}Cs, ^{137}Cs, ^{140}Ba and so on. The γ-ray yield from each nuclide gives the production rate per ^{244}Cm nucleus. The production rate was obtained as shown in **Figure 6**. The result shows that the rates are two mountains of around 100ch and 150ch.
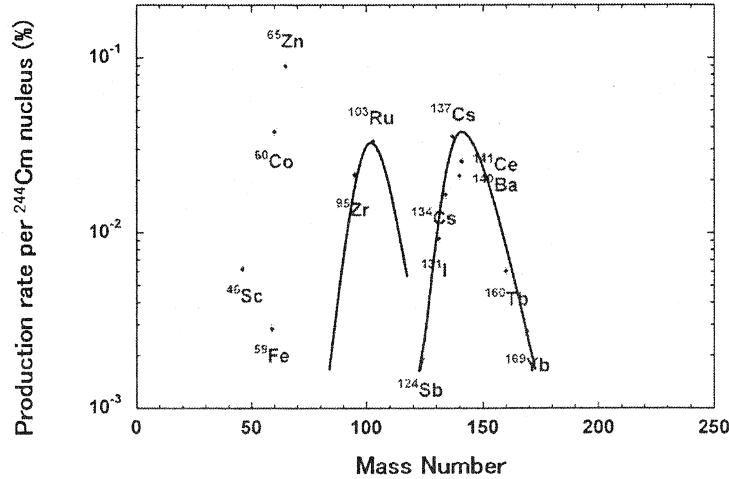

Fig.6 the production rate per ^{244}Cm nucleus

More information would be obtained about the fission products from ^{244}Cm, if the nuclides with short half-lives were measured quickly after the irradiation.

The alpha-ray measurements were performed for the Cm sample. The distance was 14mm between the surface of the sample disk and the silicon detector. An example of an alpha-ray spectrum is shown in **Figure 7**. The spectrum has a large tail in the low energy region, therefore weak alpha-rays from ^{245}Cm were not observed. When the Cm sample was dried, the lump of the sample would be made. It is necessary to reprocess the surface of the Cm sample.
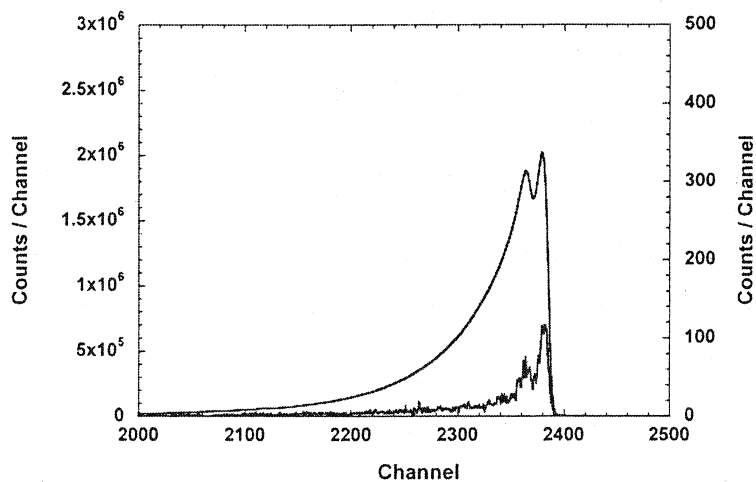
Fig.7 An example of alpha-ray spectrum of the irradiated ^{244}Cm sample (15hours)

4. Conclusion

Measurement of the effective neutron capture cross-section of ^{244}Cm was tried, and the ^{244}Cm sample was irradiated for 1 cycle (555 hours) at HR-2 of JRR-3M. It found that the neutron flux at the irradiation position was well-moderated. Gamma- and alpha-rays measurements were performed to analyze the productions from the ^{244}Cm(n,γ) and fission reactions. The fission products of 244Cm were measured, the production rates were obtained. The alpha-ray measurements of the irradiated Cm sample showed that the problem was still in the sample preparation. It is necessary to readjust processing on the surface of the Cm sample.

The measurement of the isotope ratio (^{245}Cm/^{244}Cm) will be planed by a mass spectrometer.

Acknowledgement

The authors would like to thank the staff of the JRR-3M for their cooperation.

References

[1] H.Takano, T.Ikegami, *Seventh Information Exchange Meeting*, Jeju, Republic of Korea, Oct.14-16, 2002, pp.23-35.

[2] M. Ohta *et al.*, *J.Nucl.Sci.Technol*, **43**, p.1441 (2006).

[3] V. D. Gavrilov, V. A. Goncharov and V. P. Smirnov: *Soviet Atomic Energy*, **41**(3), 808 (1976).

[4] S. F. Mughabghab, M. Divadeenam, N. E. Holden, "*Neutron Cross Section*", vol. **1**and **2**, Academic Press, New York, (1981).

[5] R. B. Firestone, V. S. Shirley, C. M. Baglin, S. Y. F. Chu, and J. Zipkin, Table of Isotopes, 8th edition, John Wiley and Sons, New York, (1995).

[6] C. H. Westcott, W. H. Walker, T. K. Alexander, "*Proc. 2nd Int. Conf. Peaceful Use of Atomic Energy, Geneva*", United Nations, New York, **16**, 70 (1958).

3.2 Measurement of activation cross section of (n, p) and (n, α) reactions in the energy range of 3.5 to 5.9 MeV using a deuterium gas target

Masataka FURUTA [1], Itaru MIYAZAKI [1],

Hiroshi YAMAMOTO [1], Michihiro SHIBATA [2], Kiyoshi KAWADE [1]

[1] *Graduate School of Engineering, Nagoya University*

[2] *Radioisotope Research Center, Nagoya University*

e-mail: furuta.masataka@f.mbox.nagoya-u.ac.jp

Activation cross sections of (n, p) and (n, α) reactions were measured by means of the activation method in the neutron energy range between 3.5 and 5.9 MeV. The d-D neutrons were generated by the deuterium gas target at the Van de Graaff accelerator (KN-3750) at Nagoya University. For the corrections of the neutron irradiations, the neutron spectra and mean neutron energies at the irradiation positions were evaluated with the MCNP-4C2 Monte Carlo code. The cross section values of ^{27}Al, $^{28, 29}$Si, ^{41}K, ^{51}V, ^{61}Ni, ^{65}Cu, $^{64, 67}$Zn, ^{69}Ga, ^{79}Br, ^{92}Mo and ^{93}Nb were obtained. These of four (n, p) reactions for the ^{29}Si, ^{67}Zn, ^{69}Ga and ^{79}Br, and ^{69}Ga (n, α) reaction were obtained for the first time. The evaluated data libraries on the basis of the theoretical calculations agree with the present results within 40%. The systematics of the (n, p) reactions in the neutron energy of 5.0 MeV in the mass range between 27 and 92 were proposed for the first time on the basis of this experiment. This can predict the cross sections within an accuracy of a factor of 1.6.

1. Introduction

A database of activation cross sections for neutron energy up to 20 MeV is required for neutron dosimetry, the design of D-T fusion reactors and neutron shielding in an accelerator facility. A lot of experimental cross section data have been reported in the neutron energy of around 14 MeV. On the other hand, there are insufficient data around 5.0 MeV because there are few appropriate neutron sources for the measurement of cross sections. In this work, we have measured activation cross section around 5.0 MeV and proposed the systematics on the basis of the present results.

2. Experiment

The d-D neutrons were generated by the deuterium gas target at the KN-3750 at Nagoya University. The accelerating voltage was between 1.0 and 3.5 MV. A pneumatic sample transport system was used for the irradiation, as shown in Fig.1-(a), (b) [1]. Typical neutron flux at the

irradiation position was approximately 2×10^6 n/cm^2/s. The fluctuation of the neutron flux was monitored by Multi-Channel Scaling (MCS) method using a NE213 liquid scintillation detector set in the irradiation room. The dwell time of MCS was 10 s.

The deuterium gas target consisted of a small cell (length of 29 mm, diameter of 8 mm and thickness of 1 mm) made of aluminum and filled with D$_2$ at 1.6×10^5 Pa, as shown in Fig.2. The cell was separated from the vacuum of the accelerator by a 2.2-μm-thick Havar foil, which acts as a window. This foil is pasted on a 1-mm-thick aluminum ring with a 5-mm-diameter hole in it. The incident d$^+$-beam from the accelerator generate neutrons via the D (d, n) ^{3}He reaction in the cell and finally lose its remaining energy in the end of the cell that is air-cooled. The Havar foil window can endure beam currents of up to 3 μA. For routine use, beam currents of <1 μA are employed. The distance between the surface of the gas target and the irradiation position was 20 mm, and the angle with respect to the incident d$^+$-beam was 0°.

The target materials were enriched isotopes or one of the naturally abundant materials. The samples in the foil form were rectangular-shaped 10 mm × 10 mm and 0.1-0.5 mm in thickness. The samples in powder form were wrapped with a thin cartridge paper, with a typical thickness of 1-2 mm. The samples were 50-90 mg. The chemical form, isotopic abundance, weight and thickness of the samples are listed in Table 1. The γ-rays emitted from the induced activities were measured with a well-type HPGe detector [2]. All cross section values were determined relative to those of the ^{115}In (n, n') ^{115m}In reactions.

3. Correction of background components

The calculated neutron spectra are shown in Fig.3 for the incident deuteron energy of 3.0 MeV using the MCNP-4C2 Monte Carlo code [3]. The neutron spectrum has a broad peak with two low-energy components. One was the self-loading of the incident d$^+$-beams in the target cell end and the other was the scattering neutrons by surrounding materials. The calculated neutron spectrum was separated into the main peak and low-energy components to subtract the contributions of low-energy components from the induced activities. The magnitude of the correction for low-energy neutrons is listed in Table 2.

4. Results

The cross sections of twelve (n, p) reactions and two (n, α) reactions were measured. Four (n, p) reactions for the ^{29}Si, ^{67}Zn, ^{69}Ga and ^{79}Br, and ^{69}Ga (n, α) reaction were measured for the first time in the neutron energy range between 3.5 and 5.9 MeV. The evaluated data libraries agree with the present results within 40% or less, as shown in Fig.4.

5. Systematics

By using only our data, we studied the systematic of the (n, p) reactions in the energy of 5.0

MeV. Our data were this experiment and the previous data measured by using the FNS in JAEA in the mass region of less than 92 [4]. As shown in Fig.5, the value of $\sigma_{n,p}/(A^{1/3} + 1)^2$ were plotted as a function of $(E_{th} + V_p)$, where $\sigma_{n,p}$, A, E_{th} and V_p are the cross section of the (n, p) reaction in the neutron energy of 5.0 MeV, the mass number, the threshold energy of the (n, p) reaction and the Coulomb barrier for an outgoing proton and a residual nucleus, respectively. The solid and dotted lines were obtained by fitting the data for the even-odd or odd-even nuclei and the even-even ones, respectively. The fitted curves were expressed as

$$\sigma_{n,p} = 5.59 \times 10^3 \left(A^{1/3} + 1 \right)^2 \exp\left\{-1.30\left(E_{th} + V_p\right)\right\}, \qquad \text{(even-odd, odd-even)}$$

$$\sigma_{n,p} = 1.38 \times 10^7 \left(A^{1/3} + 1 \right)^2 \exp\left\{-1.93\left(E_{th} + V_p\right)\right\}, \qquad \text{(even-even)}$$

The coefficients were determined on the basis of systematics of the (n, np) reaction in the neutron energy of 14 MeV [5,6]. It can be seen that the deviation from the fitted line falls between 0.6 and 1.6, namely within a factor of 1.6, in the neutron energy of 5.0 MeV in the mass range between 27 and 92.

6. Conclusion

We measured the cross section data of twelve (n, p) reactions and two (n, α) reactions in the neutron energy range of 3.5 to 5.9 MeV by using the KN-3750 at Nagoya University. The systematics of the (n, p) reaction in the neutron energy of 5.0 MeV were proposed for the first time, which can predict cross sections of the (n, p) reaction within an accuracy of a factor of 1.6 in the mass range between 27 and 92.

Acknowledgement

References

[1] T. Shimizu, et al., Nucl. Instr. Methods, A527, 543 (2004).

[2] K. Kawade, et al., Nucl. Instr. Methods A496, 183 (2003).

[3] J. F. Briesmeister, Ed, "MCNP-4 General Monte Carlo N-Particle Transport Code, Version 4C" LA-13709-M (2000).

[4] T. Shimizu, et al., Ann. Nucl. Energy 31, 975 (2004).

[5] H. Sakane, et al., JAERI-Conf. 2000-005, 202 (2000).

[6] H. Sakane, et al., Symp. on Isot. Eff. in Phys. Chem. and Eng. Nagoya, Aug. 22-24 Extend abstracts, 55 (2001).
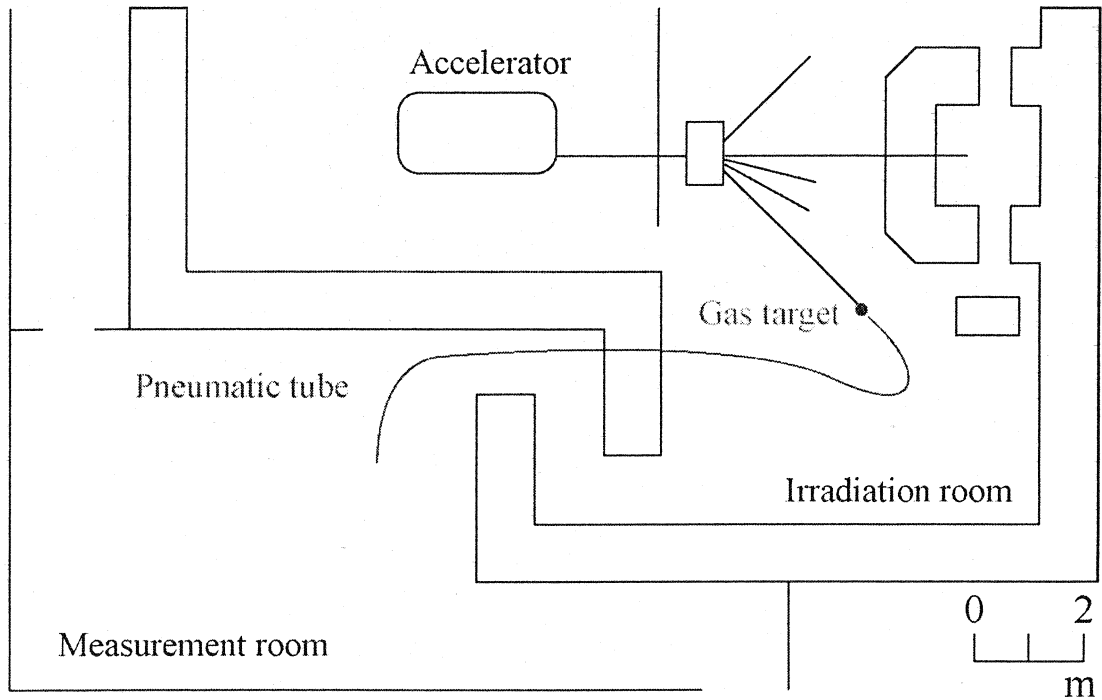
Fig.1-(a). A plane view of KN-3750 at Nagoya University.
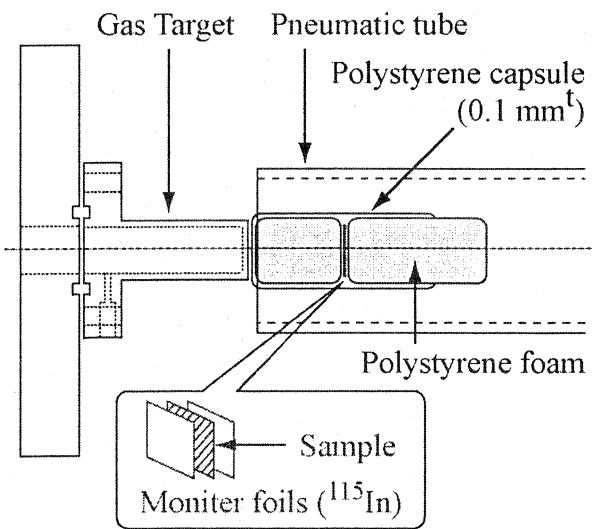The blue line shows a pneumatic sample transport system.

Fig.1-(b). An expanded view around
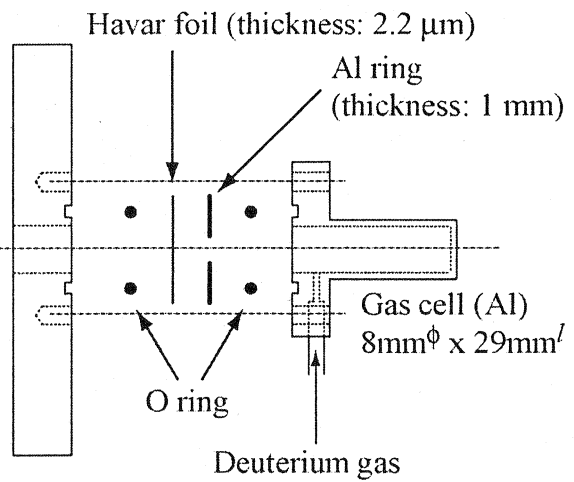the gas target assembly.

Fig.2. Cross sectional view of
the gas target assembly.

Table 1. Properties of samples

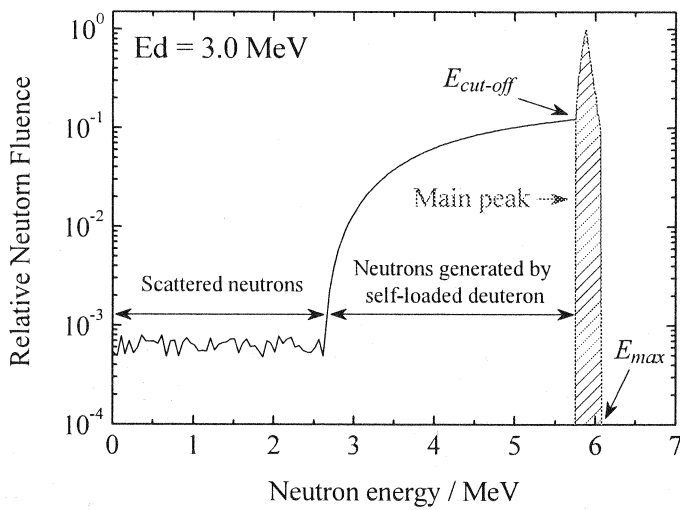| Target nuclei		Chemical form	Abundance / %	Weight / mg	Thickness / mm
^{27}Al	(Natural)	Al	100	54	0.2
^{28}Si	(Natural)	SiO_2	92.23	65	0.85
^{29}Si	(S.I.)	SiO_2	95.65	64	2.00
^{41}K	(Natural)	$KHCO_3$	6.7302	92	1.50
^{51}V	(Natural)	V_2O_5	99.750	80	1.30
^{61}Ni	(S.I.)	Ni	88.84	23	1.00
^{64}Zn	(Natural)	Zn	48.6	350	0.5
^{67}Zn	(S.I.)	ZnO	94.60	61	1.20
^{69}Ga	(Natural)	Ga_2O_3	60.108	80	1.20
^{79}Br	(Natural)	KBr	50.69	82	1.70
^{92}Mo	(S.I.)	Mo	97.01	72	1.15
^{93}Nb	(Natural)	Nb	100	90	0.1
^{115}In	(Natural)	In	95.71	150	0.2

Fig.3. Spectrum of emitted neutron from the gas target at an irradiation position of 0° calculated by MCNP-4C2 Monte Carlo code. $E_{cut-off}$ is neutron cut-off energy separating into scattered low-energy and main peak components; E_{max} is maximum energy in the emitted neutrons.

Table 2. Magnitude of the correction of Background components

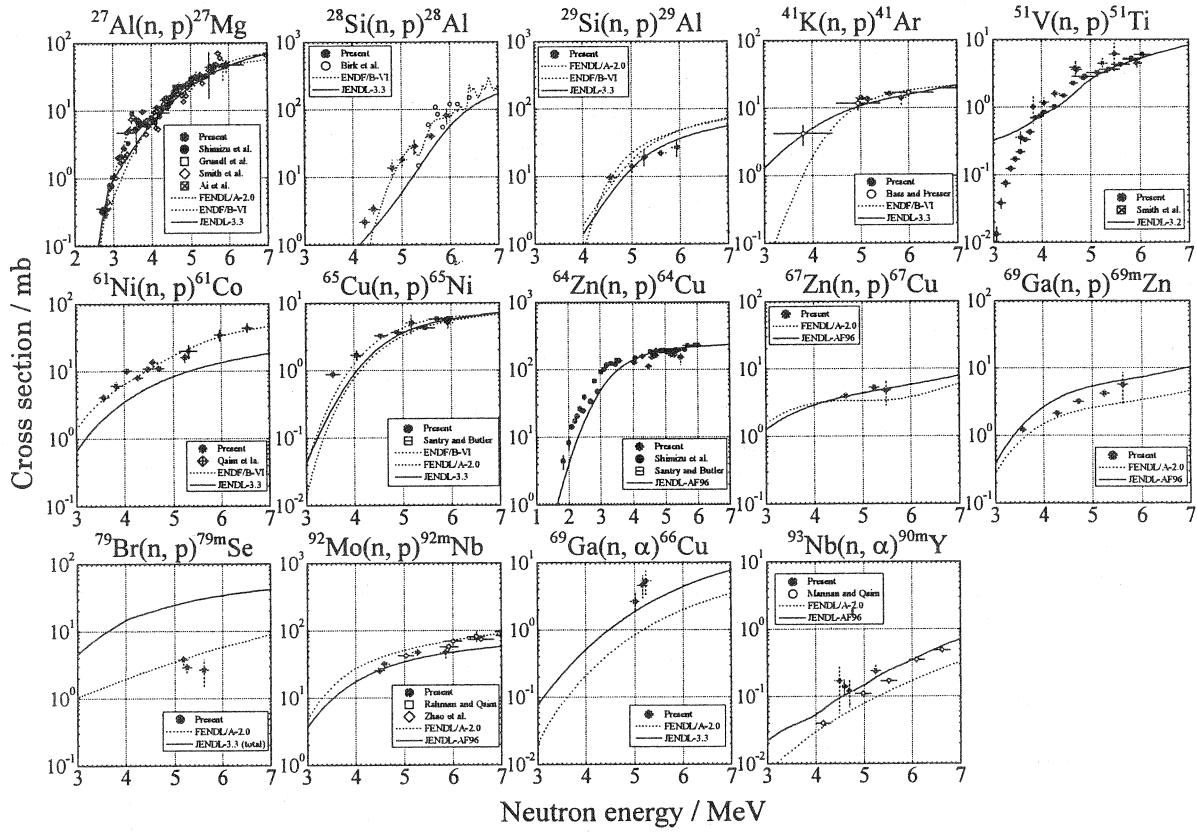| Reaction	Background components / %
^{27}Al (n, p) ^{27}Mg	11-71
^{28}Si (n, p) ^{28}Al	28-83
^{29}Si (n, p) ^{29}Al	24-52
^{41}K (n, p) ^{41}Ar	12-42
^{51}V (n, p) ^{51}Ti	23-75
^{61}Ni (n, p) ^{61}Co	19-54
^{65}Cu (n, p) ^{65}Ni	31-60
^{64}Zn (n, p) ^{64}Cu	8-35
^{67}Zn (n, p) ^{67}Cu	14-37
^{69}Ga (n, p) ^{69m}Zn	22-45
^{79}Br (n, p) ^{79m}Se	10-33
^{92}Mo (n, p) ^{92m}Nb	18-50
^{69}Ga (n, α) ^{66}Cu	38-74
^{93}Nb (n, α) ^{90m}Y	18-40
^{115}In (n, n') ^{115m}In	20-31

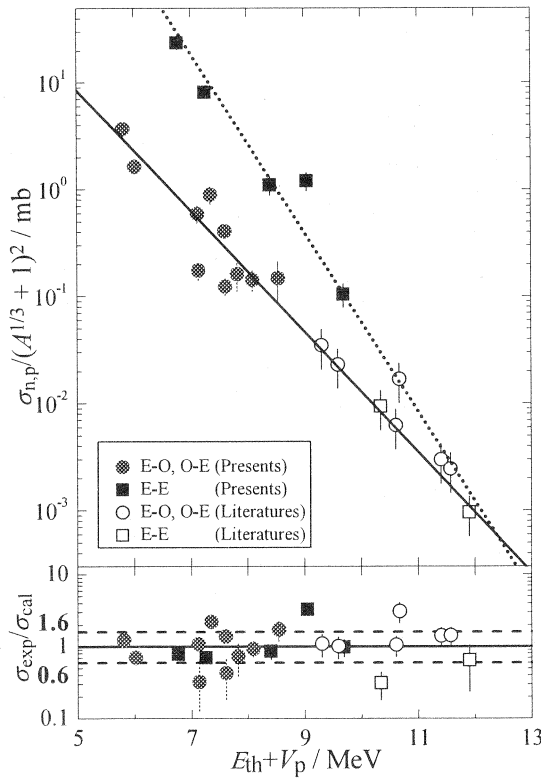Fig.4. Cross section data for the twelve (n, p) reactions and two (n, α) reactions

Fig.5. The relationship between $\sigma_{n,p}/(A^{1/3} + 1)^2$ and $(E_{th} + V_p)$, where $\sigma_{n,p}$, A and $(E_{th} + V_p)$ are the cross section of the (n, p) reaction at an energy of 5.0 MeV, the mass number and sum of threshold energy and the Coulomb barrier, respectively.

3.3 Neutron induced proton production from carbon at 175 MeV

Masateru HAYASHI[1,*,†], Yukinobu WATANABE[1], Riccardo BEVILACQUA[2],
Jan BLOMGREN[2], Leif NILSSON[2], Angelica ÖHRN[2], Michael ÖSTERLUND[2],
Stephan POMP[2], Alexander PROKOFIEV[3], Vasily SIMUTKIN[2],
Pär-Anders SÖDERSTRÖM[2] and Udomrat TIPPAWAN[4]

[1]Department of Advanced Energy Engineering Science, Kyushu University, Kasuga, Fukuoka, 816-8580, Japan
[2]Department of Neutron Research, Uppsala University, Box 525, SE-751 20 Uppsala, Sweden
[3]The Svedberg Laboratory, Uppsala University, Box 533, SE-751 21 Uppsala, Sweden
[4]Fast Neutron Research Facility, Chiang Mai University, P.O.Box 217, Chiang Mai 50200, Thailand
Email: teru@aees.kyushu-u.ac.jp

We have measured double-differential cross sections for proton production from carbon induced by 175 MeV quasi mono-energetic neutrons using the MEDLEY setup at the new TSL neutron beam facility. The present measurement is used for benchmarking of the high-energy nuclear data file, JENDL/HE-2004, and both GNASH and quantum molecular dynamics (QMD) calculations.

1. Introduction

Recently, there have been increasing nuclear data needs for neutron-induced light-ion production at intermediate energies (20 to 200 MeV) for various applications related to neutron transport and dosimetry for radiation safety and efficiency calculation of neutron detectors, *etc.* To satisfy these needs, a series of experiments were performed successfully for several targets at 96 MeV using the quasi mono-energetic neutron facility at the The Svedberg Laboratory (TSL) in Uppsala [1-3]. Afterward, the facility was upgraded toward measurements using more intense neutrons with higher energies.

The first measurement was performed of neutron-induced light-ion production from carbon at 175 MeV (hereafter called Exp-I) at the new TSL neutron beam facility [4,5]. Preliminary results have been reported in Ref.[4]. After the first measurement, the neutron beam line was reinforced by installing an additional iron shielding in order to reduce background neutrons. In addition, ΔE detectors 500 μm thick were replaced by those 1000 μm thick to improve participle identification in the high emission energy range. In the present work, we have carried out the second experiment for carbon (hereafter called Exp-II). The result is reported in comparison with the result of Exp-I. Also, the benchmark of evaluated nuclear data and theoretical model calculations are presented.

2. Experimental method

Figure 1 shows the new Uppsala neutron beam facility at TSL and the experimental setup of MEDLEY[6] experiments. Protons from the Gustaf Werner cyclotron impinge on an enriched ^{7}Li target (99.99% ^{7}Li), and neutrons are produced by the ^{7}Li(p,n) ^{7}Be reaction. In both the experiments, Exp-I and -II, 180 MeV protons produced neutrons with the peak energy of 175 MeV using 23.5 mm thick Li target. Protons passing through the Li target are bended by LISA magnet and transported to the beam dump.

Produced neutrons are transported to the reaction target placed at the center of MEDLEY chamber after passing through a 100 cm long and conical iron collimator whose diameter is 54 mm at the end of collimator. An iron shielding wall 100 cm wide, 200 cm high and 100 cm long is located around the iron collimator. The relative neutron beam intensity is monitored by the integrated proton beam current at the beam dump and by both a thin film breakdown counter and an ionization chamber mounted downstream of the MEDLEY setup.

In the renewal beam line in Exp-II, a 50cm thick iron wall was placed just in front of the MEDLEY in order to reduce background neutrons leading to reduction of accidental coincidence in DAQ system. Installment of this additional iron wall extended the distance between the Li target to the center of MEDLEY by 86 cm.
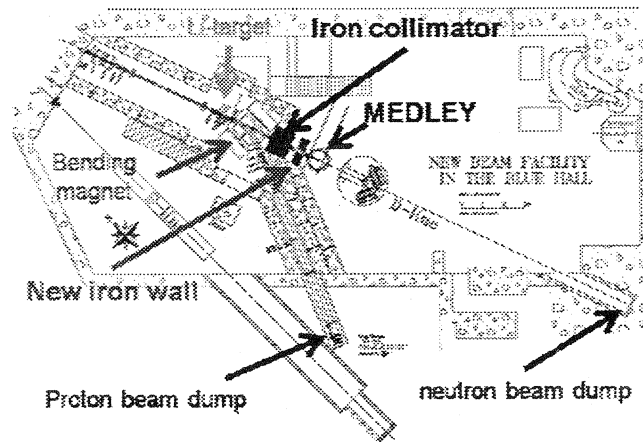

Fig. 1 Upgraded TSL neutron beam facility and experimental setup of MEDLEY.

The MEDLEY setup and construction details of each telescope are illustrated in Fig. 2. The MEDLEY consists of eight three-element telescopes mounted inside a vacuum chamber with a diameter of 90 cm. Each telescope has two silicon surface barrier detectors (either 50 or 60 μm thick and 23.9 mm in diameter for the first one, and either 400~600 μm thick(Exp-I) or ~1000 μm thick(Exp-II) and 23.9 mm in diameter for the second one) as ΔE detectors and one CsI(Tl) detector (100 mm long and 50 mm in diameter) as E detector The size of E-detector is enough to stop high-energy protons produced in the 175 MeV experiment. They have a cylindrical shape with 50 mm diameter, where the last 30 mm are taped to 18 mm diameter to match the size of a Hamamatsu S3204-08 photodiode for the light readout. The use of the ΔE-ΔE-E technique results in good particle identification over the energy range from a few MeV to 180 MeV.

A thin carbon target was placed at the center of the MEDLEY chamber. It was 22 mm in diameter and 1.0 mm thick. For absolute cross section normalization, a polyethylene (CH_2) target 25 mm in diameter and 1.0 mm thick was used. Instrumental backgrounds were also measured by removing the target from the neutron beam.

Since the ^{7}Li(p,n) reaction produces peak neutrons and low-energy tail neutrons, time-of-flight (TOF) measurements are used to reject the tail neutrons. The TOF data were measured as a time difference between master trigger signal and RF timing signal from the cyclotron.
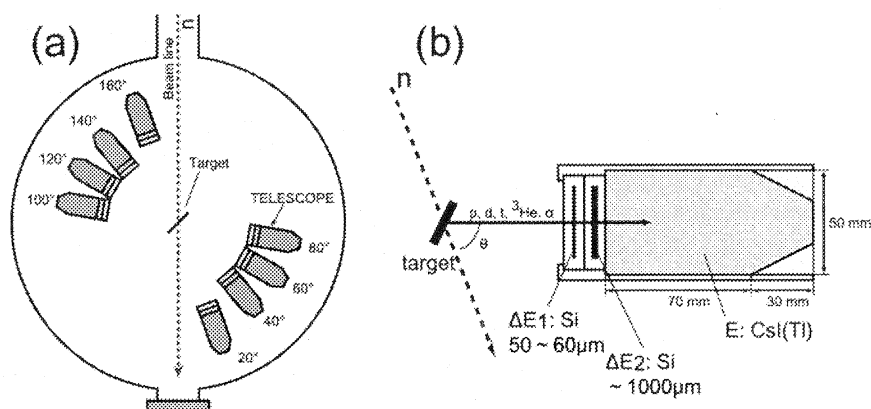

Fig. 2 MEDLEY setup: (a) arrangement of eight telescopes inside the MEDLEY chamber, (b) construction details of telescope.

Experimental conditions for individual experiments I and II are summarized in Table 1. The neutron flux was about 1×10^5 [n/s/cm^2] with the proton intensity of 0.3 μA at the MEDLEY target position. The effective beam time (30 hours) in Exp-II was twice as long as that (15 hours) in Exp-I.

Table 1. Summary of experimental conditions for Exp.-I and –II

Experiment	I	II
Proton energy [MeV]	178.7	179.3
Max proton current [μA]	0.3	
Li target thickness [mm]	23.5	
Peak neutron energy [MeV]	174.3	174.9
Peak neutron flux* [n/s/cm^2]	1×10^5	
Neutron flight path [cm]	374	460
Carbon target size (diameter x thick) [mm]	22 x 1.0	
ΔE_2 thickness [μm]	400~600	1000

*: at MEDLEY target position

3. Data analysis

Data analysis procedure based on ΔE-E technique is basically same as in the previous 96 MeV measurements[1,3,6]. Fig. 3 shows an example of the data analyses for Exp-II.

Energy calibration of all detectors is obtained using the data themselves. Events in the ΔE-E bands are fitted with respect to the energy deposition in the ΔE silicon detectors, which is determined from the thickness and the energy losses calculated with SRIM code[7]. For the energy calibration of the E detectors, the following approximate expression is applied to hydrogen isotopes due to the non-linear relationships between light output and energy deposition in the CsI(Tl) scintillator[8]:

$$E = a + bL + c(bL)^2 , \tag{1}$$

where L is the light output, and a, b and c are the fitting parameters. The parameter c depends on the kind of charged particles At Exp-II, c parameter was found to be 0.0028 for protons. The solid lines in Fig.3 (a) and (b) present the calculated energy loss curves for individual light ions, which reproduces well experimental ΔE_1-ΔE_2 and ΔE_2-E bands.

The measured TOF data shown in Fig.3 (c) are used for selection of light-ion events induced by neutrons corresponding to the main peak of source neutron spectrum.
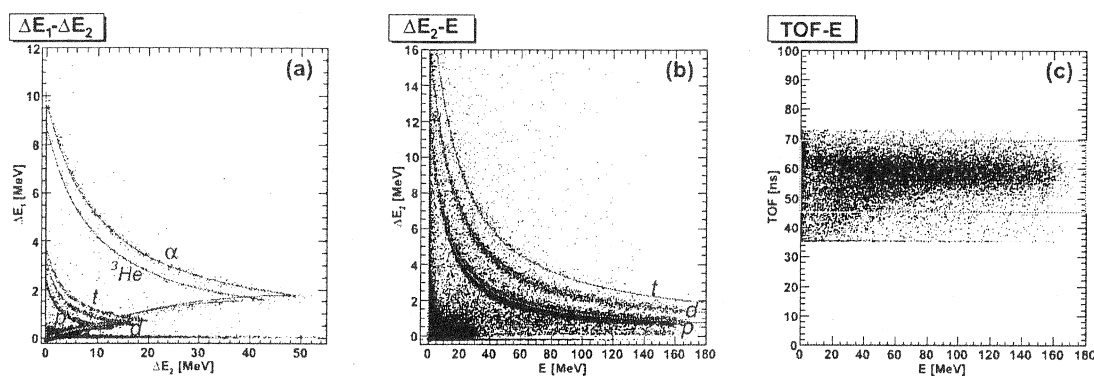

Fig. 3 Two-dimensional scatter plots of energy calibration and particle identification for (a) ΔE_1-ΔE_2 and (b) ΔE_2-E. The solid lines correspond to calculated energy losses. (c) Two-dimensional scatter plots of TOF vs. E. The events surrounded by solid line correspond to peak neutrons.

The efficiency correction due to the reaction losses in the CsI(Tl) scintillator has been reported elsewhere[9]. It was estimated for proton energies up to 200 MeV on the basis of the PHITS[10] calculation. The result was validated by the experiment using 160 MeV protons.

The number of the net counts due to *np* scattering is obtained using measurements at 20° for both CH$_2$ and

C targets. The (n,p) scattering spectrum is obtained by subtracting carbon contribution from CH_2 which shown in Fig. 4. Finally, the absolute value of measured cross section are determined using the reference np cross section in the same method as in Refs.[1,3,6] with using the equation below,

$$\frac{\sigma_C}{N_C} = \frac{\sigma_H}{N_H} \frac{2M_C}{M_{CH_2}} \frac{t_{CH_2}}{t_C} \frac{\phi_{CH_2}}{\phi_C} \frac{\Omega_{CH_2}}{\Omega_C} \frac{f_{CH_2}}{f_C}$$

(2)

where σ is the cross section, N is the net counts in a certain energy bin, M is the molecular mass, t is the target thickness, Φ is the relative neutron flux, Ω is the solid angle and f is the effective efficiency which includes energy loss effect in the CsI(Tl) scintillator. The np scattering cross section are taken from NN-online[11]. In Eq.(2), the solid angle Ω is assumed to be a point source. We have confirmed that this assumption is valid by a comparison of PHITS simulation between a point source and a plane source, in which the difference is only 1%.
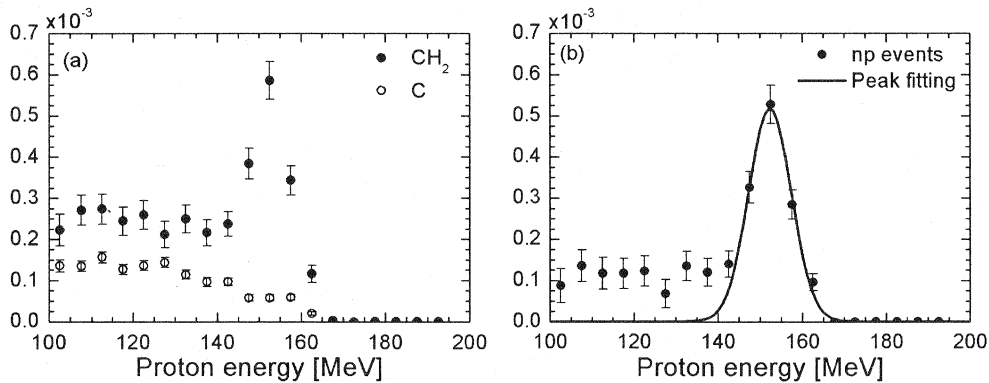

Fig.4   Measured np scattering peak: (a) the contribution from C in the CH_2 data and (b) the net np peak with Gaussian fitting.

The incident neutron spectrum accepted by the TOF gate was estimated from data analysis of the recoil protons from np scattering in the measurement of the CH_2 target. Fig. 5 shows the result together with the source neutron spectrum calculated using an empirical formula[12]. Both the spectra are normalized so that each peak corresponding to 175 MeV is unity. The calculated spectrum is folded using a Gaussian function with the same width as the experimental energy resolution. Both measured results for Exp-I and –II coincide within errors. The measured neutron spectra show good agreement with the calculated one. The hatched region above 95 MeV corresponds to the accepted neutron spectrum in both the measurements.
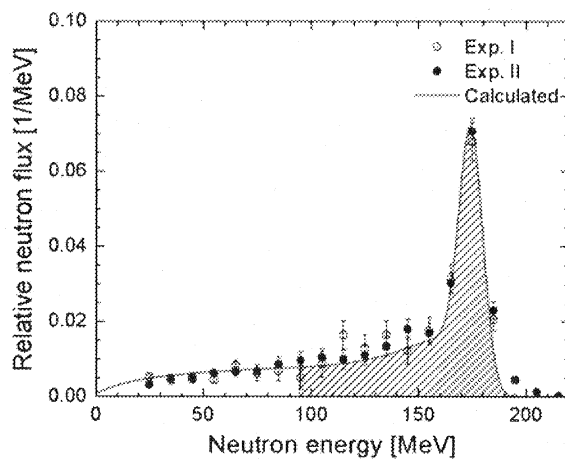

Fig. 5 Measured incident neutron spectra for each experiment and calculated one.

Proton spectra of the C(n,xp) reaction measured at 20 and 40 degrees are compared for both the measurements, Exp-I and –II, in Fig.6. Both show good agreement within errors except in the energy range

below 50 MeV. The difference may be due to rather worse particle identification in the first experiment, Exp-I.
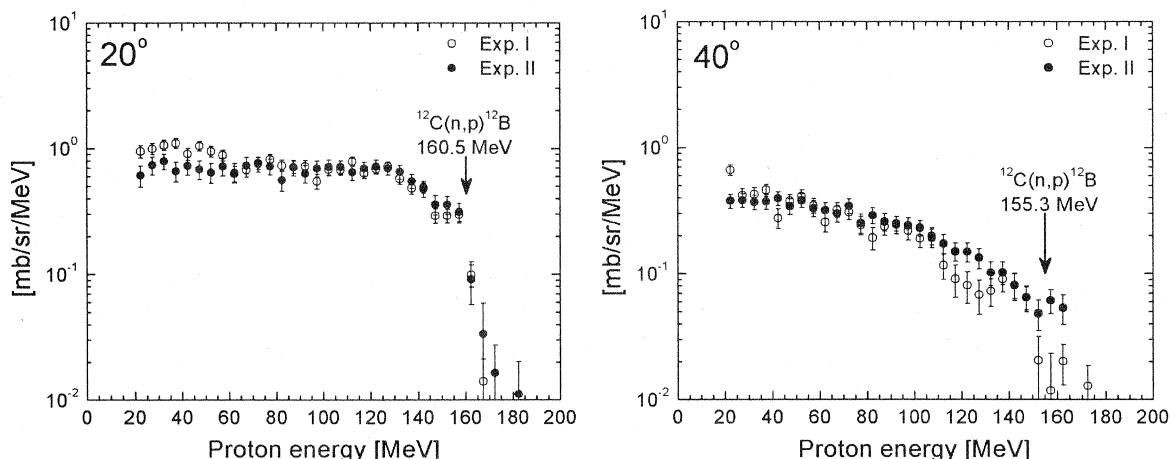

Fig. 6 Measured C(n,p) spectra at 20 and 40 degrees.

4. Benchmark of nuclear data and theoretical models

The measured data are used for benchmarking of high-energy nuclear data library and theoretical models. As mentioned in the preceding section, the experimental data contains the events from tail-neutron down to 95 MeV. Therefore, the measured spectra should be compared with the following folding spectrum:

$$\sigma^{fold} = \int_{E_{lower}}^{E_{upper}} \sigma^{eval}\left(E_n, E_p, \theta_p\right) f\left(E_n\right) dE_n , \tag{3}$$

where $f(E_n)$ is the accepted neutron spectrum corresponding to the hatched area in Fig. 5, and E_{lower} (=95MeV) and E_{upper} (=180 MeV) are the lower and upper limits of the neutron energy selected by TOF cut, and σ^{eval} is the calculated cross section.

The evaluated nuclear data and theoretical models to be benchmarked in the present work are JENDL/HE-2004 evaluated nuclear data file[13], statistical model calculations including preequilibrium emission with GNASH code [14], and QMD calculation [15]. Fig. 7 shows the results for 20 and 40 degrees. The GNASH calculation reproduces the measurement over the whole energy region better than the other calculations. The QMD and JENDL/HE-2004 results overestimate the high-energy end at 20 degrees.
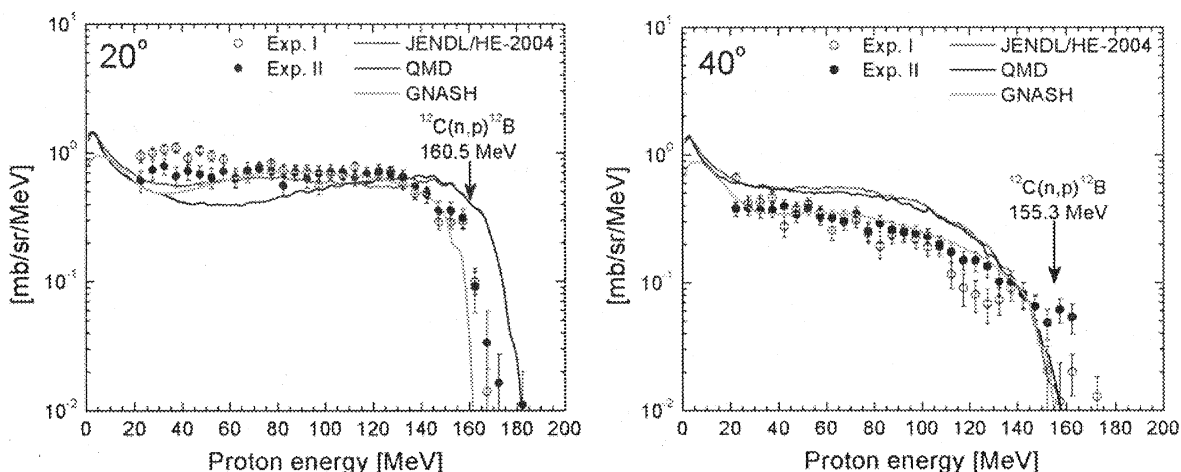

Fig. 7   Comparison between measured (n,xp) spectra at 20 and 40 degrees and calculation results of JENDL/HE, GNASH and QMD models.

5. Summary and conclusions

We have measured the double-differential cross sections of (n,xp) reactions on C at 175 MeV using the new Uppsala neutron beam facility twice. The comparison between the first and second measurements indicates that use of additional iron shielding and thicker ΔE detectors led to improvement of particle identification and reduction of background neutrons. Good agreement between both the measured data proves the reliability of the MEDLEY measurement. The data analysis for the second measurement is still in progress, particularly for low energy component measured by a combination of two ΔE detectors.

The result of benchmarking shows that the GNASH calculation can reproduce measured cross section better than the QMD calculation and JENDL/HE-2004 data. More detailed analyses including the ranges of low proton energies and larger angles will be necessary to draw a final conclusion about the benchmark.

Acknowledgements

References

[1] U. Tippawan, *et al.*, Phys. Rev. C **69**, (2004) 064609.
[2] V. Blideanu, *et al.*, Phys. Rev. C **70**, (2004) 014607.
[3] U. Tippawan, *et al.*, Phys. Rev. C **73**, (2006) 034611.
[4] M. Hayashi, *et al.*, in Proc. of Int. Conf. on Nuclear Data for Science and Technology, Nice, France, April 22-27 (2007).
[5] S. Pomp, *et al.*, in Proc. of Int. Conf. on Nuclear Data for Science and Technology, Santa Fe, USA, (2005) p780.
[6] S. Dangtip, *et al.*, Nucl. Instr. and Meth. A **452**, (2000) 484-504.
[7] J.F. Ziegler, *et al.*, the Stopping and Range of Ion in Solids, Pergamon Press, New York, 1985.
[8] D. Horn, *et al.*, Nucl. Instr. And Meth. A **320**, (1992) 237-276.
[9] M. Hayashi, *et al.*, Engineering Science Reports, Kyushu Univ. Vol. **29**, No. 4, (2001). (in Japanese).
[10] H. Iwase, *et al.*, J. Nucl. Sci. And Technol. **39**, (2002) 1142-1151.
[11] SAID Nucleon Nucleon scattering data base, Available from Center for Nuclear Studies, Department of Physics, George Washington University, USA. URL: http://gwdac.phys.gwu.edu.
[12] A. Prokofiev, *et al.*, in Proc. of Int. Conf. on Nuclear Data for Science and Technology, Tsukuba, Japan; J. Nucl. Sci. and Technol., Suppl.2, (2002), p.112.
[13] Y. Watanabe, *et al.*, in Proc. of Int. Conf. on Nuclear Data for Science and Technology, Santa Fe, USA, (2005), p326.
[14] P. G. Young, *et al.*, Los Alamos National Laboratory Report No. LA-12343-MS, (1992).
[15] K. Niita, *et al.*, Phys. Rev. C **52**, (1995) 2620-2635.

3.4 Study of a new crystal array detector to measure double differential cross sections of proton-actinide reactions in 600-MeV region

Y. Koba[1], Z. Tsamalaidze[2], P. Evtoukhovitch[2], M. Imamura[1], H. Iwamoto[1], V. Kalinnikov[2], W. Kallies[2], N. Khomutov[2], N. Kuchinski[2], A. Moiseenko[2], D. Mzavia[2], V. Samoilov[2], T. Fukahori[3], K. Kiyohara[1], Y. Uozumi[1], G. Wakabayashi[1]

[1] *Department of Applied Quantum Physics and Nuclear Engineering, Kyushu University, Motooka 744, Fukuoka 819-0395, Japan*
[2] *Joint Institute for Nuclear Research, JINR, 141980 Dubna, Russia*
[3] *JAEA, 4-49 Muramatsu, Tokai-mura, Naka-gun, Ibaraki 319-1184, Japan*

A new crystal array detector is proposed to conduct charged particle cross section measurements with actinide targets for a study of accelerator transmutation of waste. The detector enables both the Time-of-Flight and the Pulse-Height measurements in an energy range around 600 MeV. From the simulation designs, it was revealed that the detector has great potential to realize a moderate energy resolution and a wide energy acceptance.

1. Introduction

The accelerator driven system (ADS) has been recognized as one of most attractive options for the nuclear transmutation of high level nuclear waste. One may expect ADS to reduce a hazard level of the waste dramatically, and to operate as an energy generator. To realize ADS, it is necessary to conduct various areas of fundamental researches and technical developments. Double differential cross section (DDX) data of nucleon-actinide reactions are of highly importance for the nuclear waste transmutation facilitated by ADS. Since charged particle emission data are strongly required as well as neutron data up to 1500 MeV, we plan to conduct charged particle measurements with typical actinide targets at the cyclotron facility, the Joint Institute for Nuclear Research, Dubna, in the energy range 200 to 700 MeV.

In order to obtain high-quality nuclear data of DDX, one needs to use a detector that offers a moderate energy resolution of a few percent and a wide energy acceptance covering from almost zero up to the maximum emission energy. Moreover, detection efficiency should be high enough for the usage of a thin target. A crystal array detector is the most suitable one to these conditions, and the only solution above 100 MeV. However, there are some crucial problems when one uses it at energies of around/above 600 MeV.

In the present article are described a design study of a new crystal array detector that combines the Time-of-Flight (TOF) and the Pulse-Height (PH) measurement. In addition we reports characteristics of scintillation crystals of GSO(Ce) and LYSO(Ce), which are considered to be the best candidate as the detector element, because of its relatively high light output and very short scintillation decay constant, investigated through experiments using charged particle beams.
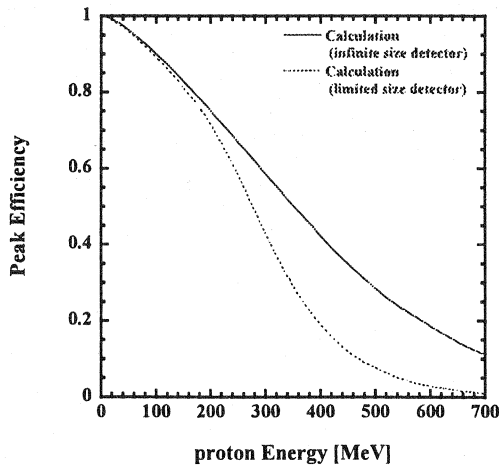
Fig. 1. The calculated peak efficiency of GSO(Ce) crystal to protons. See text for more detail.
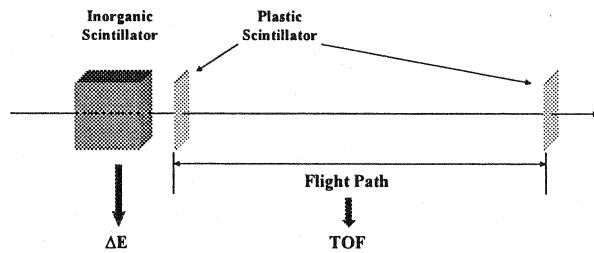
Fig. 2. Sketch of the detector concept. The system consists of dE and TOF measurement parts. See text for more detail.

2. Crystal array detector for charged particles

2.1 Difficulties of present methods

When one applies a crystal detector to measure charged particle energies of several hundreds MeV, the particle identification (PI) analysis is most useful to deduce DDXs. However, the PI analysis is recognized to become insufficient in a high energy range. This is because the peak efficiency, the ratio of the number of full energy peak events to the total events, decreases to a level where the PI analysis is no longer applicable.

In Fig. 1 are shown typical examples of the peak efficiency curves of GSO(Ce) crystal to protons as a function proton energy. They were calculated by the simple Monte Carlo procedure [1,2]. The dotted line is the calculated efficiency for a crystal having a cross section of 43 mm x 43 mm, which should be the largest possibly present days. It is found that the curve drops rapidly above 200 MeV and approaches to zero at around 600 MeV. The solid line is that for infinite size crystal, of which the efficiency is determined solely by the nuclear reactions and remains to be about 20% at 600 MeV. However, the crystal dimension must be unreasonably large. In addition to this low efficiency, the 2D PI plot which is necessary for the PI analysis is known to scatter widely and obscure at these energies. Thus, it will be concluded that the conventional PI analysis is not very useful in this energy range.

Although there are some alternative options such as the unfolding analysis and the TOF technique, they have also serious difficulties. The unfolding analysis suffers from a large ambiguity when it is applied to continuum energy spectra. Although TOF is effective to detect high energy protons, its efficiency becomes very low due to a long flight path length that leads to an extremely small solid angle and a large portion of beam bunch thinning-out in cyclotrons. Moreover, it is impossible to realize a wide energy acceptance with a long flight path in charged particle measurements under atmosphere.

2.2 Proposal of new detector system used in 600 MeV range

In order to meet the criteria discussed above, we propose a new detector system which enables nuclear data measurement in a 600 MeV range. It utilizes both the pulse height and TOF in proton measurements. As the concept is illustrated briefly in Fig.2, it consists from two sections; one is a crystal detector based on the ordinal dE-E method, and the other the TOF section following the crystal.

The crystal detector works as an E detector for low energy protons and an energy degrader for high energy protons. Since low energy protons stop in the crystal, one needs not the beam bunch thinning-out in cyclotron operations. The shorter flight path length, which is realized by the degrader, offers great advantages: the larger solid angle and easy preparation of a vacuum duct to cover the flight section which is essential for charged particle measurements. The detector proposed presently is expected to offer the best characteristics to fulfill required specifications, such as energy resolution and energy acceptance.

3. Design study of new detector system

3.1 Specifications

Since we have a lot of experiences in this kind of experiment, we decided to determine the specifications by following the parameters optimized in the previous experiments [3-5]. The detector we used had the solid angle of about 1 msr. The energy resolution of GSO(Ce), which was operated for the dE-E method, was 5 to 10%. Furthermore, the peak efficiency of at least 50% was found to be preferable to perform the most reliable PI analysis. Although the deeper crystal results in the more loss of particles, the following TOF section is benefited from the less number of particles. It seems reasonable to determine the crystal depth as to be equivalent with 50% of the peak efficiency.

The basic criteria for the TOF section should come from difficulties in manufacturing and placing a long vacuum line. A one-meter long duct should be reasonable, and an enough area to be installed is available in the planned experimental hall of JINR. Moreover, the spread in time measurement appears also to be reasonable as discussed in the following section.

The specifications targeted in this study are summarized as below:
- Energy resolution is 10%.
- Solid angle is 1msr.
- Peak efficiency of crystals is at least 50%.
- The fight path is one meter.

3.2 Depth of crystal and peak efficiency

As found from Fig. 1, the proton energy range where the peak efficiency approaches 50% is around 300 MeV. The crystal depth needed to stop protons of 300 MeV is about 120 mm. Since the dimension of cubic GSO(Ce) crystals available presently is 43 mm in the edge length, two or three crystals must be placed in the front section.

When 600 MeV protons pass through a crystal with this thickness, 32% of protons will be lost due to nuclear reactions as a result of calculation. The survivors can enter the TOF section. It is preferable to decrease the number of particles in view of avoiding interferences between two particles accidentally appear in the TOF simultaneously. The crystal depth of 86 mm will be the best to fulfill these requirements.

3.3 Energy resolution

The estimated energy resolution in the sole TOF section after crystal is shown in Fig.3, as a function of proton energy and the depth of crystal section of 0, 43, 86 and 129 mm. It is apparent that the TOF energy resolution improves as the crystal section becomes deeper. In this case, we have assumed the whole timing resolution to be 100 ps, which could be standard with fast plastic scintillator detectors. A resultant resolution was, for instance, about 30% at 600 MeV. However, we expect to have the better resolution by including additional information from crystal detector in actual measurements.
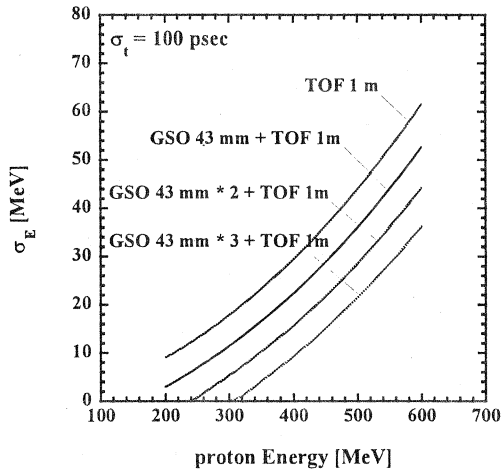
Fig. 3. Estimated energy resolutions for TOF as a function of proton energy and degrader (crystal detector) thickness.
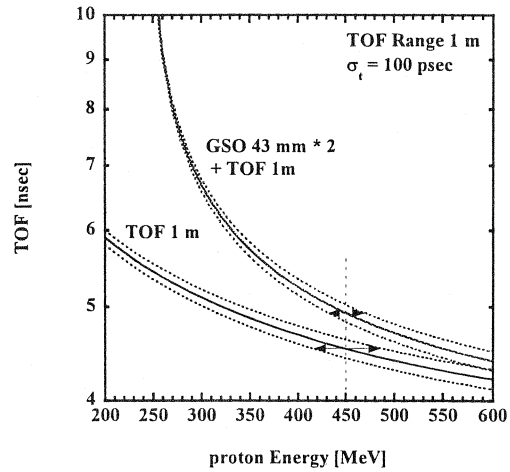
Fig. 4. Estimated energy resolution as a function of proton energy compared with/without crystal as energy degrader.

The advantage of this method is demonstrated in Fig.4, which compares the time of flight with/without the degrader crystal under the flight path length of one meter. The effect of crystal degrader is significant, and helps to improve the energy resolution.

3.4 Solid angle and fight path

The detector solid angle is shown in Fig.5 as a function of flight path length, and compared between three different dimensions of square plastic scintillator of 40, 80 and 120 mm on a side. At a flight path of one meter, the solid angle of 1msr is realized with that of 80 mm.

This plastic cross section is reasonable from view points of manufacturing a vacuum duct and the time spread due to different flight path from the scintillation source to the photocathode in a photomultiplier.

3.5 Energy Straggling

In this method, the crystal causes the energy straggling of the penetrating particles, and the energy resolution of the total system descends. We estimate this energy straggling using the Geant4 code. Fig.6~8 show the energy spectra of the particles after penetrating crystal. Fig.6 shows that the energy straggling doesn't depend on the initial energy well. Fig. 7 and 8 shows the energy spectra after penetrating GSO(Ce) crystal of various thickness. These figures show that the energy straggling largely depends on the length of dE crystal. The long length of dE crystal improves resolution of TDC by degrading particle energy, but spreads particle energy by straggling and decreases resolution of energy identification. The length of crystal are very important for the resolution. We must further investigate the energy resolution of the total system

3.6 Detector arrangement

As a result of the above discussion, we decided the detector arrangement as shown in Fig.9 The low energy part consists from stacked crystal detectors where the conventional dE-E measurements are made up to 300 MeV. Protons of energies higher than 300 MeV are measured by the TOF detector. It consists of two plastic scintillators with a one-meter flight path length. The end plastic is a square 100 mm on a side. Excluding the

effect of energy straggling, the expected energy resolution is about 10% for 450 MeV protons. This design almost satisfies the performance we targeted in this study.

4. Conclusion

A new type of detector system was studied to measure double differential cross sections of proton productions from proton-actinide reactions at around 600 MeV. The detector system is based on a combination of dE-E and TOF measurements to realize a moderate energy resolution and an extremely wide energy acceptance. On the base of the calculations, the detector arrangement has been optimized in terms of crystal dimensions, TOF path length, and more.

Acknowledgment
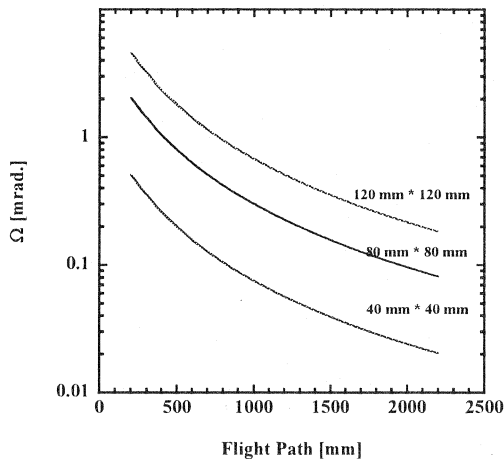
Fig. 5. The detector solid angle as function of flight path length and dimension of TOF end detector.
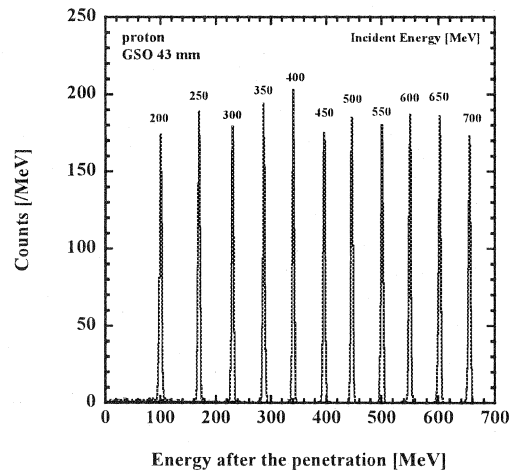
Fig. 6. The energy spectra after penetrating crystal. The depth of crystal is 43 mm.
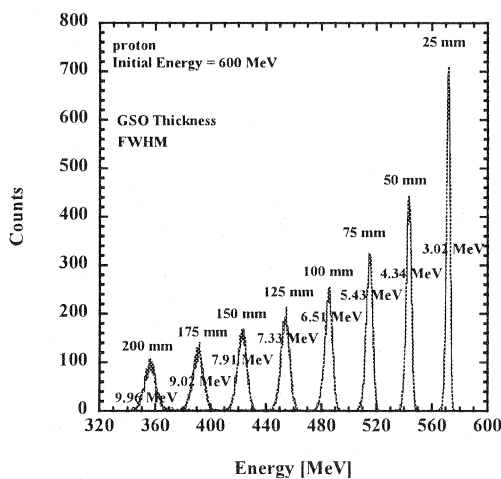
Fig. 7. The energy spectra of after penetrating crystal. Initial energy of proton is 600 MeV
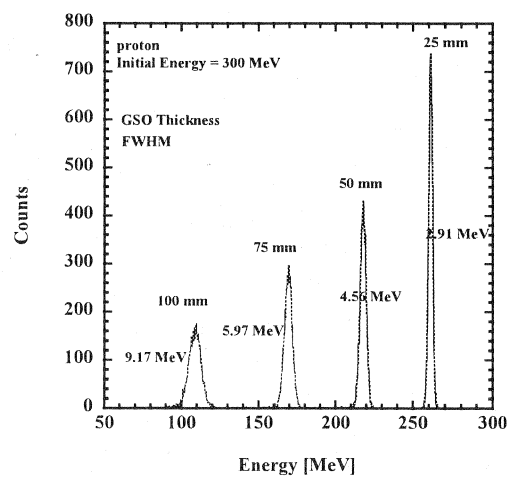
Fig. 8. The energy spectra of after penetrating crystal. Initial energy of proton is 300 MeV
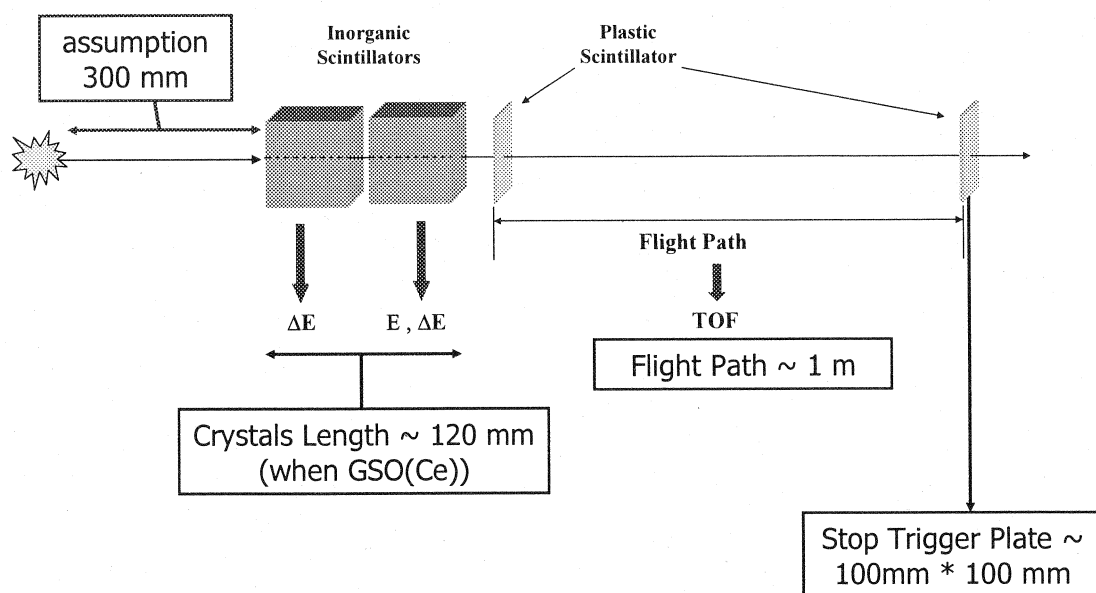
Fig. 9. The detector arrangement we decided.

References

[1]H. Yoshida et al., Nucl. Instr. & Meth. **A** 411, 46 (1998).

[2]F. Saiho et al., Nucl. Instr. & Meth. **A 537**, 594 (2005).

[3]Y. Uozumi et al., Journal of NUCLEAR SCIENCE and TECHNOLOGY, **Supplement 2**, 385 (2002)

[4]T. Kin et al., Physical Revew C, **Vol.72**, 014606 1-9 (2005).

[5]K. Anami et al., Nucl. Instr. & Meth. **A 404**, 327 (1998).

3.5 Nucleon Optical Potentials for the CDCC analysis of Deuteron Elastic Scattering from ^{6,7}Li

Tao Ye[1], Yukinobu Watanabe[1], Kazuyuki Ogata[2], Satoshi Chiba[3]

[1]*Department of Advanced Energy Engineering Science, Kyushu University, Kasuga, Fukuoka 816-8580, Japan*
[2]*Department of Physics, Kyushu University, Fukuoka 812-8581, Japan*
[3]*Advanced Science Research Center, Japan Atomic Energy Agency, Tokai, Ibaraki, 319-1195 Japan*
Email: yetao@aees.kyushu-u.ac.jp

Phenomenological nucleon optical model potentials of ^{6,7}Li up to 50 MeV are obtained on the basis of the neutron optical model potential of ^{6}Li. They are applied to the analysis of deuteron elastic scattering up to 50MeV using the CDCC method. The optical model calculation with the obtained nucleon optical potentials reproduces well the experimental data of neutron and proton elastic angular distributions and neutron total cross sections, and also the CDCC calculation with the nucleon optical potentials for deuteron elastic scattering from ^{6,7}Li shows overall good agreement with the measurement.

1. INTRODUCTION

The International Fusion Materials Irradiation Facility (IFMIF) [1] is composed of an accelerator-driven deuteron-lithium neutron source for irradiation tests of fusion reactor candidate materials. Neutrons up to about 55 MeV will be produced by two 125 mA beams of 40 MeV deuterons bombarding a thick target of flowing liquid lithium. The neutrons are generated by d-Li stripping, breakup and other reaction processes. The McDelicious code [2-5] developed in Forschungszentrum Karlsruhe (FZK) is used to calculate the neutron source in IFMIF with the evaluated d+^{6,7}Li cross sections. The McDelicious code can reproduce well both thick target yield (TTY) and double differential cross sections (DDX) [6]. In evaluation of d+^{6,7}Li nuclear data [5], compound nucleus reactions, pre-equilibrium processes, stripping and direct interactions have been taken into account as the related reaction mechanisms. Since the deuteron is a loosely-bound nucleus composed of a neutron and a proton, the deuteron breakup is expected to contribute to the Li(d,xn) reaction if the incident energy is larger than its binding energy. Therefore, it will be necessary to include the breakup process explicitly in the analysis of the Li(d,xn) reaction.

One of the promising quantum-mechanical approaches to describe the deuteron breakup process is the Continuum-Discretized Coupled Channels (CDCC) method, which has so far been applied successfully to the analyses of the data of C, Ni and Cu [7, 8], but not Li. Recently, an example has been reported of the CDCC calculation of the (d,n) reaction on ^{7}Be [9], a mirror nucleus of ^{7}Li, at 8 MeV. The CDCC method deals with the deuteron breakup process using a phenomenological three-body hamiltonian in which the nucleon-nucleus interaction is represented by the optical model potential (OMP) at half the deuteron incident energy and an effective nucleon-nucleon potential is used for the p-n interaction. The nucleon-nucleus OMP is the most important input quantity in the CDCC method. Before analyzing the breakup contribution in the Li(d,xn) process, it is worthwhile to study d-Li elastic scattering and reaction cross sections using the CDCC method in order to derive the proper nucleon-lithium OMPs. This is the purpose of this work.

In the following sections, we describe the derivation of the nucleon OMP of lithium first, and then analyze nucleon elastic scattering and total cross sections using the OMP. Finally, the result of the CDCC calculation for deuteron elastic scattering is presented.

2. OPTICAL MODEL POTENTIAL OF LITHIUM

As a powerful tool, the optical model is applied successfully to calculate angular distributions of elastic scattering, total cross sections and reaction cross sections. Nucleon OMPs, especially neutron OMPs, are the most successful example, and have been studied intensively. Recently, the global nucleon OMPs [10, 11] have been applied satisfactorily to calculations of deuteron induced elastic and reaction cross sections using the CDCC method by P. Chau Huu-Tai [12]. The Dave-Gould OMP for neutron on light targets was also applied to ^{7}Be [9] using the

CDCC method. However, the mass range of the target nuclei in [12] is larger than A=16, and the analysis in [9] has only one incident energy point. Thus, we have decided to derive the proper nucleon-^{6,7}Li OMP for the CDCC analysis of d-^{6,7}Li at nucleon incident energies up to 25MeV in the present work.

There are many experimental data of total cross sections and neutron elastic angular distributions for ^{6,7}Li at energies of our interest. However, it is known that the neutron data of ^{7}Li contain inelastic scattering contribution to the first excited state of ^{7}Li, 0.478MeV state. It would be difficult to determine reliable neutron OMP of ^{7}Li from the elastic scattering data by a conventional method of OMP parameter search. Also the number of the proton data of ^{7}Li is very limited in comparison with those of ^{6}Li. Therefore, we propose a method to determine the nucleon OMPs of ^{7}Li on the basis of those of ^{6}Li. As for ^{6}Li, the neutron OMP obtained by Chiba et al.[13] is available for our purpose, which explains fairly well the angular distributions of ^{6}Li(n,n) ^{6}Li at energies up to 24 MeV. The OMP will be referred to the Chiba OMP hereafter.

We choose the following potential forms from the Chiba OMP:

$$U = -(V_r + iW_v) f(r, r_v, a_v) + 4ia_d W_d \frac{d}{dr} f(r, r_d, a_d) + \left(\frac{\hbar}{m_\pi c}\right)^2 (\vec{l} \cdot \vec{s}) V_{SO} \frac{1}{r} \frac{d}{dr} f(r, r_{SO}, a_{SO}),$$ (1)

in which f is the Woods-Saxon form factor,

$$f(r, r_i, a_i) = \frac{1}{1 + \exp\left(\frac{r - r_i A^{1/3}}{a_i}\right)},$$ (2)

where r_i and a_i are the radius and diffuseness parameters, respectively, and A is the target mass number.

Since both neutron and proton OMP analyses of ^{6,7}Li are necessary, we extend the neutron OMP to the proton OMP by assuming the Lane model, and further extend the Chiba OMP so as to include ^{7}Li target by changing the Fermi energies. The depth parameters in Eq. (1) are listed below:

$$V_r = \left(V_0 + V_1 \pm 21\frac{N-Z}{A}\right)\left[1 - V_0 \frac{1 - e^{-\lambda_v(E-E_f)}}{V_0 + V_1}\right] + \left[\Delta V_C(E)\right]_{\text{for proton}}$$ (3)

$$W_v = W_{v_0} \frac{(E - E_f)^4}{(E - E_f)^4 + W_{v_1}^4}$$ (4)

$$W_d = \left(W_{d_0} \pm 16\frac{N-Z}{A}\right) e^{-\lambda_{W_d}(E-E_f)} \frac{(E - E_f)^4}{(E - E_f)^4 + W_{d_1}^4}$$ (5)

$$V_{SO} = V_{SO} \, e^{-\lambda_{SO}(E-E_f)},$$ (6)

where the (N-Z)/A term presents the isospin dependence, and the signs +/- are for proton and neutron OMPs, respectively. The coefficients of (N-Z)/A are taken from the Koning-Delaroche OMP [10]. The energy dependent function $\Delta V_C(E)$, is the Coulomb correction term for the proton OMP which follows Eq.(23) in Ref. [10]. All parameters in $\Delta V_C(E)$ are the same as those in Ref. [10].

The Fermi energy, E_f, is calculated using the following expressions:

$$E_{f_n} = -\frac{1}{2}\left[S_n(^A_Z X_N) + S_n(^{A+1}_Z X_{N+1})\right] \qquad \text{for neutron,}$$ (7)

$$E_{f_p} = -\frac{1}{2}\left[S_p(^A_Z X_N) + S_p(^{A+1}_{Z+1} X_N)\right] \qquad \text{for proton.}$$ (8)

In Eqs. (7) and (8), $S_y(X)$ is the separation energy of y (=neutron or proton) from the target. Finally, the Fermi energies of proton and neutron for ^{6,7}Li are given as

$$E_{f_n}(^6 Li) = -6.457 \, \text{MeV}$$

$$E_{f_n}(^6 Li) = -4.641 \, \text{MeV}$$

$$E_{f_p}(^7 Li) = -5.099 \, \text{MeV}$$

$$E_{f_p}(^7 Li) = -13.62 \, \text{MeV}.$$ (9)

3. Results and discussion

The extended Chiba OMP discussed above is applied to calculate four sets of nucleon elastic scattering experiments that we are interested in, ^{6}Li(n,n)^{6}Li, ^{6}Li(p,p)^{6}Li, ^{7}Li(n,n)^{7}Li, and ^{7}Li(p,p)^{7}Li. Two parameter sets of Chiba OMP marked as Set-1 and Set-2 are used in the calculations, because they agree with experimental data equally on ^{6}Li(n,n)^{6}Li reaction in Ref. [13]. And most of the parameters are the same as those in Ref. [13]. However, two parameters are slightly adjusted to get better agreement with experimental data. According to Delaroche et al. [14], the radius of the real volume term, r_v, is assumed to have a weak energy dependence. Therefore, r_v is adjusted by fitting the experimental data of neutron total cross, reaction cross sections and elastic scattering angular distributions simultaneously. W_{d0}, the parameter of imaginary surface depth term in Eq. [5], is also adjusted for ^{7}Li to fit the proton elastic scattering data. All parameters obtained in the present work are listed in Table 1.

TABLE 1. Nucleon optical model potential parameters for ^{6,7}Li. The quantities V_i and W_i are given in MeV, λ_i in MeV^{-1}, and r_i and a_i in fm.

Parameters	Set-1	Set-2	
V_0	65.64	71.68	
V_1	-26.71	-29.69	
λ_0	0.00486	0.00495	
r_v	$\begin{cases}1.55-0.035E_n \\ 1.19-0.01E_n \\ 1.34\end{cases}$	$\begin{cases}1.46-0.04E_n \\ 1.049+0.11E_n \\ 1.22\end{cases}$	$\begin{array}{l}E_n \in [5,8) \\ E_n \in [8,15) \\ E_n \in [15,25]\end{array}$
a_v	0.707	0.822	
W_{v0}	10.19	10.06	
W_{v1}	18.42	14.03	
W_{d0}	$\begin{cases}74.69 \\ 16\end{cases}$	$\begin{cases}312.4 \\ 16\end{cases}$	$\begin{array}{l}^6\text{Li} \\ ^7\text{Li}\end{array}$
W_{d1}	15.69	18.76	
λ_d	0.207	0.315	
r_d	1.59	1.37	
a_d	0.899	0.699	
V_{SO}	8.374	8.702	
λ_{SO}	0.01407	1.01407	
r_{SO}	1.58	1.64	
a_{SO}	0.427	0.311	

The optical model calculations are performed using the ECIS code [15], and the results are compared with the experimental data and two OMPs, which are the Dave-Gould neutron OMP [16] at energies from 7 MeV to 14 MeV, and the Watson proton OMP [17] at energies from 16 MeV to 50 MeV. The related total cross-sections are analyzed too. The comparisons are shown in Fig. 1(a)-(d). It should be noted that the result of ^{6}Li(n,n)^{6}Li is the same as in Fig.3 of Ref. [13] and is not included in this report. The experimental data used in the figures are from the EXFOR database [18]. In the calculations with the Dave-Gould OMP, the individual parameter sets (Table II in the Ref. [16]) are used for ^{6}Li and ^{7}Li, respectively, because they reproduce the experimental data better than the global parameter sets. The proton OMP based on the Dave-Gould neutron OMP is also constructed by introducing the asymmetry term and the Coulomb correction term. The results are plotted in Fig. 1(a)-(c). The results of the Watson OMP [17] for Li(p,p) are plotted in Fig.1.(a) and (c). Hereafter, the eOMP will be referred to the extended OMP which introduces the asymmetry term and the Coulomb correction term.

Both the calculations using the Chiba eOMPs with different parameters, Set-1 and Set-2, are almost same, although some small differences are seen at large angles. Their results of nucleon elastic angular distributions reproduce the experimental data fairly well at the forward angles as the other two OMPs do. Meanwhile, they deviate from the experimental data at intermediate angles in the ^{7}Li(n,n)^{7}Li at energies lower than 24 MeV. This might be
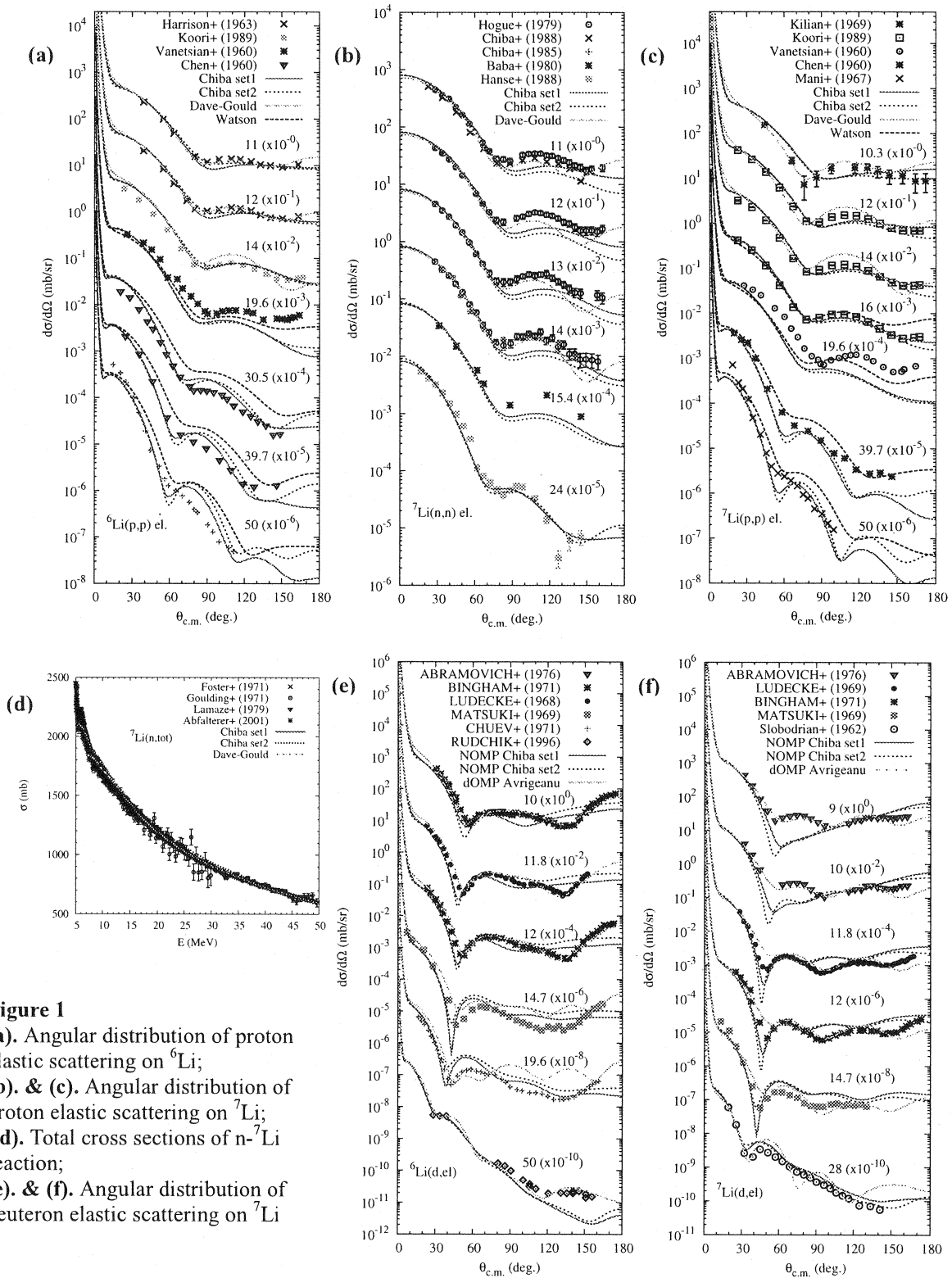
Figure 1

(a). Angular distribution of proton elastic scattering on ^{6}Li;

(b). & (c). Angular distribution of proton elastic scattering on ^{7}Li;

(d). Total cross sections of n-^{7}Li reaction;

(e). & (f). Angular distribution of deuteron elastic scattering on ^{7}Li

partly because the contribution of inelastic scattering to the first excited state is included in experimental data. There is a large discrepancy seen in ^{7}Li(p,p) at 19.6 MeV, which cannot be explained properly. Through the comparisons in Fig.1, it is concluded that at energies from 5 MeV to 50 MeV, the results with Chiba eOMP show overall agreement with the experimental data of elastic angular distributions and total cross sections to the similar extent of those of the Dave-Gould eOMP and Watson OMP.

Next, we perform CDCC calculations of deuteron elastic scattering cross sections with the obtained nucleon OMPs of ^{6,7}Li. The CDCDEU/HICADEU codes [20] are used in the present calculation. The nucleon OMPs at half the deuteron incident energy are required in the CDCC calculation. The deuteron ground state wave function is composed of $^3S_1$ state alone, and the D-states are neglected. The breakup states' wave functions contain the relative angular momentum of the p-n subsystem $l = 0$ and 2, $i.e.$, $^3S_1$, $^3D_1$, $^3D_2$, and $^3D_3$. The ground-state and breakup-state wave functions are constructed using Gaussian potentials [7]. The total number of the discretized continuum bins N_{bin} is set to be 12, and the maxim total angular momentum J_{max} is 20. And only opened-channels are considered. The convergences of N_{bin} and J_{max} have been checked so that the relative errors are less than 0.3% for deuteron elastic angular distributions. The Coulomb breakup effects are not included in our CDCC calculations. The reason is that lithium is the light nucleus in which the Coulomb interaction is much weaker than heavier nuclei, so that the Coulomb breakup effect is expected to be negligible [9].

The results are plotted in Fig.1.(e) to (f), and they agree with the results of phenomenological deuteron OMP [19] and experimental data at the forward angles. However, the CDCC results underestimate the first minimum on ^{7}Li(d,d)^{7}Li at energies below 14.7 MeV, and cannot fit well the experimental data at backward angles at all energies. The poor fittings on the first minimum of ^{7}Li(p,p)^{7}Li may lead to the failures on those of ^{7}Li(d,d)^{7}Li. And additional contributions from compound reaction mechanism and sub-cluster structure description on ^{6,7}Li [19] might improve the calculations at the backward angles.

4. Conclusions

First, we have obtained the phenomenological nucleon optical model potentials of ^{6,7}Li up to 50 MeV on the basis of the neutron optical model potential of ^{6}Li given by Chiba et al. [13]. It was confirmed that the optical model calculation with the obtained OMPs could describe well the nucleon angular distributions and neutron total cross sections of ^{6,7}Li in the energy range from 5 MeV to 50 MeV.

Second, the obtained nucleon OMPs was applied to the CDCC analysis of deuteron elastic scattering up to 50MeV. The calculation shows reasonably good agreement with the experimental angular distributions. Particularly, the good agreement is obtained at forward angles to the same extent to the optical model calculation with phenomenological deuteron OMP [19]. Such comparisons between nucleon OMPs and deuteron OMPs connected by the CDCC method will be helpful to evaluate both the nucleon and deuteron OMPs simultaneously.

Finally, the success in applying the CDCC calculation to deuteron elastic scattering from ^{6,7}Li encourages us to use the CDCC method to predict neutrons produced from the deuteron breakup process. The prescription for the (d,pn) reaction has already been proposed by Iseri $et\ al.$[8] and the code is now available. As our second step, we expect to clarify the importance of the d-breakup process in the Li(d,xn) reaction through the CDCC calculation with the nucleon OMPs obtained in the present work.

Acknowledgements

REFERENCES

[1] H. Matsui, in $Proceedings\ of\ the\ 23rd\ Symposium\ on\ Fusion\ Technology$, Venice, Italy, Sept. 20-24, 2004.
[2] S.P. Simakov, U. Fischer, V. Heinzel, and U. von Möllendorff, $Forschungszentrum\ Karlsruhe\ Report$ FZKA6743, (2002).
[3] S.P. Simakov, U. Fischer, U. von Möllendorff, I. Schmuck, A. Yu. Konobeev, Yu. A. Korovin, and P. Pereslavtsev, $J.\ Nucl.\ Mater.$, 307-311, 1710 (2002).
[4] U. Fischer, Y. Chen, S.P. Simakov, P.P.H. Wilson, P. Vladimirov, and F. Wasastjerna, $Fusion\ Eng.\ Des.$ 81,

1195 (2006).

[5] U. Fischer, M. Avrigeanu, P. Pereslavtsev, S.P. Simakov, and I. Schmuck, *J. Nucl. Mater.*, 367-370 1531 (2007).

[6] M. Hagiwara, T. Itoga, N. Kawata, N. Hirabayashi, T. Oishi, T. Yamauchi, M. Baba, M. Sugimoto, and T. Muroga, *Fusion Sci. Technol.*, 48, 1320 (2005).

[7] M. Yahiro, Y. Iseri, H. Kameyama, M. Kamimura, and M. Kawai, *Prog. Theor. Phys. Suppl.* 89, 32 (1986).

[8] Y. Iseri, M. Yahiro, and M. Kamimura, *Prog. Theor. Phys. Suppl.* 89, 84 (1986).

[9] K. Ogata, M. Yahiro, Y. Iseri, and M. Kamimura, *Phys. Rev. C* 67, 011602(R) (2003).

[10] A.J. Koning and J.P. Delaroche, *Nucl. Phys. A* 713, 231 (2003).

[11] R.L. Varner, W.J. Thompson, T.L. McAbee, E.J. Ludwig, and T.B. Clegg, *Phys. Rep.* 201, 57 (1991).

[12] P. Chau Huu-Tai, *Nucl. Phys. A* 773, 56 (2006).

[13] S. Chiba, K. Togasaki, M. Ibaraki, M. Baba, S. Matsuyama, N. Hirakawa, K. Shibata, O. Iwamoto, A.J. Koning, G. M. Hale, and M. B. Chadwick, *Phys. Rev. C* 58, 2205 (1998).

[14] J. P. Delaroche, Y. Wang and J. Rapaport, *Phys. Rev. C* 39, 391 (1989).

[15] J. Raynal, ECIS96 code, CEA Saclay Report No. CEA-N-2772 (1994); *Proceedings of the workshop on Applied Nuclear Theory and Nuclear Model Calculations for Nuclear Technology Applications*, Trieste, Italy, 506 (1988).

[16] J.H. Dave and C.R. Gould, *Phys. Rev. C* 28, 2212 (1983).

[17] B. A. Watson, P. P. Singh, and R. E. Segel, *Phys. Rev.* 182, 977 (1969).

[18] EXFOR/CSISRS DATABASE, http://www.nndc.bnl.gov/exfor/exfor00.htm.

[19] M. Avrigeanu, W. von Oertzen, U. Fischer, and V. Avrigeanua, *Nucl. Phys. A* 759, 327 (2005).

[20] Y. Iseri, M. Kamimura, M. Yahiro, Y. Sakuargi, K. Ogata, *Bulletin of Research Computer System, Computing and Communications Center of Kyushu University*, CDCDEU code, Vol.5, No.3, 117 (2006); HICADEU code, Vol.1, No.1, 16 (2007).

3.6 Developments of simulation model describing both elastic and inelastic scattering

Yoshinori Fukui, Hiroki Iwamoto, Yusuke Uozumi

Faculty of Engineering, Kyushu University

Motooka 744, Nishi-ku, Fukuoka 819-0395, Japan

yoshinori@nucl.kyushu-u.ac.jp

Nuclear reaction simulation models such as INC and QMD cannot calculate the nuclear elastic scatterings. Based on the stochastic quantization theory, we describe the wave motion of protons by Newtonian mechanics, and then incorporate elastic scatterings into the framework of the intranuclear cascade model. Numerical calculations were carried out and compared with experimental angular distributions of cross sections. Reasonable agreements have been demonstrated and verifying its high predictive ability and usefulness.

1.   Introduction

In recent days, the importance of nuclear reaction simulations is increasing. In particular an intermediate energy range covering from a few hundreds MeV to about 1 GeV. For instance, they are used for the particle radiation therapy, the astronautical engineering, the design of the spallation part of accelerator driven subcritical system (ADS), the particulate radiation transport and the radiation shielding for accelerator facilities and so on.

The intranuclear cascade (INC) model [1-4] is one of the most successful models and employed in many simulation tools such as PHITS [5], GEANT4 [6] and FLUKA [7]. This model covers the domain of classical collision regime that corresponds to inelastic reactions, but does not contain the nuclear elastic scattering. It is generally accepted that elastic scatterings must be described by the wave mechanics, and cannot be expressed from classical particle aspects. A new simulation approach must be developed which can describe inelastic and elastic processes simultaneously.

In the present work, we study a method in order to describe elastic scattering in the framework of one of the typical simulations, the INC model. We examine two methods for calculating elastic scattering. One is to use the classical potential and introduces the other. We incorporate above two methods into the INC model which is developed by our laboratory [8]. In order to check their applicability, we perform numerical calculations by means of two methods and results are compared with experimental data, respectively.

2. Theories

2. 1 Classical potential

A brief description is given of the method for calculating elastic scattering that uses a classical potential. First, we define temporal differential momentum of incident nucleon in terms of the nucleus potential gradient by the following equation:

$$\frac{d\vec{p}}{dt} = -\nabla U(r),$$

(1)

where $U(r)$ is potential of the Woods-Saxon type with the form of

$$U(r) = \frac{-V_0}{1 + \exp\left(\dfrac{r - R_{nucl}}{a_{nucl}}\right)}.$$

(2)

Parameters of V_0, R_{nucl} and a_{nucl} are potential depth, radius and diffuseness of the nucleus, respectively. Secondly, the trajectory displacement $dr(t)$ is described by

$$d\vec{r}(t) = \frac{\vec{p}(t)}{\sqrt{m^2 + |\vec{p}|^2}} dt + \frac{d\vec{p}(t)}{2\sqrt{m^2 + |\vec{p}|^2}} dt.$$

(3)

Where m is nucleon mass. At last, we assign eq.(1) to above equation. Therefore, we obtain the form of the trajectory displacement as

$$d\vec{r}(t) = \frac{\vec{p}(t)}{\sqrt{m^2 + |\vec{p}|^2}} dt - \frac{\nabla U(r)}{2\sqrt{m^2 + |\vec{p}|^2}} dt^2.$$

(4)

2. 2 Stochastic quantization

The procedure is the new technique of the stochastic quantization. This method is based on Nelson's stochastic mechanics [9], where wave functions are interpreted in terms of the probability distribution and the quantum motion is expressed by a Brownian like classical path. The theory is written by the stochastic differential equation:

$$d\vec{r}(t) = \vec{b}(\vec{r}(t),t)dt + \sqrt{\frac{\hbar}{2m}}d\vec{w}(t).$$

(5)

Where b is the mean forward velocity, and dw corresponds to quantum fluctuation of Wiener process. The mean forward velocity b is indicated by following equation:

$$\vec{b}(\vec{r}(t),t) = \mathrm{Re}\left[\frac{\hbar}{m}\nabla\ln\psi(r,t)\right] + \mathrm{Im}\left[\frac{\hbar}{m}\nabla\ln\psi(r,t)\right].$$

(6)

Here, the wave function $\psi(r,t)$ satisfies the Schrödinger equation under the condition of dw:

$$\left|d\vec{w}\right| = 0, \tag{7}$$

and

$$\left\langle d\vec{w}(t)d\vec{w}(t)\right\rangle = \frac{\hbar}{m}dt. \tag{8}$$

In the present work, we modify eq.(1) in order to simplify the calculation. Specifically, eq.(1) is modified to be

$$d\vec{r}(t) \rightarrow \left(\vec{b}' + \vec{\omega}'\right)\Delta t \equiv \vec{\zeta}\Delta t, \tag{9}$$

with

$$\vec{b}' = \frac{\vec{p}}{m}.$$

Where b' is the velocity of a particle defined by the conventional INC model. The vector field b and dw are approximated by new vectors b' and ω' in Ref.[10]. They are finally combined and replaced by ζ. The functional form of ζ includes the symmetric deflection angle dθ. And ζ is determined so as to reproduce experimental data. Additionally, dθ is given by the function ξ. It is a function of dθ, the wave number of incident proton k, the particle kinetic energy E and the target mass number A :

$$\xi(d\theta) = c\left\{\frac{kR^2}{2\sin(d\theta/2)}\right\}^2 \exp\left\{x_1 x_2\left(1 + \frac{x_1}{40}\right)\right\}, \tag{10}$$

with

$$c = 0.0000193E^{1.4} + 419.13E^{-1.521},$$

$$R = 0.14A^{1/3} + 0.122(A+1)/A,$$

$$x_1 = 2kR\sin(d\theta/2) \quad \text{and} \quad x_1 = 0.2(208/A).$$

The form of eq.(10) was introduced originally in Ref.[11] to simplify a form given in Ref.[12]. From a practical point of view, it is not worthwhile to reproduce detailed diffraction patterns in the angular distributions. Eventually, the trajectory displacement is described by the deflection angle which is decided by using nonuniform random number based on eq.(10).

3.   Results and discussion

Fig.1 shows angular distributions of the ^{40}Ca(p,p)^{40}Ca elasic scattering at 200 MeV and 500 MeV calculated by above two methods. Similarly, fig.2 shows results of the ^{208}Pb(p,p)^{208}Pb scattering. The solid line denotes the calculation result of introducing the stochastic quantization. The dashed line is the calculation result obtained by using the classical potential. And the closed circles denote the experimental

data cited from Refs.[12,13].

Fig.1 and fig.2 show that the method of using the classical potential cannot reproduce experimental data. In this method, the particle emission seems to be allowed in sole the most forward angles, and cannot be deflected to the larger angle region where experimental data exist. It is generally ascribed to the classical limit of the particle motion.
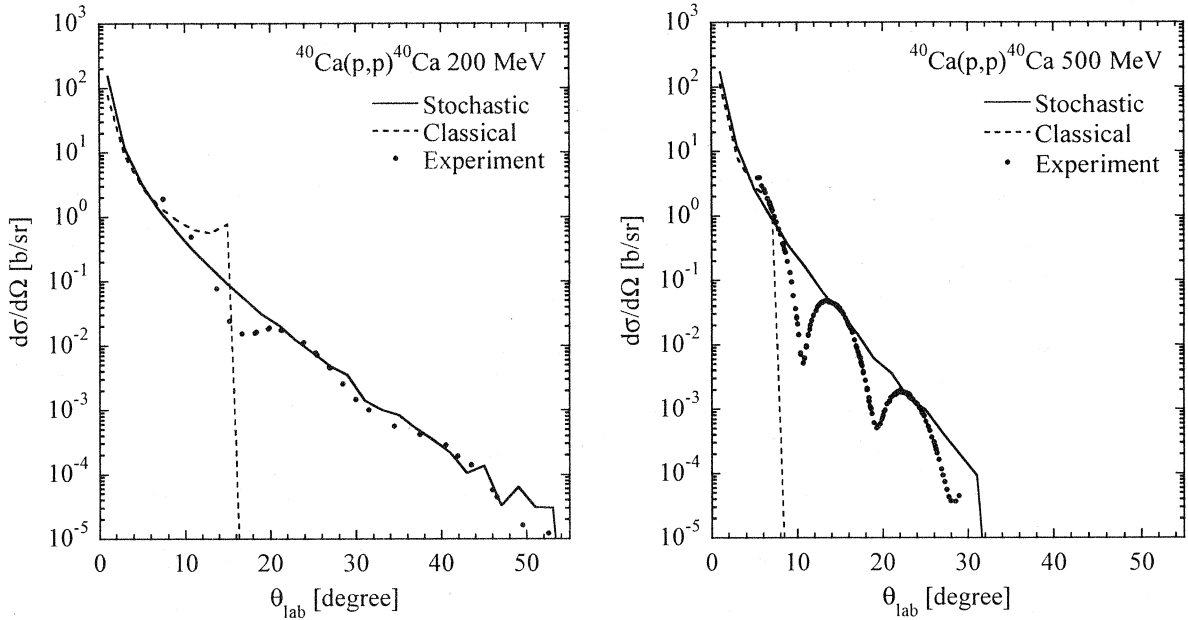

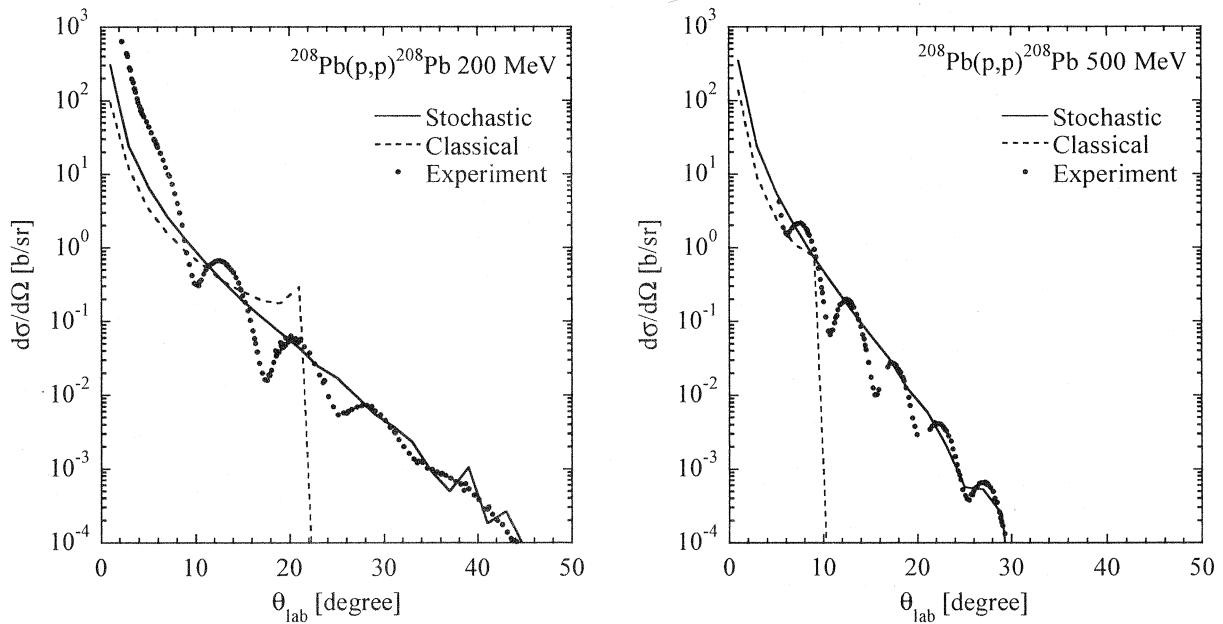Fig.1 Comparison between calculated and experimental [13,14] angular distributions of $^{40}Ca(p,p)^{40}Ca$ reaction at 200MeV and 500MeV.

Fig.2 Comparison between calculated and experimental [13,14] angular distributions of $^{208}Pb(p,p)^{208}Pb$ reaction at 200MeV and 500MeV.

The stochastic approach shows reasonable agreements with experiments in both the absolute values and the shape of angular distributions in fig.1 and fig.2. Since we introduced a simple prescription, diffraction patterns are not reproduced. From a theoretical point of view, this approach is unsatisfying and incorrect, since the mean forward velocity is disregarded and the particle path is no longer differentiable. Even so, essence of the stochastic mechanics is that the superposition of trajectories can justify the probability interpretation of the wave function. Since we have chosen trajectories to reproduce experimental data, the superposed trajectories can be considered to be close to the true one. Additionally, from an application point of view, in constant, this approach has positive aspects: it requires only simple calculations and appears to give reasonable physical results within the INC framework. To the best of our knowledge, it is the only finite order approach that consistently gives reasonable results for both elastic and inelastic processes.

4. Conclusion

We have proposed a new simulation model that incorporated the elastic scattering process into the INC model, which is widely used for nuclear reaction simulations. We examined two methods for calculating elastic scattering that uses the classical potential and the other introduces the stochastic quantization. The former has found to fail to reproduce deflection. In the latter, reasonable agreements were realigned although. For wider validity and reduce computational requirements, the exact theory was reduced to an empirical frame. Calculation results indicated that the stochastic approach is more useful than the classical potential approach. From the present work, it can be concluded that the stochastic approach has positive aspects for applications.

From the theoretical point of view, the success of stochastic approach is very interesting result. The model offers a method to describe elastic and inelastic reactions simultaneously. Elastic scattering is governed by wave effects, while inelastic reactions have a classical point-like particle nature. This approach is the first to combine two phenomena from different physical pictures.

Our further study will be directed toward testing its applicability to other regimes and performing calculations of recoil momentum of residual nuclei.

Reference

[1] R. Serber, "Nuclear reactions at high energies ", Phys. Rev. **72**, 1114-1115 (1947).

[2] M. L. Goldberger, "The interaction of high energy neutrons and heavy nuclei", Phys. Rev. **74**, 1269-1277 (1948).

[3] T. Kin et al., "Proton production cross sections for reactions 300- and 392- MeV protons on carbon, aluminum, and niobium", Phys. Rev. C **72**, 014606, 1-9 (2005).

[4] H. Duarte, "Particle production in nucleon induced reactions above 14MeV with an intranuclear cascade model", Phys. Rev. C **75**, 024611, 1-26 (2007), and References therein.

[5] K. Niita et al., "PHITS—a particle and heavy ion transport code system", Radiation Measurements, **41**,

1080-1090 (2006).

[6] J. Allison, et al., "Geant4 developments and applications", IEEE Transactions on Nucl. Sci. **53**, 270-278 (2006).

[7] A. Fassó, A. Ferrari, J. Ranft, P. R. Sala, "New developments in FLUKA modeling of hadronic EM interactions", Porc. of SARE-3, KEK report proceedings 1997, 32-43 (1997).

[8] H. Iwamoto, Y. Uozumi, M. Nakano, "INC", Proc. of the International Conference on the Soft Computing and Human Science 2007, Kitakyushu, 145-152 (2007).

[9] E. Nelson, "Derivation of the Schrödinger equation from Newtonian mechanics", Phys. Rev. **150** [4], 1079-1085 (1966).

[10] Y. Uozumi, Y. Fukui, H. Iwamoto, M. Nakano, "Stochastic approach to proton nucleus elastic scattering", Proc. of the International Conference on the Soft Computing and Human Science 2007, Kitakyushu, 139-144 (2007).

[11] H. Yoshida et al., "Absolute efficiency of stacked GSO(Ce) spectrometer for inter-mediate energy protons", Nucl. Instrum. And Meth. A **411**, 46-50 (1998).

[12] S. Pearlstein, "Medium energy nuclear data libraries", Jonr. Astrophys. **346**, 1049 (1989).

[13] D. A. Hutcheon et al., "The elastic scattering of intermediate energy protons from ^{40}Ca and ^{208}Pb", Nucl. Phys. A **483**, 429-460 (1988).

[14] G. W. Hoffmann et al., "Elastic scattering of 500- MeV polarized protons from 40,48Ca, 90Zr, and 208Pb, and breakdown of impulse approximation at small momentum transfer", Phys. Rev. Lett. 47, 1436-1440 (1981).

[14] Y. Uozumi, Y. Fukui, H. Iwamoto, M. Nakano, "Stochastic approach to proton nucleus elastic scattering", Proc. of the International Conference on the Soft Computing and Human Science 2007, Kitakyushu, 139-144 (2007).

3.7 Paramagnetic Scattering of Neutrons by Rare-Earth Oxides*

Toru Murata* and Tsuneo Nakagawa**
*Former NAIG Nuclear Research Lab.
**Nuclear Data Center, Japan Atomic Energy Agency

Thermal region neutrons are scattered by the paramagnetic moment of rare-earth oxides such as Gd_2O_3 which are contained in nuclear fuels as burnable poison. The scattering is atomic process and not a nuclear process, so the data are not included in the nuclear data files such as ENDF/B and JENDL. The cross sections and angular distributions of the elastic scattering are calculated using the existing theory and ENDF/B type files are made for oxides of Ce, Pr, Nd, Sm, Eu, Gd, Tb, Dy, Ho, Er, Tm and Yb. in the incident neutron energy range from 10^{-5} to 1.0 eV at the room temperature and the temperature dependences in the paramagnetic region are also given.

1. Introduction

Most rare-earth oxides have paramagnetic moment of its ionized states. Neutrons have magnetic moment and interact with the paramagnetic moment of the ions and scattered when they impinge upon the oxides. The paramagnetic scattering is an atomic process and not included in the nuclear data files such as the ENDF/B and JENDL. In the present work, cross sections and angular distributions of the paramagnetic elastic scattering of 3^+ states of 11 elements; Ce, Pr, Nd, Sm, Gd, Tb, Dy, Ho, Er, Tm and Yb, and 2+ state of Eu were calculated based on the theory described in the papers[1],[2],[3]. For these ions, paramagnetic properties are determined by the 4f electron numbers.

2. Theory

The interaction of neutron magnetic moment and the atomic electrons is given by

$$H_{int} = -\int \vec{\mu}_n \cdot \mathbb{H}(\vec{r} - \vec{r}_n)dr , \tag{1}$$

where $\vec{\mu}_n = \gamma \mu_N \vec{\sigma}$ is the magnetic moment of neutron, $\gamma = -1.913$, $\vec{\sigma}$ neutron spin operator,

and $\mathbb{H}(\vec{r} - \vec{r}_n)$ is the magnetic fields at neutron position $\vec{r}_n$ caused by the charge density and current density of the moving bound electrons at $\vec{r}$. The paramagnetic properties of the rare-earth oxides are well described by the states of unpaired 4f electrons and the integration in Eq. (1) is also made for the states.

Then the paramagnetic elastic scattering differential cross section is given by

$$\frac{d\sigma_{pm}}{d\Omega} = \frac{k_f}{k_i}\left|\left\langle f \left| H_{int} \right| i \right\rangle\right|^2 \approx \frac{1}{6}\left(\frac{e^2}{mc^2}\right)^2 \gamma^2 \mu^2 f(K)^2 , \tag{2}$$

---

and the elastic scattering cross section is given by

$$\sigma_{pm}(K) = \frac{2}{3}\pi\left(\frac{e^2}{mc^2}\right)^2 \gamma^2 \mu^2 \left\langle f(K)^2 \right\rangle \quad , \qquad (3)$$

where $\vec{K} = \vec{K}_f - \vec{K}_i$ is the momentum change between incident and scattered neutrons, e^2/mc^2 is the classical electronic radius, γ and μ are the magnetic moments of neutron and of the ions, respectively, $f(K)$ the magnetic form factor and $\left\langle f(K)^2 \right\rangle$ average of the squared magnetic form factor over all scattering angles. So, the relationship between scattering angle θ and the momentum change K is K = $2K_i \sin(\theta/2)$.

The magnetic form factor $f(K)$ is given by Blume et al.[2] for the atomic ions of ground state configuration of (S, L, J) in the LS coupling as

$$f(K) = \frac{\vec{L}\cdot\vec{J}\left\langle g_0(K) - g_2(K)/2 \right\rangle + 2\vec{S}\cdot\vec{J}\left\langle j_0(K) \right\rangle}{\vec{L}\cdot\vec{J} + 2\vec{S}\cdot\vec{J}} \qquad (4)$$

Blume et al.[2] tabulated the functions $\left\langle g_0(K) - g_2(K)/2 \right\rangle$ and $\left\langle j_0(K) \right\rangle$ defined as

$$\left\langle j_L(K) \right\rangle = \int_0^\infty R_{4f}^{\;2}(r)\cdot j_L(Kr)dr$$

$$\left\langle g_L(K) \right\rangle = \int_0^\infty R_{4f}^{\;2}(r)\cdot g_L(Kr)dr , \qquad (5)$$

where $j_L(Kr)$ is the usual spherical Bessel function, $g_L(Kr)$ the function defined by Trammell[1] and $R_{4f}(r)$ the radial part of the 4f electron wave function obtained with the Hartree-Fock method.

3. Calculation

Blume et al.[2] tabulated the function values in the momentum transfer range $K/4\pi = 0 \sim 1.3/\text{Å}$ for the 3+ ions of Ce, Pr, Nd, Sm, Gd, Dy, Er and Yb. For Eu, 3+ ion has J=0 and no magnetic moment, and the values of 2+ ion were given. The function values change rather smoothly over these elements. In the present calculation, the values were interpolated for the 3+ ions of Tb, Ho and Tm using the values of the neighbor ions.

Table 1 shows electronic configurations, ground state (S, L, J) values and paramagnetic moments of rare-earth 3+ ions at room temperature. Most of calculated paramagnetic moments of these ions agree with the experimental values, and the ground state (S, L, J) values are predicted properly by the Hund rule. For Sm and Eu, it is well known that the excited states lie near the ground state and thermally excited, so the simple Landé factor can not explain the experimental data, which are reproduced well with the theory by Van-Vleck[5]. Present calculations were made with Eqs. (2), (3) and (4) using the experimental magnetic moments. Paramagnetic moments tabulated in Table 1 are those at room temperature T₀ (300

°K) and those at higher temperature T (°K) are predicted by

$$\mu(T) = \mu(T_0) \cdot \chi(T) / \chi(T_0), \tag{6}$$

where $\chi(T)$ is the paramagnetic susceptibility at T and given by[6]

$$\chi(T) = \sum_J (2J+1)\exp(-E_J/kT)\left\{\frac{g_J^{\;2}\mu_B^{\;2}}{3kT}J(J+1)+\alpha_J\right\} \Bigg/ \sum_J (2J+1)\exp(-E_J/kT) \tag{7}$$

where g_J is the Landé g factor for total spin J, μ_B the Bohr magneton and E_J the atomic excitation energies caused by the ground state L · S coupling with the strength λ given in the last column of Table 1;

$$E_J = \lambda\{J(J+1)-L(L+1)-S(S+1)\}/2, \quad \text{J=L+S,...,|L-S|}, \tag{8}$$

and α_J is the constant susceptibility defined by Van Vleck[5] and approximately;

$$\alpha_J = \frac{\mu_B^{\;2}}{6(2J+1)}\left\{\frac{F(J+1)}{E_{J+1}-E_J} - \frac{F(J)}{E_J - E_{J-1}}\right\}, \tag{9}$$

where

$$F(J) = \left[(S+L+1)^2 - J^2\right] \cdot \left[J^2 - (S-L)^2\right]/J \tag{10}$$

With these formula, temperature dependence of the paramagnetic scattering were calculated in the temperature range from 300 to 2000 °K and showed approximately $(T_0/T)^2$ dependence for most elements but Sm.

4. Results and Discussion

Examples of the calculated cross sections and differential cross sections are shown in Fig.1 and Fig.2, respectively, comparing with the experimental data, if available. For thermal neutron (En=25.3 meV) cross sections, comparison is made in Fig. 1 with the referred cross sections in Mughabghab's book[7]. Though good agreement is shown in the figure between them, for some elements such as Ho and Tm, discrepancies are recognized. That will be originated in the differences of magnetic moments. Present calculations were made in the incident neutron energy range up to En=1.0 eV, however, above 0.1 eV, extrapolation was made in the magnetic form factors given by Blume et al.[2] and there will be great ambiguity in the region. Table 2 compares the thermal cross sections of nuclear scattering and magnetic scattering of rare-earth oxides at 300 °K. Uncertainty of the calculations is also caused by the error of experimental magnetic moments. The errors are not given in the handbook[4], so the cross section errors can not be estimated. Calculated examples of the temperature dependence of paramagnetic susceptibilities are shown in Fig.3. Numerical values of the temperature dependence of the cross sections are also given in the present data file. Except Sm, magnetic scattering cross section decreases with the temperature as is shown in the left

part of Fig.3, and there will be little effect in the power reactors, however, in the room temperature experiment of the critical assembly which include such as Gd_2O_3, the influence of the magnetic scattering should be examined.

Thanks are due to the other members of the FP working group of JNDC for useful discussion.

References

1) G. T. Trammell, Phys. Rev. 92, 1387 (1953)
2) M. Blume et al., J. Chem. Phys. 37, 1245 (1962)
3) C. Stassis and W. Deckman., Phys. Rev. B12,1885 (1975)
4) "Handbook of Chemistry and Physics (88th ed.2007-2008)", CRC press
5) J. H. Van Vleck: "The theory of electric and magnetic susceptibilities" Clarendon Press, Oxford, 1932
6) T. Nagamiya and R. Kubo edited "Solid State Physics (2nd ed.)" published by Iwanami, 1966, chapter 3 by T. Nagamiya. [in Japanese]
7) S. F. Mughabghab et al. "Neutron Cross Sections vol.1, part A", Academic Press (1981)
8) W. C. Koehler, E. G. Wollan, Phys.Rev.92,1380 (1953)
9) W. C. Koehler et al., Phys. Rev. 110,37 (1958)

Table 1 Electronic configuration and magnetic moment of rare-earth oxide ions. (Mainly from ref.4)

Elements	Configuration	G.State (S,L,J)*1	Mag.moment (calc.)*2	Mag.moment (exp)	L·S strength λ(meV)
Ce3+	$4f^15s^2p^6$	$^2F_{5/2}$ (1/2, 3, 5/2)	2.54	2.52	79
Pr3+	$4f^25s^2p^6$	$^3H_4$ (1, 5, 4)	3.58	3.56	45
Nd3+	$4f^35s^2p^6$	$^4I_{9/2}$ (3/2, 6, 9/2)	3.62	3.45	36
Pm3+	$4f^45s^2p^6$	$^5I_4$ (2, 6, 4)	3.68	—	32
Sm3+	$4f^55s^2p^6$	$^6H_{5/2}$ (5/2, 5, 5/2)	0.85	1.74	30
(Eu3+)	$4f^65s^2p^6$	$^7F_0$ (3, 3, 0)	0	3.4*3	29
Eu2+	$4f^75s^2p^65d^0$	$^8S_{7/2}$ (7/2, 0, 7/2)	7.94	3.4*3	NDG*4
Gd3+	$4f^75s^2p^6$	$^8S_{7/2}$ (7/2, 0, 7/2)	7.94	7.98	NDG*4
Tb3+	$4f^85s^2p^6$	$^7F_6$ (3, 3, 6)	9.72	9.77	−36
Dy3+	$4f^95s^2p^6$	$^6H_{15/2}$ (5/2, 5, 15/2)	10.64	10.83	−47
Ho3+	$4f^{10}5s^2p^6$	$^5I_8$ (2,6, 8)	10.6	11.2	−64
Er3+	$4f^{11}5s^2p^6$	$^4I_{15/2}$ (3/2,6,15/2)	9.58	9.9	−102
Tm3+	$4f^{12}5s^2p^6$	$^3H_6$ (1, 5, 6)	7.56	7.61	−160
Yb3+	$4f^{13}5s^2p^6$	$^2F_{7/2}$ (1/2, 3, 7/2)	4.54	4.5	−365

*1 Hund's rule

*2 $\mu(theory)= g \cdot [J(J+1)]^{1/2}$

　　　Lande g-factor: $g=1+[J(J+1)+S(S+1)-L(L+1)]/2J(J+1)$

*3 C.Kittel, "Introduction to Solid State Physics(8th ed.)", John Wiley

*4 No data given

Oxides	Cross Section (b)	
	Nuclear*	Magnetic**
Ce_2O_3	3.397	1.572
Pr_2O_3	3.361	3.604
Nd_2O_3	8.735	3.924
Sm_2O_3	13.70	3.668
EuO	5.421	1.898
Gd_2O_3	70.21	11.84
Tb_2O_3	10.69	21.13
Dy_2O_3	not given	28.64
Ho_2O_3	not given	32.76
Er_2O_3	5.885	27.16
Tm_2O_3	not given	16.62
Yb_2O_3	not given	6.028

Table 2   Nuclear and magnetic scattering cross sections of rear-earth oxides.
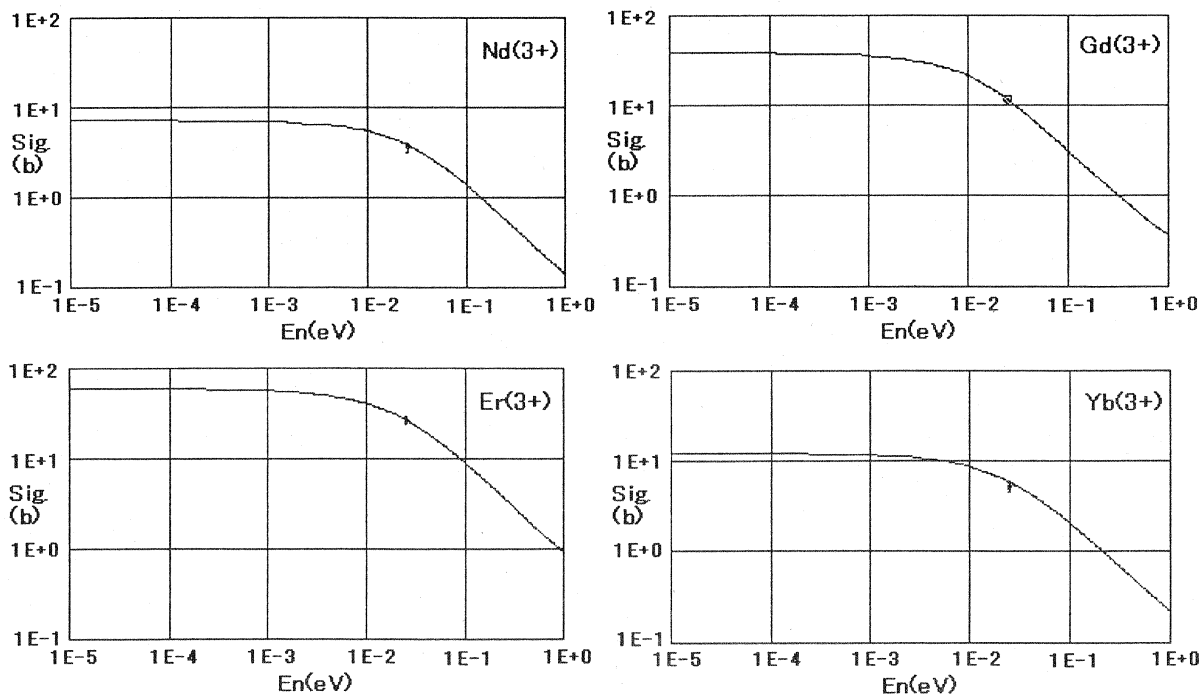* JENDL-3.3 (T=300°K)
** Present calculation:

Fig.1   Examples of the paramagnetic neutron scattering cross sections. Solid line is the results of the present calculation. Dots at En=25.3 meV are the experimental data for Nd, Er and Yb, and calculated result for Gd referred in Mughabghab's book[7] .
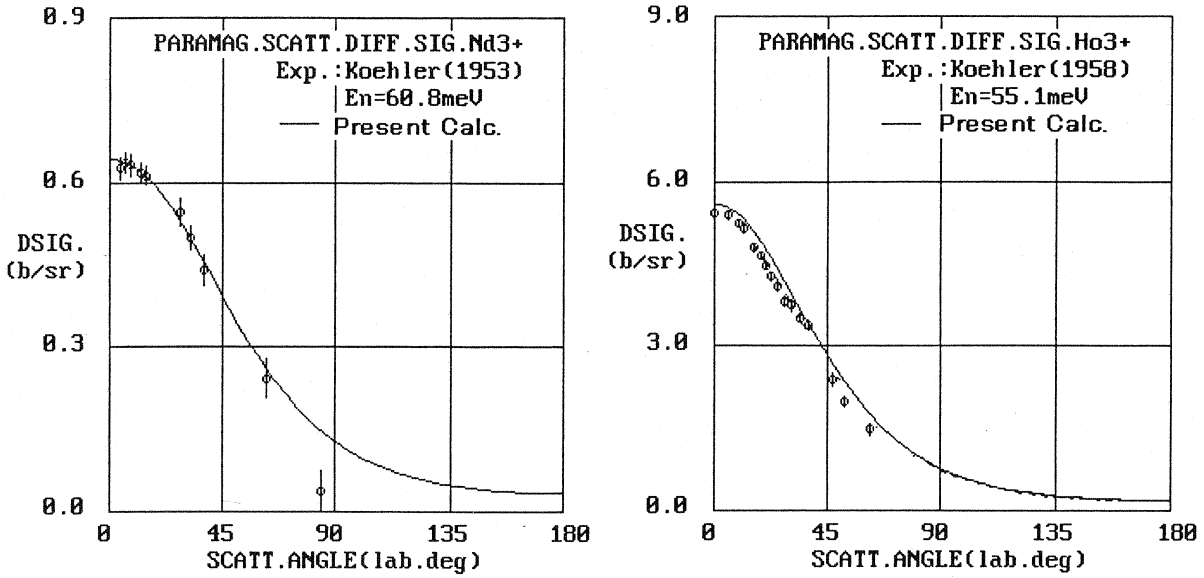
Fig.2   Examples of differential cross section of paramagnetic neutron scattering (Left: Nd2O3, Right: Ho2O3). Experimental data are measured by Koehler et al.[8),9)], present calculation is shown in solid line.
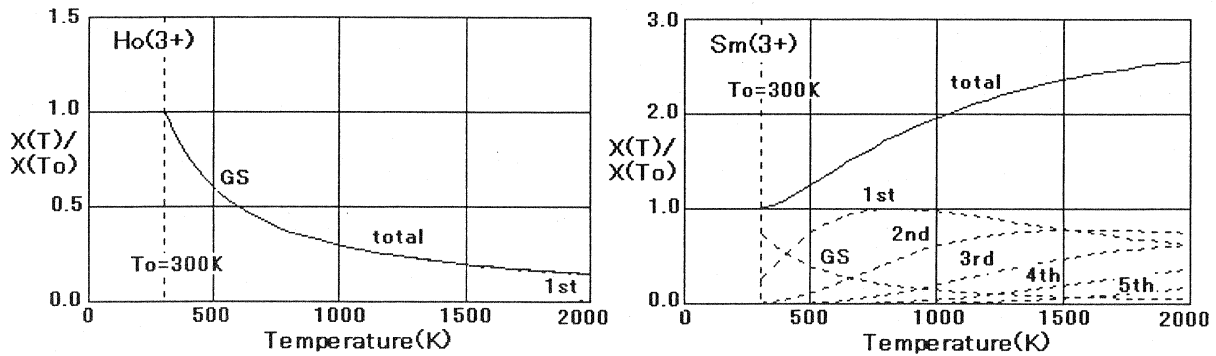
Fig.3   Calculated temperature dependence of the paramagnetic susceptibility of Ho3+ (left) and Sm3+ (right) above 300°K. The ordinate shows the ratio of susceptibility of temperature T to that of the room temperature 300°K. Almost rare earth elements but Sm show the tendency to decrease with the increase of temperature like Ho case. Sm has seven narrow spacing excited states of the ground state L·S multiplet and these states excited by thermal energies and the susceptibility increases with temperature. The dashed lines show the details of the susceptibilities with excited levels.

3.8 Impact of Cross Section Library Update from ENDF/B-VI.8 to ENDF/B-VII.0 on BWR Fuel Lattice Burnup Characteristics

Akiko Toishigawa, Tadashi Ikehara, Munenari Yamamoto, Hiromi Maruyama
Global Nuclear Fuel – Japan Co., Ltd.
3-1, Uchikawa 2-Chome, Yokosuka-Shi, Kanagawa-Ken 239-0836
E-mail: Akiko.Toishigawa@gnf.com

ENDF/B-VII.0 was released December 2006. We investigated the impact of cross section library update from ENDF/B-VI.8 to ENDF/B-VII.0 on BWR fuel lattice burnup characteristics. In the case of UO_2 fuel lattice with Gd rods, the difference in K_{inf} between the two libraries varies ±0.4%dk along exposure. Major contributors to this difference were identified, namely the update of U-238, Pu-241, O-16 and H-1 (bound in H_2O) data.

1. Introduction

ENDF/B-VII.0 was released December 2006. Many benchmark tests have been done with the new library against critical experiments to examine its predictability of criticality, showing the better results relative to those with the older ENDF/B versions. In the results for LEU benchmarks of the ICSBEP, for example, the average difference in C/E of criticality factor between ENDF/B-VI.8 and VII.0 library was reported to be 469pcm[1]. Note that this was obtained from a series of cold, clean critical experiments. It is expected, therefore, that the situations are different in an actual heterogeneous, hot, operating condition. The influence of the library update on LWR fuel burnup characteristics is worth evaluating, while no such investigations have been reported. Then, we investigated the reactivity impact of cross section library update from ENDF/B-VI.8 to ENDF/B-VII.0 on BWR fuel lattice burnup characteristics.

2. Calculational codes and cross-section library

Investigation has been done using three different codes, i.e. Monteburns2[2], MVP-BURN[3] and LANCER01[4]. Monteburns2 is a fully automated tool that links the continuous energy Monte Carlo code MCNP with the burnup code ORIGEN2. We have enhanced Monteburns2 to remove the limitation on the number of burnup materials and of burnup steps. MVP-BURN is also a tool that links the continuous energy Monte Carlo code MVP with the burnup module BURN. LANCER01 is the multi-group transport-theory based BWR lattice physics code developed by GNF.

NJOY99.161[5] was used for generating both MCNP and LANCER01 cross-section libraries based on ENDF/B-VI.8 and ENDF/B-VII.0. MCNP library was prepared for Monteburns2. This library consists of 246 nuclides including 120 FP nuclides having sensible worth in reactivity. LANCER01 library consists of 225 nuclides in the form of 190 neutron energy group structure.

On the other hand, cross-section library for MVP-BURN was generated by JAEA's LICEM system[6] which is entirely independent of NJOY system. The BURN module has several choices of burnup chain models: we chosen a detailed burnup chain model comprising 21 heavy nuclides and 104 FP nuclides.

3. Reactivity impact of cross section library update

3.1. Burnup calculation of 4x4 fuel rod lattice with 2 adjacent Gd-poisoned rods (NEACRP/L-271 benchmark problem)[7]

The NEACRP/L-271 burnup benchmark problem was taken as the first case to

evaluate the reactivity impact of the cross section library update on LWR fuel burnup characteristics. Two separate burnup calculations with use of the two different library versions (ENDF/B-VI.8 and VII.0) were performed by each of the aforementioned three codes. In addition, one more MVP-BURN calculation with use of JENDL-3.3 library was made to compare with the results of ENDF/B-VI.8. We obtained ΔK_{inf} due to cross section library update by taking the difference of K_{inf} between each pair of the corresponding burnup calculations. The resultant ΔK_{inf} are plotted in Fig.1, showing that the reactivity impact of updating the cross section library from ENDF/B-VI.8 to VII.0 is considerable and varies with exposure ranging over $\pm 0.4\%dK$. It should be noted that all three methods yielded almost consistent results of ΔK_{inf} both in trend and magnitude over the exposure range of interest. This indicates that the deterministic LANCER01 calculation is reliable for the current purpose: a time-consuming Monte Carlo calculation is not always necessary. It is interesting to notice, in addition, that the results of JENDL-3.3 are fairly close to those of ENDF/B-VI.8.

3.2. Reactivity impact of cross section library update on burnup characteristics of BWR fuel lattice

A pair of LANCER01 burnup calculations with use of two different cross section libraries (ENDF/B-VI.8 and VII.0) were performed for the following three cases of BWR fuel assembly.

Case-1: 9x9 BWR UO$_2$ fuel rod lattice with 16 Gd-poisoned rods[8]
Case-2: 9x9 BWR UO$_2$ fuel rod lattice with no Gd-poisoned rod
Case-3: 10x10 BWR MOX fuel rod lattice with 14 Gd-poisoned rods[8]

Case-1 is the case known as "LWR Next Generation Benchmark Problem". Case-2 is a typical STEP-III BWR assembly with the average enrichment of 4.3wt%, while all the Gd-poisoned rods are intentionally set to be Gd free to remove the effect caused by Gd nuclides. Case-3 intends to see the effect of changing fuel material from UO$_2$ to MOX.

The results of reactivity impact by cross section library update are shown in Fig.2 for the Case-1, Fig.3 for the Case-2 and Fig.4 for the Case-3, respectively. It should be noted that the results are significantly different among the three, and that the exposure dependent behavior of Case-1 looks similar to that shown in the NEACRP/L-271 problem. This implies that the effect of library update would be produced by several exposure-dependent components. It is also worth investigating to identify the cause of the variations among the cases.
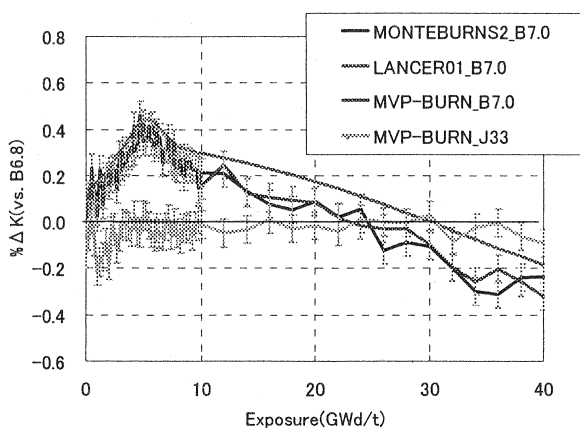

Fig.1 Difference in K_{inf} by library update from ENDF/B-VI.8 to B-VII.0 or JENDL-3.3 (NEACRP/L-271 Problem)
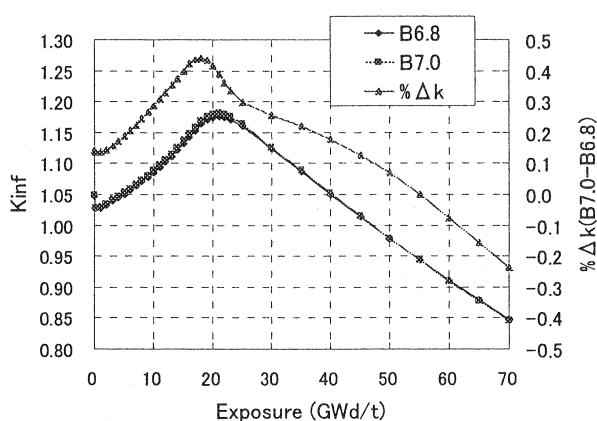
Fig.2 Difference in K_{inf} by library update from ENDF/B-VI.8 to BVII.0 (Case-1)
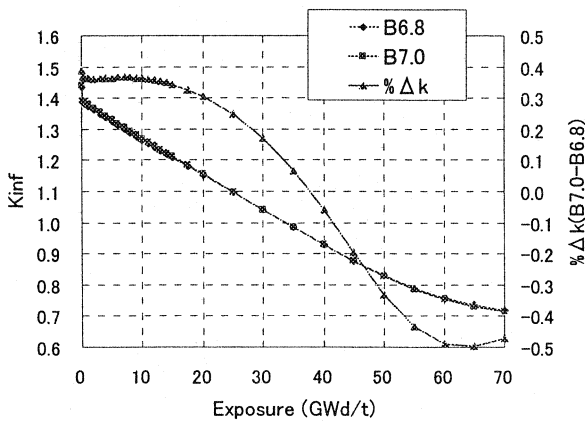
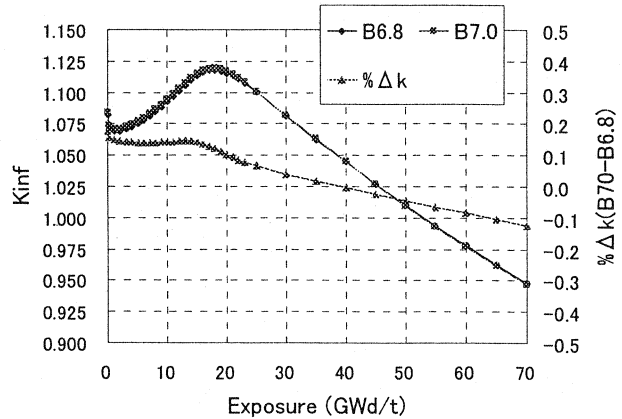Fig.3 Difference in K_{inf} by library update from ENDF/B-VI.8 to B-VII.0 (Case-2)

Fig.4 Difference in K_{inf} by library update from ENDF/B-VI.8 to B-VII.0 (Case-3)

4. Sensitivity study of cross-section data update of individual nuclides

To look into the main causes of producing the behavior along exposure shown in the previous section, we made additional LANCER01 burnup calculations for the NEACRP/L-271 problem: sensitivities on K_{inf} were obtained by replacing ENDF/B-VII.0 cross section data with ENDF/B-VI.8 data individually for those nuclides which are the major players in LWR analysis. As a result, four major contributors to the differences were identified, namely the update of U-238 capture cross section, Pu-241 capture cross section, O-16 (n, α) cross section and H-1 (bound in H_2O) thermal scattering kernel. Fig.5 shows the results of sensitivities on K_{inf} for each of the above four contributors together with their summation. This plot reveals that the summation of the four contributors reproduces fairly well the K_{inf} difference between ENDF/B-VI.8 and B-VII.0 shown in Fig.1. Particularly, the H-1 contribution is notable, because it evidently produces an effect on Gd worth during the period of its depletion.

To physically interpret the effect created by each contributor, we made a comparison of LANCER01's multi-group cross section data between ENDF/B-VI.8 and B-VII.0 as shown in Figs.6 through 9. Each plot also contains the ratio of ENDF/B-VII.0 data to B-VI.8 for clarity of comparison.

4.1. U-238

The reactivity effect of U-238 update from EBDF/B-VI.8 to B-VII.0 is significant and has a large variation along exposure as shown in Fig.5. In Fig.6, a comparison of U-238 capture cross sections between the two libraries is given, showing that it decreased in value of 1% to 2% over a low energy range. Then, this update brings positive reactivity during a low exposure period, and turns negative at high exposure due to the reduced production of Pu-239.

4.2. Pu-241

In ENDF/B-VII.0, Pu-241 thermal capture cross section increased in value as shown in Fig.7. Then, this update brings negative reactivity, since Pu-241 increases in number density with exposure in a UO_2 fuelled lattice.

4.3. O-16

In ENDF/B-VII.0, O-16 (n, α) cross-section decreases in value about 30% as shown in Fig.8. This update brings constant reactivity of +0.15%dK over an entire range of exposure.

4.4. H-1 (in H₂O)

In ENDF/B-VII.0, H-1 (bound in H_2O) thermal scattering cross section was changed

as shown in Fig.9. This update produced exposure-dependent differences in reactivity as shown in Fig.5 for the NEACRP/L-271 problem. A steep gradient in reactivity curve seen in an early burnup period is created by a sensitive nature of Gd depletion mechanism. Therefore, the reactivity effect of this H-1 update may change with the Gd-related conditions. This can be examined by looking at the results obtained for Case-1, 2 and 3 as shown in Fig.10. In Case-1 (9x9 BWR UO$_2$ fuel rod lattice with 16 Gd-poisoned rods), the reactivity effect starts with negative contribution at the beginning of fuel exposure: once Gd capture was overly calculated, the Gd depletion rate becomes faster and faster due to the positive feedback mechanism of Gd depletion, resulting in the behavior seen in Fig.10. After Gd burns out, the reactivity effect becomes close to that of Case-2. In Case-3 (10x10 BWR MOX fuel rod lattice with 14 Gd-poisoned rods), on one hand, the reactivity effect of the H-1 update looks much different from the previous Case-1. This is due to two factors, i.e. one is that thermal spectrum in MOX lattice is much harder than that of UO$_2$, and another the presence of Pu thermal resonance around 0.3eV depresses thermal spectrum sensitive to Gd capture.
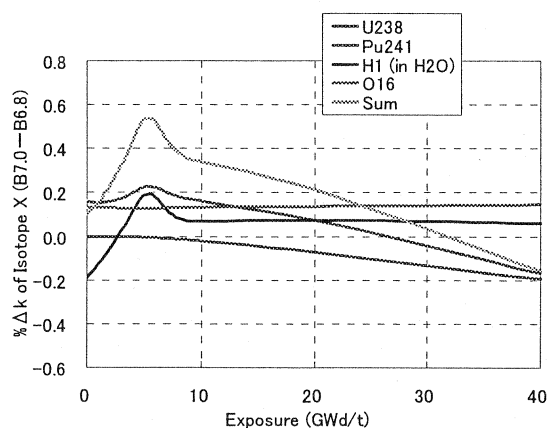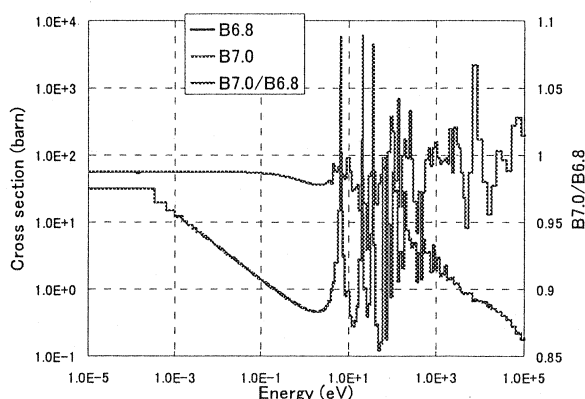
Fig.5 Reactivity of nuclide data update

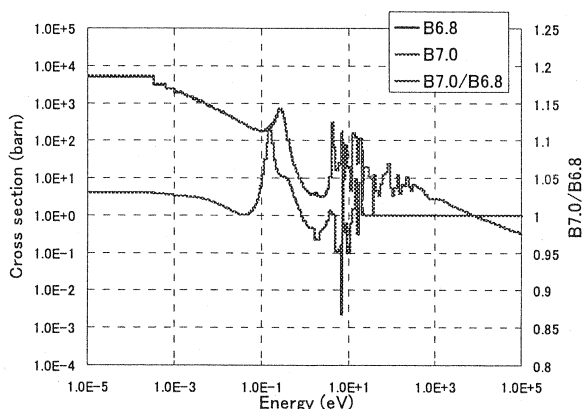Fig.6 U-238 capture cross-section update

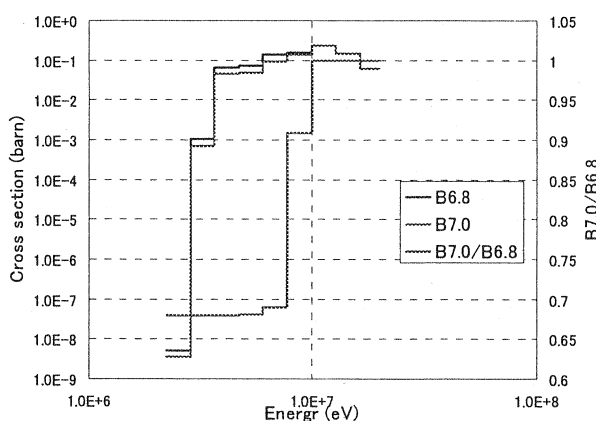Fig.7 Pu-241 capture cross-section update

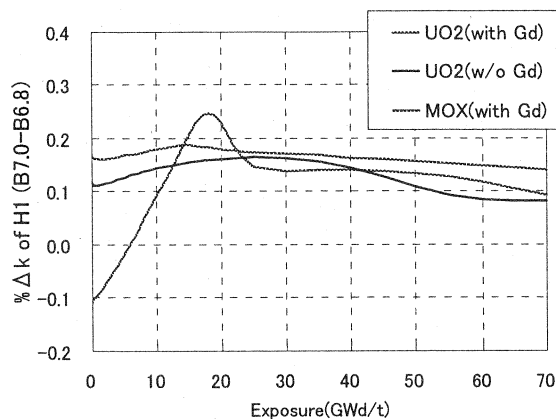Fig.8 O-16 (n, α) cross-section update
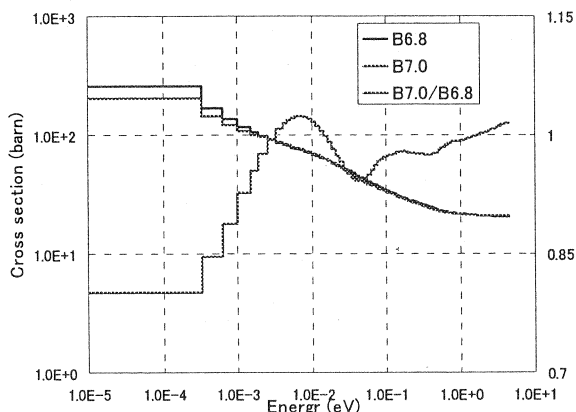
Fig.9 H-1(in H₂O) scattering cross-section update   Fig.10 Reactivity of H-1(in H₂O) data update

5. Conclusion

The impact of cross section library update from ENDF/B-VI.8 to B-VII.0 on BWR fuel burnup characteristics was investigated. The degree of impact is significant and varies with fuel compositions and/or Gd presence. Major contributors to the K_{inf} difference between the two libraries are the decrease of U-238 capture cross-section, the increase of Pu-241 capture cross-section, the decrease of O-16 (n, α) cross-section and the change of H-1 (bound in H₂O) thermal scattering kernel. It is suggested, when adopting the new cross-section library in the design and analysis of LWR core, that the benchmark calculations only for the clean conditions is insufficient, and that evaluation of the impact on burnup characteristics is also important.

Reference

[1] Steven C. van der Marck, Benchmarking ENDF/B-VII.0, Nuclear Data Sheets 107 (2006) 3061-3118
[2] RSICC Peripheral Science RUTINE COLLECTION, MONTEBURNS2.0, An automated Multi-Step Monte Carlo Burnup Code System. Los Alamos National Laboratory, PSR-455 MONTEBURNS2.0
[3] K. Okumura, *et. al.,* Validation of a Continuous-Energy Monte Carlo Burn-up Code MVP-BURN and Its Application to Analysis of Post Irradiation Experiment, JNST, 37, 128 (2000)
[4] K. Azekura, *et. al.,* Development of a BWR Lattice Analysis Code LANCER Based on an Improved CCCP Method, ANFM2003
[5] R.E. Mac Farlane, *et. al.,* RSICC Peripheral Shielding Routine Collection NJOY99.0, LANL, PSR-480 NJOY99.0
[6] T. Mori, *et. al.,* Neutron Cross Section Library Production Code System for Continuous Energy Monte Carlo Code MVP LICEM, JAERI-Data/Code 96-08 (1996) [in Japanese]
[7] C. Maeder, *et. al.,* International Comparison Calculations for a BWR Lattice with Adjacent Gadolinium Pins, NEACRP-L-271 (1984)
[8] A. Yamamoto, *et. al.,* Benchmark Problem Suite for Reactor Physics Study of LWR Next Generation Fuels, JNST, Vol.39, No8, p.900-912 (2002)

3.9 Analysis of irradiated UO2 and MOX fuel composition data measured in REBUS program

Yoshihira ANDO[1]*, Toru YAMAMOTO[1], Yamato HAYASHI[2]

1) Reactor Core and Fuel Reliability Group, Safety Standard Division

Japan Nuclear Energy Safety Organization (JNES)

TOKYU REIT Toranomon Bldg. 7F, 3-17-1, Toranomon, Minato-ku, Tokyo 105-0001, Japan

2) Nuclear Core & Plant Engineering Group, System Design & Engineering Department

Isogo Nuclear Engineering Center

Toshiba Corporation, 8 Shinsugita-cho, Isogo-ku Yokohama 235-8523, Japan

*E-mail: ando-yoshihira@jnes.go.jp

Japan Nuclear Energy Safety Organization (JNES) participated in REBUS international program organized by Belgonucleaire and SCK/CEN and has been analyzing the experimental data. This paper presents preliminary analysis results obtained using SRAC and MVP-BURN codes with the nuclear library JENDL-3.2 for the measured isotope composition data of the UO2 and the MOX fuels that were irradiated in commercial LWR plants and used in critical experiments in the VENUS critical facility of SCK/CEN.

1. Introduction

Critical experiments of the cores partially including irradiated UO2 and MOX fuels were performed in REBUS international program.[1] Burnup calculations of the irradiated fuels were performed to determine the fuel compositions in the analyses of the critical experiments. The irradiated fuels were selected from MOX fuel assemblies irradiated in the BR3 PWR plant (BR3-MOX), 9x9 MOX fuel assemblies irradiated in the Gundremmingen BWR plant (GUN-MOX) and a 18x18 UO2 fuel assembly irradiated in the GKN-II PWR plant (GKN-UO2). One sample were taken for each fuel type and isotopic compositions were measured by a chemical assay at a hot laboratory in SCK/CEN.

We have been studying analysis methods including nuclear data libraries through comparisons between the calculated and the measured composition data[2,3,] in which burn-up calculations were performed with SRAC[4] and MVP-BURN[5] codes with the nuclear data library JENDL-3.2[6].

2. Measurements of Irradiated LWR Fuel Compositions in REBUS Program

Table 1 shows main characteristics for the measured fuel samples. Measured nuclides and measurement errors (2σ) for composition data are shown in Table 2 and Fig. 1. Analytical methods used in the chemical assay are summarized in Table 3

Table 1 Main Characteristics for Measured Fuel Samples

Plant	BR3	Gundremmmingen	GKN-II
Reactor Type	PWR	BWR	PWR
Fuel Type	MOX	MOX	UO2
Exposure (GWd/t)*	20	62	54
Initial U-235(wt%)	DU	DU	3.8
Initial Puf (wt%)	6.9	5.5	-
Sample Name	BR3-MOX	GUN-MOX	GKN-UO2

* : Average exposure of test fuel rod

Table 2 Measured Nuclides

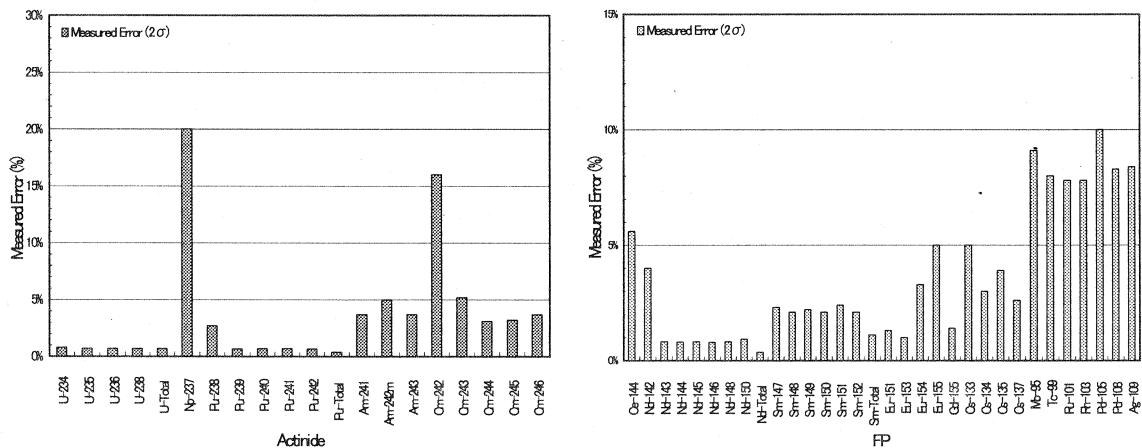| Element	Nuclide
Actinide	
U	U-234, U-235, U-236, U-238
Np	Np-237
Pu	Pu-238, Pu-239, Pu-240, Pu-241, Pu-242
Am	Am-241, Am-242m, Am-243
Cm	Cm-242, Cm-243, Cm-244, Cm-245
Fission Products	
Burn-up Indicator	Nd-143, Nd-144. Nd-145, Nd-146, Nd-148, Nd-150, Cs-137, Ce-144
Neutron Absorber	Mo-95, Tc-99, Ru-101, Rh-103, Pd-105, Pd-108, Ag-109, Cs-133, Cs-135,Nd-143,
	Nd-145, Sm-147, Sm-149, Sm-150, Sm-151, Sm-152, Eu-153, Eu-154, Gd-155

Fig.1 Measurement Errors (2 σ) for Composition Data

Table 3 Analytical Methods in Measurement

Analytical Method	Measured Nuclide
Radiochemical Analysis α -Spectrometory γ -Spectrometory	 Pu238, Cm242, Cm244 Cm243, Cs137, Ce144, Eu154
Mass Spectrometry Analysis TIMS (Thermal Ionization Mass Spectrometry) Power spike using isotopic dilution method : U233, Pu242, Am241, Nd146, Natural Sm, Eu, Gd ICP-MS (Inductively Coupled Plasma Mass Spectrometry)	 U, Pu, Am, Cm, Nd, Sm, Eu, Gd, Cs Isotopes excluding α and γ measured nuclides Mo95, Tc99, Ru101, Rh103, Pd105, Pd108, Ag109, Np237

3. Analysis of Irradiated UO2/MOX Fuel

Burn-up calculations were performed with a Pij module of SRAC and MVP-BURN using JENDL-3.2. In MVP-BURN calculations, 400,000 neutrons were generated in each burn-up step. Irradiation histories used in the burn-up calculation were determined based on the plant data and cooling periods between the fuel discharge and the measurements were considered in the burn-up calculation. For the BR3 -MOX and the GKN-UO2 fuels, pin cell models that are equivalent to the assemblies and for the GUN-MOX fuel an assembly model were applied. The burn-up calculations adopted the exposures determined by a non-destructive gamma-ray spectroscopy of Cs-137 for the fuel rods.

4. Comparison of Analyses with Measurements

Comparisons of fuel compositions for the samples of the BR3-MOX, the GUN-MOX and the GKN-UO2 fuels are shown in Figs. 2, 3 and 4.

(1) BR3-MOX

The comparisons are summarized as follows:

U-235:well agree within 1%, Pu-isotopes: well agree (<3%), Np-237&Am-242m:agree (<2 σ), Am-241 large overestimate (25%), Cm: underestimate (>20%), Major FPs: well agree, Sm-148,Eu-154&155,Gd-155: slightly underestimate, Nd-142:largely underestimate, Metal FPs: largely overestimate.

(2) GUN-MOX

The comparisons are summarized as follows:

U-235: a little overestimate (4%), Pu-239&241: slightly overestimate ($\sim$10%), Pu-238&240: well agree (<2%), Am-241(Pu-241) : largely overestimate (25%), Cm-242: agree within 2σ, Cm-244: well agree, major FPs: well agree, Sm-148,Eu-154,Gd-155: well agree, Nd-142: agree, Metal FPs: largely overestimate

(3) GKN-UO2

In this analysis, SRAC and MVP-BURN calculations based on a assembly model were performed in addition to the cell model of SRAC. These calculation results agree very well.

The comparisons are summarized as follows:

U-235: little overestimate, Pu-239: slightly overestimate ,Pu-240&241: agree (<8%), Am-241(Pu-241):

largely overestimate (25～30%), Cm-242: agree within 2 σ , Cm-244: small underestimate (12～25%), Major FPs: well agree, Sm-148,Eu-154,Gd-155 : slightly underestimate, Nd-142 : slightly underestimate, Metal FPs: largely overestimate.
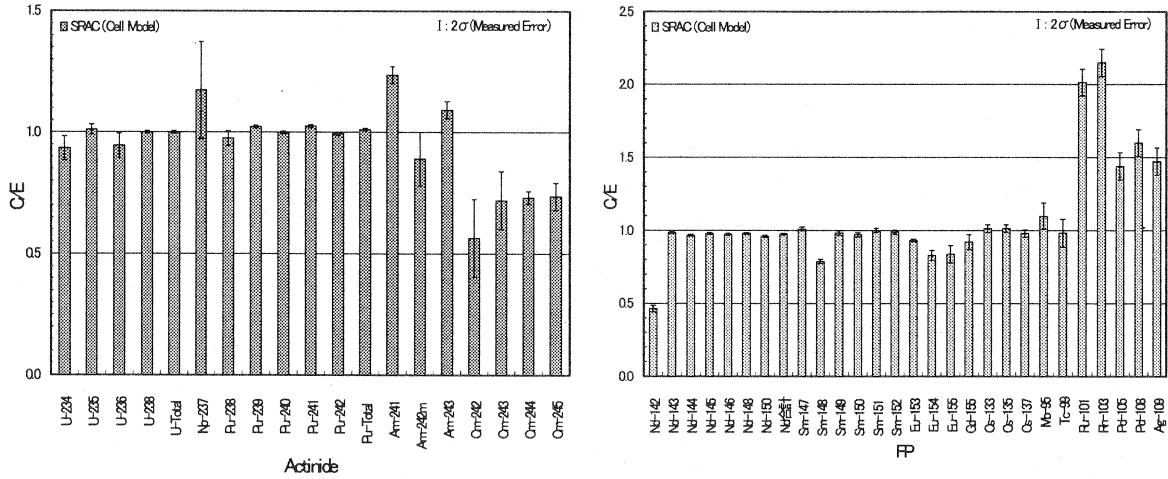

Fig.2 Comparison between Calculations and Measurements for BR3-MOX sample
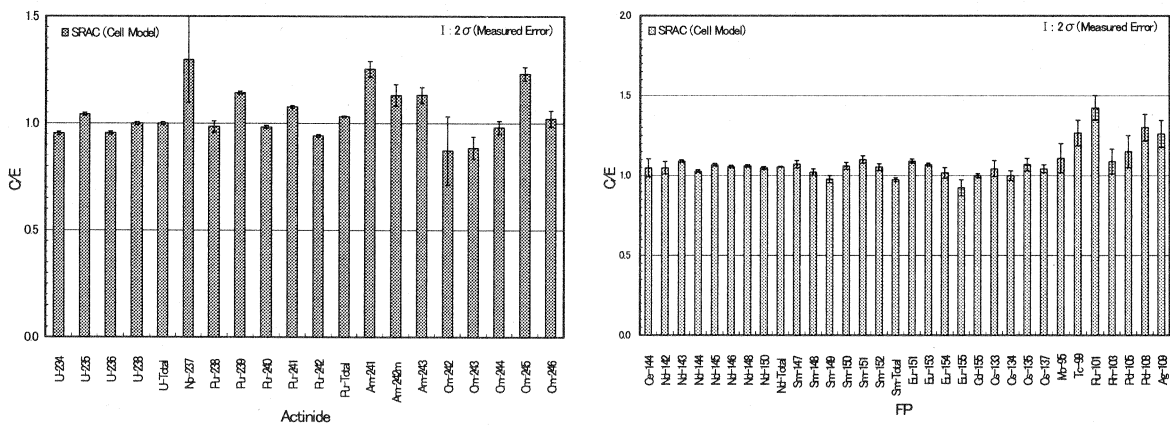

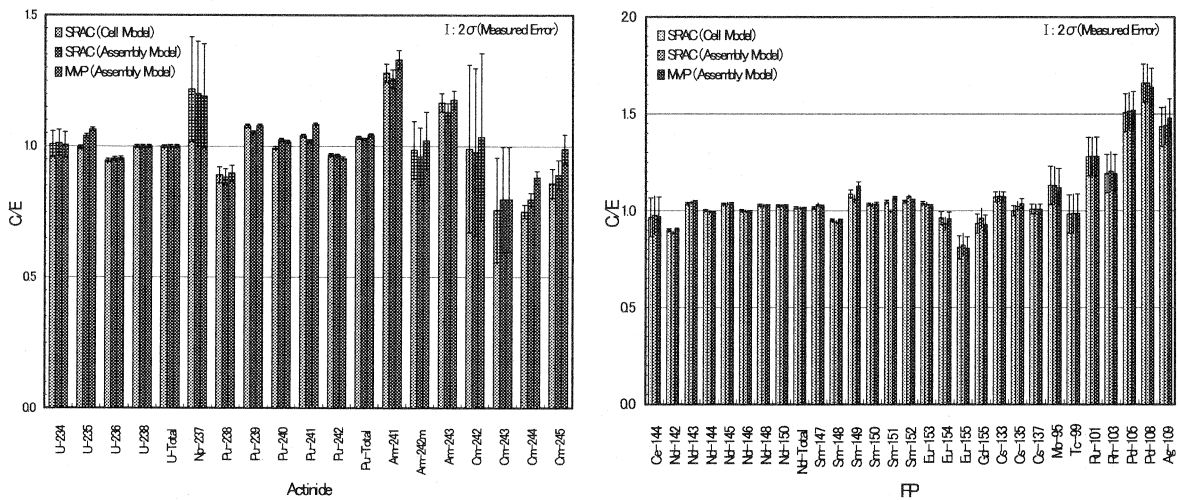Fig.3 Comparison between Calculations and Measurements for GUN-MOX sample

Fig.4 Comparison between Calculations and Measurements for GKN-UO2 sample

5. Summary and Discussions

Following conclusions were obtained through the comparisons of fuel composition analyses:

(1) The accuracies for main U and Pu-isotopes is good in low burnup MOX (BR3-MOX). However, noticeable discrepancies are observed in high burn-up MOX&UO2 (GUN-MOX and GKN-UO2) and further studies are necessary for the analysis models and also U and Pu cross sections

(2) Accuracy for TRUs beyond Pu including Np-237, is not good. For 241Am, large overestimations are observed in all samples. The improvement of TRUs cross section is strongly desired.

(3) For major FPs, the accuracies are generally good. However, large discrepancies for the metal FPs are observed. Further information is necessary for the accuracies of the chemical assay for the metal FPs. The fission yields for metal FPs changes largely along mass numbers shown in Fig. 5. Therefore, the improvement of fission yields may be necessary to decrease calculational errors.
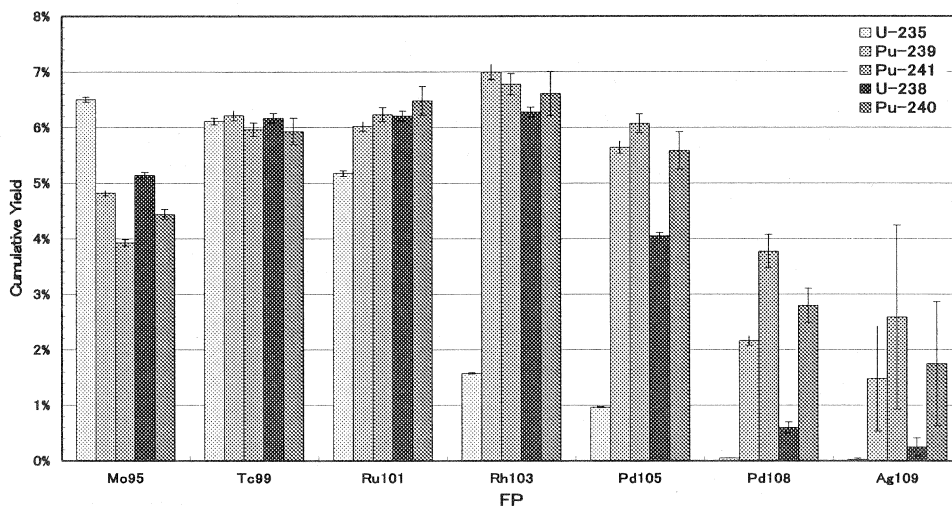
Fig.5 Comparison of Fission Yields and Uncertainties for Metal FPs (Nuclear Data : ENDF/B-VI)

(4) Nuclide-wise reactivity worth of the total inventory of each nuclide was evaluated for the fuel cell of the irradiated GKN-UO2 fuel in the experimental core based on SRAC pin cell calculations. Using these information the effects of the deviations of the calculated compositions from the measurements on the infinite multiplication factor of the cell were evaluated. The results are shown in Fig.6 for actinide nuclides and Fig.7 for FP nuclides.

In actinides, the largest three reactivity nuclides are $+2\%\Delta k$ for Pu-239 (C/E: 1.08), $+0.32\%\Delta k$ for Pu-241(C/E: 1.04) and $-0.36\%\Delta k$ for Am-241(C/E: 1.28) where the values in brackets show C/Es in the compositions. In fission products, the largest three reactivity nuclides are $-0.26\%\Delta k$ for Rh-103 (C/E: 1.19), $-0.13\%\Delta k$ for Ag-109 (C/E: 1.43) and $-0.10\%\Delta k$ for Sm-149 (C/E: 1.09) The above results shows that small analysis errors for Pu isotopes such as Pu-239 and Pu-241 cause large reactivity effects and reconfirm the conclusions shown in (1) through (3) should be reconfirmed.
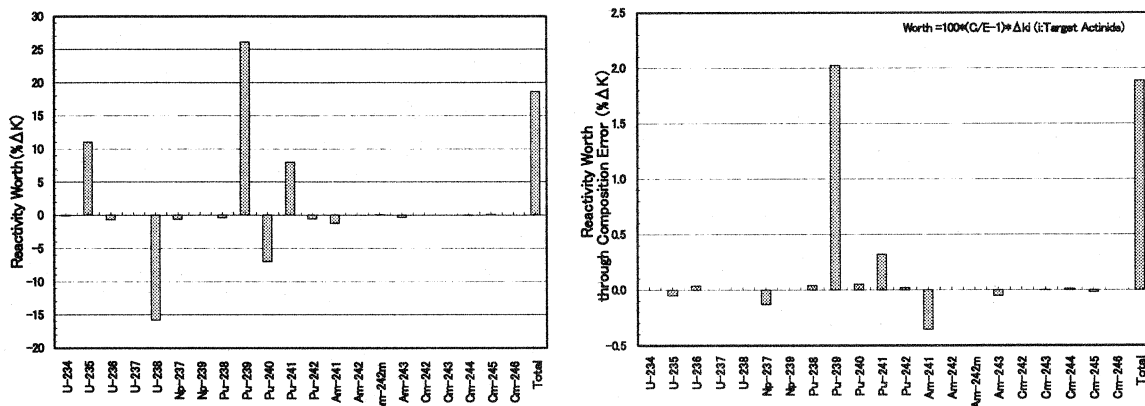
Fig. 6 Reactivity Worth of Total Inventories (Left) and Reactivity Worth Caused by Calculation Errors for Actinides (Right)
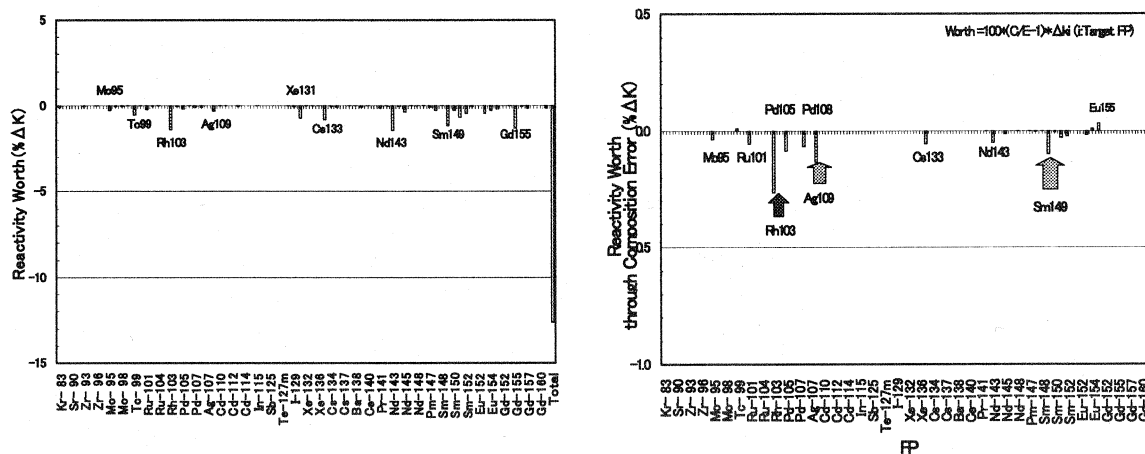
Fig. 7 Reactivity Worth of Total Inventories (Left) and Reactivity Worth Caused by Calculation Errors for FP nuclides (Right)

References

1) P. Baeten et al., "The REBUS Experimental Programme for Burn-up Credit," Proc. Int. Conf. on Nuclear Critical Safety (ICNC 2003), Oct. 20-24, 2003, Tokai, Japan (2003).

2) K. Kawashima et al., " Analysis of Reactor Physics Experiment for the Irradiated LWR MOX Fuels," Proc. Int. Conf. ICAPP '06, Reno, NV USA, June 4-8, 2006, Paper 6077(2006).

3) T. Yamamoto et al., " Preliminary Analysis of Irradiated UO2 Fuel Core in REBUS Program," Cong. ICNC2007, St. Petersburg, Russia, May 28-June 1, 2007 (2007)

4) K. Okumura, K.Kaneko and K.Tsuchihashi/., "SRAC95: General Purpose Neutronics System," JAERI-Data/Code 96-015 (1996).

5) K. Okumura, T. Mori, M. Nakagawa et al., "Validation of a Continuous-Energy Monte Carlo Burn-up Code MVP-BURN and its Application to Analysis of Post Irradiation Experiment," J. Nucl. Sci. and Technol. 37[2], 128-138(2000).

6) T. Nakagawa, K. Shibata, S. Chiba et al., "Japanese evaluated nuclear data library version 3 revision-2," J. Nucl. Sci. Technol., 32, 1259 (1995).

3.10 Short Comment to Iron Data in JENDL-3.3

Chikara Konno[1], Kentaro Ochiai[1], Masayuki Wada[2] and Satoshi Sato[1]

[1]Fusion Research and Development Directorate, Japan Atomic Energy Agency
Tokai-mura, Naka-gun, Ibaraki-ken 319-1195 Japan
e-mail : konno.chikara@jaea.go.jp

[2]Japan Computer System
2-8-1 Chuo, Mito-shi, Ibaraki-ken, 310-0805, JAPAN

We investigated what of the iron data in JENDL-3.3 caused the overestimation of the measured neutrons below ~ 10 keV in the iron experiment at JAEA/FNS through the DORT analyses based on the iron data in ENDF/B-VII.0. It was found out that the first inelastic scattering cross section data of ^{57}Fe in JENDL-3.3 caused the overestimation.

1. Introduction

We presented analysis results of the integral experiments at JAEA FNS with recent nuclear data libraries (JENDL-3.3 [1], FENDL-2.1 [2], JEFF-3.1 [3] and ENDF/B-VII.0 [4]) and MCNP-4C [5] at the last symposium on nuclear data [6]. One problem appeared in the iron experiment [7] as shown in Fig. 1. The calculation with JENDL-3.3 overestimated measured neutrons below ~ 10 keV for the iron experiment, while other calculations agreed with them well. Figures 2 and 3 indicate the problem. It was expected that the iron data in JENDL3.3 had some problems. In this paper we investigate what of the iron data in JENDL-3.3 causes the overestimation based on ENDF/B-VII.0.

2. Method

The Sn code DORT [8] was used for this analysis because this code gives almost the same results as MCNP very quickly. Multigroup libraries of neutron 175 group structure with self-shielding correction were produced with the TRANSX code [9] from MATXS files. The MATXS files supplied from JAEA Nuclear Data Center were adopted for JENDL-3.3 [10]. Since MATXS files for ENDF/B-VII.0 were not released officially, they were produced with the NJOY99.161 code [11] and patch [12] from BNL National Nuclear Data center for

ourselves.

3. Results and discussion

First in order to examine which iron isotope caused the overestimation, we calculated neutron spectra of the iron experiment with DORT, where the iron isotopes in JENDL-3.3 were replaced with those in ENDF/B-VII.0 one by one. Figures 4 and 5 show the result. As a result, it was found out that the ^{57}Fe data in JENDL-3.3 caused the overestimation of the measured neutrons below ~ 10 keV.

Next we compared the ^{57}Fe data in JENDL-3.3 with those in ENDF/B-VII.0 every reaction. The elastic and first inelastic scattering cross section data of ^{57}Fe in JENDL-3.3 were different from those in ENDF/B-VII.0 largely as shown in Figs. 6 and 7. In order to investigate which reaction caused the overestimation, we calculated neutron spectra of the iron experiment with DORT, where the elastic or first inelastic scattering cross section data of ^{57}Fe in JENDL-3.3 were replaced with those in ENDF/B-VII.0 separately. Figures 8 and 9 show the result. It was concluded that the first inelastic scattering cross section of ^{57}Fe in JENDL-3.3 caused the overestimation of the measured neutrons below ~ 10 keV in the iron experiment.

4. Summary

We investigated what of the iron data in JENDL-3.3 caused the overestimation of the measured neutrons below ~ 10 keV in the iron experiment at JAEA/FNS through the DORT calculations based on the iron data in ENDF/B-VII.0. It was found out that the first inelastic scattering cross section data of ^{57}Fe in JENDL-3.3 caused the overestimation. The ^{57}Fe data should be revised in JENDL-4.

References

[1] K. Shibata, et al. : J. Nucl. Sci. Tech. 39, 1125 (2002).

[2] D. Lopez Al-dama and A. Trokov : "FENDL-2.1 Update of an evaluated nuclear data library for fusion applications," IAEA Report INDC(NDS)-467 (2004).

[3] A. Koning, et al. (Ed.) : "The JEFF-3.1 Nuclear Data Library," JEFF Report 21, OECD Nuclear Energy Agency (2006).

[4] M.B. Chadwick, et al. : Nuclear Data Sheets 107, 2931 (2006).

[5] J.F. Briesmeister (Ed.) : "MCNP - A General Monte Carlo N-Particle Transport Code, Version 4C," LA-13709-M (2000).

[6] K. Ochiai, et al. : "SND2006-V.11: Analyses of Benchmark Experiments at FNS with Recent Nuclear Data Libraries," T. Fukahori (Ed.), Proc. of 2006 Symposium on Nuclear Data, Jan. 25-26, 2007, RICOTTI, Tokai-mura, Ibaraki-ken, Japan,

ISBN978-4-89047-138-6, Nuclear Data Division, Atomic Energy Society of Japan (2007) [CD-ROM].

[7] F. Maekawa, et al. : "Data Collection of Fusion Neutronics Benchmark Experiment Conducted at FNS/JAERI," JAERI-Data/Code 98-021 (1998).

[8] DOORS3.2a : One, Two- and Three-Dimensional Discrete Ordinates Neutron/Photon Transport Code System, RSICC CODE PACKAGE CCC-650 (2007).

[9] R.E. MacFarlane : "TRANSX 2: A Code for Interfacing MATXS Cross-Section Libraries to Nuclear Transport Codes," LA-12312-MS (1993).

[10] K. Kosako, et al. : "The libraries FSXLIB and MATXSLIB based on JENDL-3.3," JAERI-Data/Code 2003-011 (2003).

[11] R.E. MacFarlane and D.W. Muir : "The NJOY Nuclear Data Processing System, Version 91, " LA-12740-M (1994).

[12] http://www.nndc.bnl.gov/exfor/4web/processing.html.
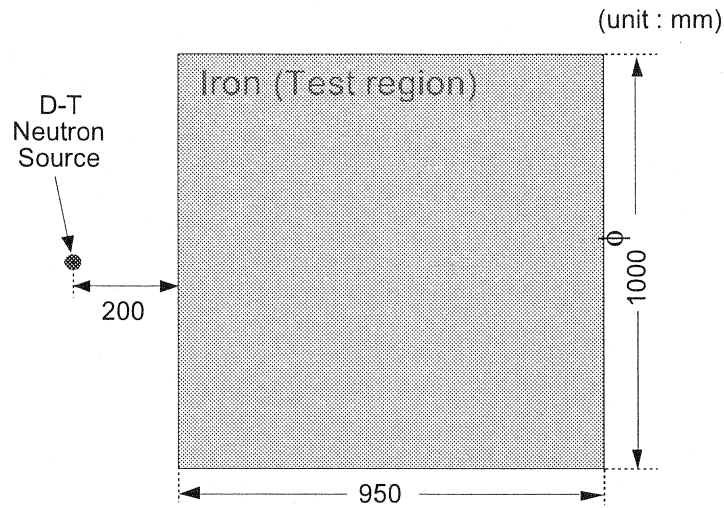
Fig. 1   Experimental configuration of iron experiment.

Fig. 2 Measured and calculated neutron spectra at depth of 310 mm in iron experiment.(1)
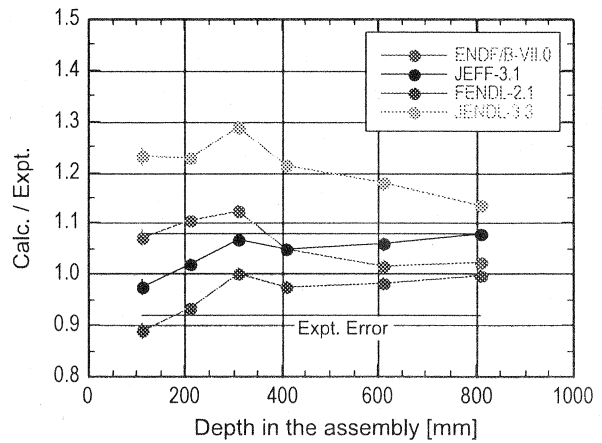
Fig. 3 C/E for neutron flux from 0.1 keV to 1 keV in iron experiment.(1)

Fig. 4 Measured and calculated neutron spectra at depth of 310 mm in iron experiment.(2)
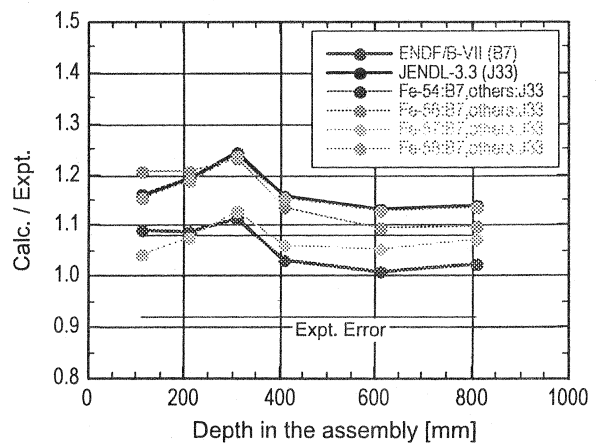
Fig. 5 C/E for neutron flux from 0.1 keV to 1 keV in iron experiment.(2)
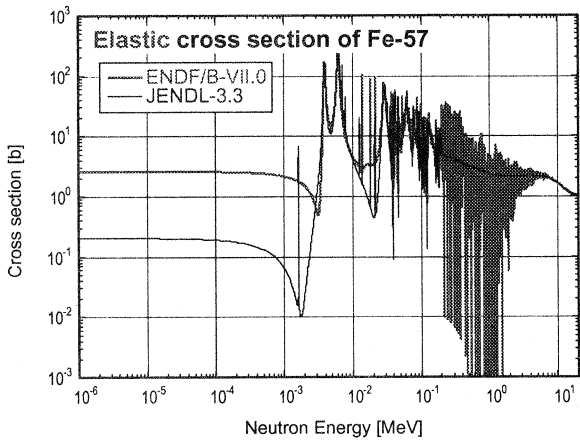
Fig. 6 Elastic cross section of ^{57}Fe
in JENDL-3.3 and ENDF/B-VII.0.
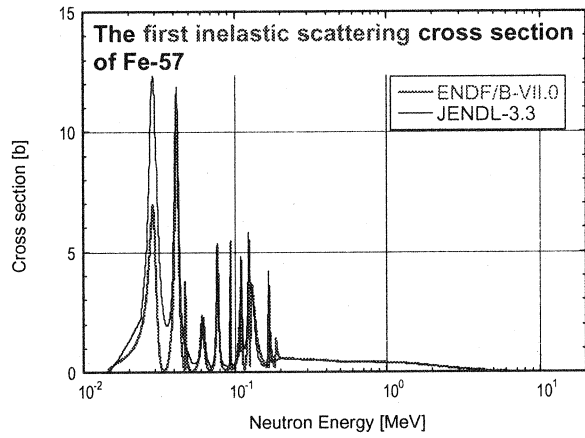
Fig. 7 First inelastic cross section of ^{57}Fe
in JENDL-3.3 and ENDF/B-VII.0.
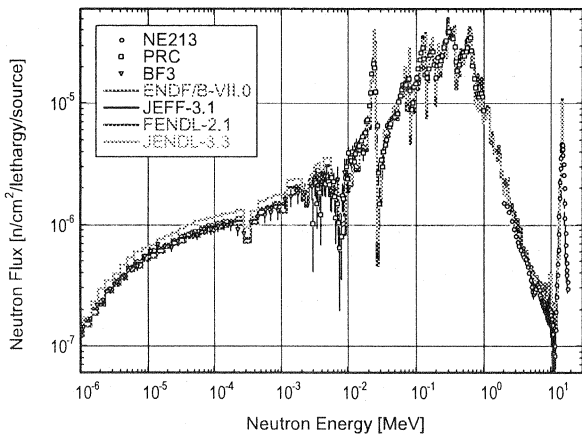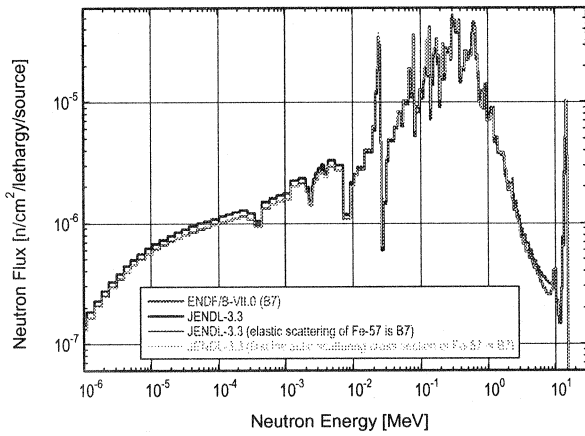

Fig. 8 Measured and calculated neutron spectra
at depth of 310 mm in iron experiment.(3)
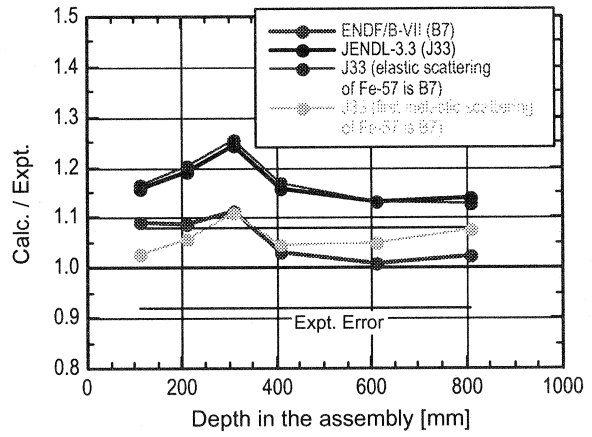
Fig. 9 C/E for neutron flux from 0.1 keV
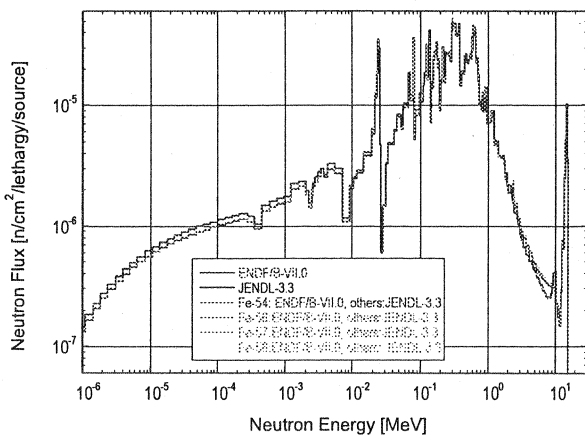to 1 keV in iron experiment.(3)

3.11 Nuclear Data Benchmark for Sodium Voided Reactivity Worth with Improved Neutronics Simulation Method

Go Chiba

Japan Atomic Energy Agency
e-mail: chiba.go@jaea.go.jp

Abstract

In order to assess the evaluated nuclear data files for sodium voided reactivity worth (SVRW) predictions, benchmark calculations were performed with deterministic neutron transport solvers. The benchmark result indicated that JENDL-3.3 and JEFF-3.1 predict well SVRW. However, it was found that ENDF/B-VII.0 underestimates leakage components of SVRW due to the large value of P_1 elastic scattering cross sections of sodium.

I Introduction

The sodium voided reactivity worth (SVRW) is one of the most important neutronics parameters in core designs and safety analyses of fast reactors. Since a prediction accuracy for SVRW depends on an accuracy of nuclear data used in prediction calculations, it is important to assess accuracies of the evaluated nuclear data files for SVRW predictions.

In a sodium-voided situation, a neutron leakage from a reactor core increases and a neutron energy spectrum becomes harder. The former brings a negative reactivity to a reactor core. On the other hand, the latter brings a positive reactivity normally in fast reactors since neutrons with higher energy are 'more important' in a view of a neutron multiplication in a reactor core.

The nuclear data of sodium has a strong sensitivity to SVRW. In addition, the nuclear data of major actinides, such as uranium-238 and plutonium-239, also have strong sensitivities since energy spectra of neutron importance functions depend on those. Hence, the nuclear data for sodium and the major actinides should be assessed for accurate SVRW predictions.

For the assessment of the nuclear data, integral data are beneficial. In the present study, we utilize the experimental SVRW data obtained in the MZA assembly[1] constructed at the ZEBRA critical facility in order to assess the evaluated nuclear data files, JENDL-3.3, JEFF-3.1 and ENDF/B-VII.0. Since it is important to reduce uncertainties caused by numerical methods for neutronics simulations in benchmark calculations, we perform this benchmark calculation with an improved numerical procedure.

II Utilized experimental data

As described in the introduction, we utilize the data obtained in the MZA assembly[1] for the present study. This data for core specifications and material number densities was re-evaluated by Kaise and Osada in 2003. In this data, unit lattices are simplified into one-dimensional slab geometries.

Figure 1 shows the specification of the MZA assembly. In the present calculation, we utilize the four SVRW data in which radial central regions were voided. Voided regions are shown with their step indices in Fig.1. This SVRW experiment is not a 'cumulative' SVRW experiment. At the void step 3, regions numbered as 1 and 2 are not voided, for example. The non-leakage component is dominant in SVRW of the step 1, while the leakage component is dominant in SVRW of the step 4.

III Numerical method

We perform the present benchmark calculation with deterministic neutron transport solvers since Monte-Carlo codes are inappropriate for small reactivity calculations. In a conventional deterministic calculation procedure, each lattice is homogenized in a unit lattice calculation, and spatially-homogenized lattices are used in whole-core calculations. This 'lattice homogenization' results in some ambiguities in calculation. Hence, we perform this benchmark calculation without whole-lattice homogenizations. Namely, we treat heterogeneities of unit lattices explicitly in whole-core calculations.

Figure 2 shows a model used for the present whole-core calculation. As shown in this figure, a unit lattice is composed of several material plates. Actually, these material plates were covered by thin materials named as 'can regions'. In the present calculation, only these can regions are homogenized in unit lattice calculations.

Unit lattice calculations are performed with a SLAROM-UF code[2] and a 900-group library. Below 50keV, a ultra-fine energy group library is adopted. The calculated 900-group cross section in each material plate and can region is collapsed to 70-group cross section, and only can regions are homogenized after that.

The plate-wise 70-group cross sections obtained at the above unit lattice calculations are utilized in whole-core calculations. The whole-core calculations are performed with a discrete ordinates neutron transport solver SNT. In this calculation, the double-Gaussian Tchebyshev angular quadrature set is utilized. The details of SNT and this quadrature set can be found in the reference[3].

In this calculation, lattices located far from the voided region are treated homogeneously. This treatment was validated in the previous study[3]

The effective delayed neutron fraction, used as a unit converter for reactivities, is calculated from Tuttle's fission yield data, Keepin's delayed neutron family fraction data and Saphier's delayed fission spectrum data.
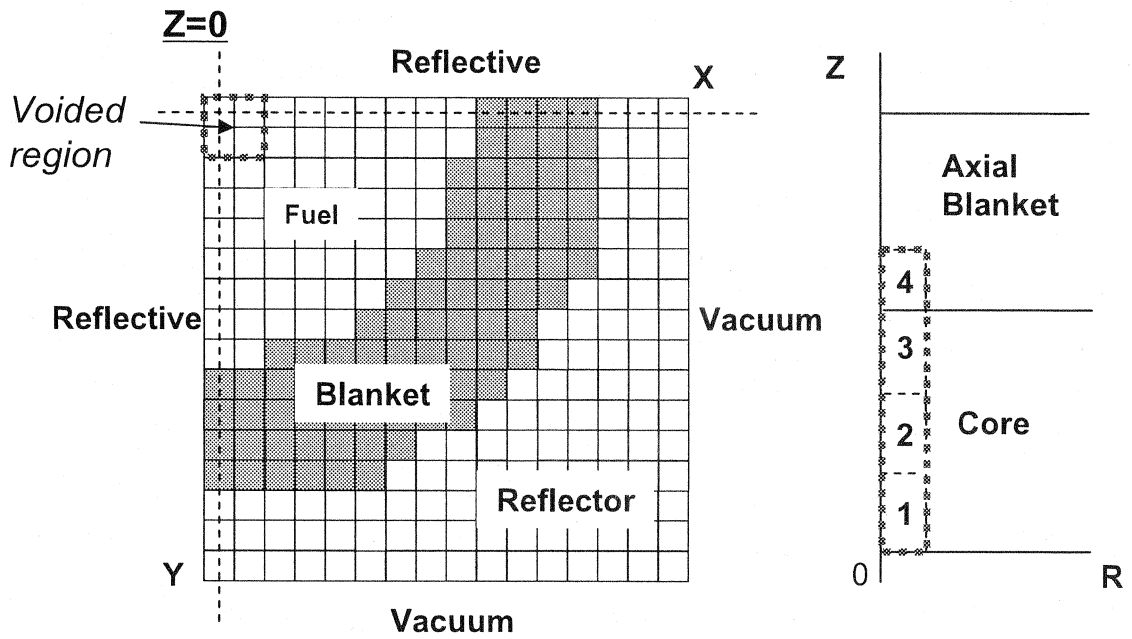
Fig.1 Specification of MZA
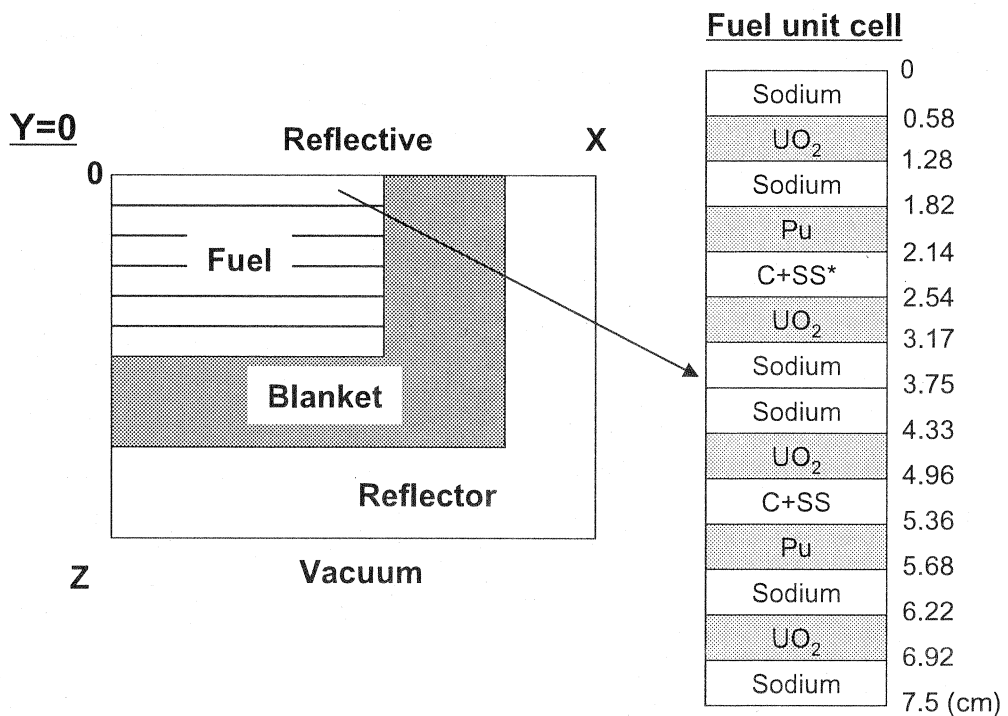
Fig.2 Model used for whole core calculation

IV Results

Table 1 shows obtained C/E values with relative experimental errors.

Table 1: C/E values with experimental errors

Void step	Relative experimental error	JENDL-3.3	JEFF-3.1	ENDF/B-VII.0
1	0.022	0.972	1.006	0.941
2	0.020	1.100	1.186	1.135
3	0.017	1.039	1.056	0.965
4	0.016	0.955	0.973	0.887

Since SVRW is a sum of a positive non-leakage component and a negative leakage component, SVRW gives a value close to zero in some cases. In such cases, it is difficult to extract useful information from relative comparisons. Hence, we also calculate (C-E) values normalized with each component of SVRW. Using these normalized (C-E) values, it becomes possible to grasp a degree of a difference between C- and E-values. Under an assumption that a C-value of a non-leakage component has no error, a (C-E) value normalized with a leakage component means a relative difference between C- and E-values of a leakage component.

Table 2 shows the normalized (C-E) values. The leakage component of step 1 and the non-leakage component of step 4 are negligible. Hence, we omit the (C-E) value normalized with these in this table. Absolute experimental errors are also normalized with each component, and shown in this table.

Table 2: Normalized (C-E) values

Void step	Normalized component	Normalized absolute experimental error	JENDL-3.3	JEFF-3.1	ENDF/B-VII.0
1	Non-L*	0.05	-0.02	+0.00	-0.05
2	Non-L	0.06	+0.02	+0.03	+0.02
	L**	0.08	-0.02	-0.04	-0.03
3	Non-L	0.09	-0.06	-0.09	+0.06
	L	0.03	+0.02	+0.03	-0.02
4	L	0.04	-0.03	-0.02	**-0.09**

* Non-leakage, ** Leakage

As shown in table 2, JENDL-3.3 and JEFF-3.1 predict well SVRW. However, it is clearly seen that ENDF/B-VII.0 underestimates the leakage component in the step 4. Through a sensitivity analysis, it is found that this difference comes from a difference in values of P_1 component of elastic scattering cross sections of sodium.

Figure 3 shows P_1 coefficients of elastic scattering cross sections of sodium. This
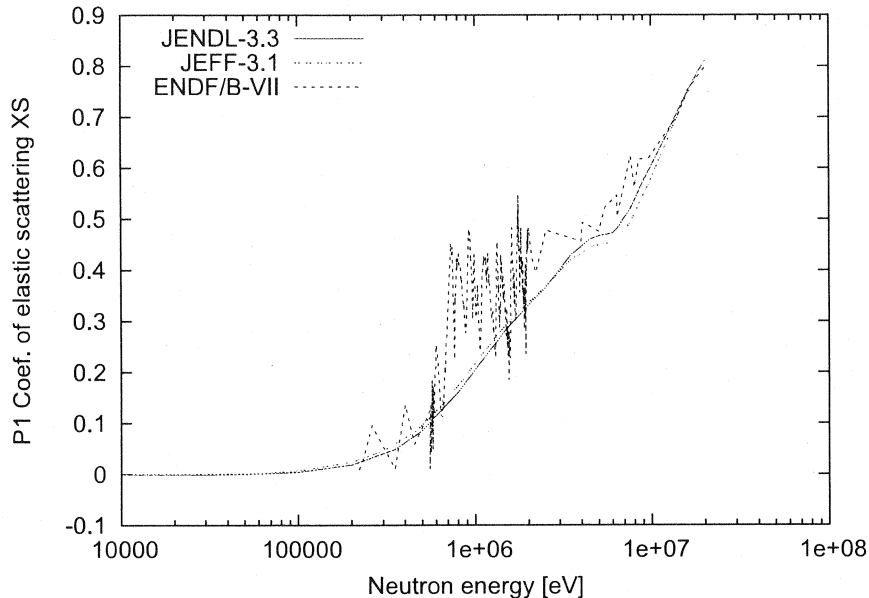
Fig.3: P_1 component of elastic scattering cross sections of sodium

difference in the cross sections between ENDF/B-VII.0 and others also results in large differences in criticalities of small fast reactors(4). Hence, it is required for the nuclear data community to investigate this difference.

V   Conclusion

In order to assess the evaluated nuclear data files for SVRW predictions, benchmark calculations with integral data have been performed. The benchmark result has indicated that JENDL-3.3 and JEFF-3.1 predict well SVRW. However, it has been found that ENDF/B-VII.0 underestimates leakage components due to the large value of P_1 elastic scattering cross sections of sodium.

Acknowledgment

The author wishes to express his gratitude to Dr.Okajima of Japan Atomic Energy Agency who provided useful comments.

References

[1] Y.Kaise, H.Osada, 'Investigation of MOZART Experimental Data and Analysis of MOZART Experiment Using JFS-3-J3.2R Group Constant,' JNC TJ9400 2003-009,

Japan Nuclear Cycle Development Institute, (2003)[in Japanese].

[2] T.Hazama, *et al.*, 'Development of SLAROM-UF: A Lattice Calculation Code with Fine and Ultra-fine Energy Group Structure,' *J. Nucl. Sci. Technol.*, **43**, p.908 (2006).

[3] G.Chiba, Y.Shimazu, 'Sodium Void Reactivity Worth Calculations for Fast Critical Assemblies without Whole-Lattice Homogenization,' *J. Nucl. Sci. Technol.*, **44**, p.1526 (2007).

[4] G.Chiba, *et al.*, 'Benchmark Test of Evaluated Nuclear Data Files for Fast Reactor Neutronics Application,' JAEA-Research 2007-051, Japan Atomic Energy Agency, (2007)[in Japanese].

3.12 CBGLIB: A Multi-group Neutron Library for Precise Neutronics Simulations

Go Chiba

Japan Atomic Energy Agency
e-mail: chiba.go@jaea.go.jp

Abstract

A multi-group neutron library CBGLIB has been developed. The following techniques are developed and implemented into CBGLIB: (1) nuclide- and energy group-dependent Bell factors, (2) multiple R-parameters, and (3) adjustment of self-scattering cross sections to consider angular-moment dependence of total cross sections. A numerical test for pincell problems has been performed. Infinite multiplication factors calculated with CBGLIB agree with reference Monte-Carlo solutions within $0.2\%\Delta k/k$.

I Introduction

In order to carry out accurately and easily neutronics analyses for critical assemblies or power reactors, we have been developing an integrated neutronics simulation code system named CBG. So far, a lattice code SLAROM-UF[1] has been incorporated into CBG to obtain self-shielded resonance cross sections. SLAROM-UF adopts a ultra-fine energy group library for the resonance energy range. Rigorous self-shielded cross sections, therefore, can be obtained in unit lattice calculations with SLAROM-UF. A usage of the ultra-fine group library has a merit in accuracies. However, it also has a demerit in computational burdens: it requires large computer memory and long computation time.

In the present study, we develop a new multi-group neutron library CBGLIB for the CBG system. While CBGLIB has the coarse 107-group structure same as the SRAC library[2], the accuracy of CBGLIB is better than that of the SRAC library by virtue of implementations of several techniques.

In the present paper, we will describe the techniques to improve accuracies of multi-group libraries, and show a performance of CBGLIB for pincell calculations.

II An integrated neutronics simulation code system, CBG

An integrated neutronics simulation code system CBG has been developed for fast nuclear data benchmark calculations[3] and for accurate fast critical assembly analyses[4]. While CBG could be applied only to fast reactor calculations initially, it can solve also thermal reactor neutronics at the present time.

Most part of CBG is written in the C++ programming language. CBG is composed of 'classes,' namely units containing data and methods, in order to allow easy handling of data. Data needed in neutronics calculations, such as cross sections, lattice geometries,

core geometries, are treated as common objects in CBG, and these are utilized by all the neutron solvers as input (or output). Hence, once objects to determine information of a target system are prepared, various calculations, for example, eigenvalue or small reactivity calculations, can be conducted with both the transport theory and the diffusion theory with these objects. The above feature of CBG is briefly illustrated in **Fig.1**. CBG has several neutron transport/diffusion solvers for both lattice and core calculations. Features of these solvers can be found in the reference(4, 5).

III Development of CBGLIB

In the present study, we develop a new multi-group neutron library CBGLIB for the CBG system. CBGLIB has the same 107-group structure as the SRAC-library. CBGLIB includes infinite dilution cross sections, scattering matrices, self-shielding factors, incident energy-dependent fission spectrums and probability tables.

Resonance calculations with multi-group libraries have several limitations, and these limitations reduce accuracies of calculations with multi-group libraries. In the present study, we develop several techniques in order to improve the accuracies.

In the following, the details of these techniques will be described.

1 Nuclide- and energy group-dependent Bell factors

Bell factor a is used to improve the following rational approximation for a fuel-escape probability $P_{esc}(E)$:

$$P_{esc}(E) \approx \frac{a}{\tilde{l}\Sigma(E) + a} \tag{1}$$

where the notations are usual ones.

In an isolated fuel-moderator pincell, a NR-based neutron flux $\phi(E)$ in the fuel region is expressed as follows:

$$\phi(E) = \frac{\Sigma_0^F}{\Sigma_t^F(E)} \left(1 - P_{esc}(E)\right) + P_{esc}(E) \tag{2}$$

where $\Sigma_t^F(E)$ and Σ_0^F is the total cross section and the potential cross section of the fuel region, respectively. On the other hand, the neutron flux in the fuel region can be approximately written using the rational approximation as

$$\phi_a(E) = \frac{\tilde{l}\Sigma_0^F + a}{\tilde{l}\Sigma_t^F(E) + a}. \tag{3}$$

A common value for Bell factor is normally used in a lattice code. However, an optimum value for Bell factor depends on $\tilde{l}\Sigma_t^F(E)$. Hence, we give an optimum value for Bell factor to each nuclide and each energy group in CBGLIB.

An optimum value for Bell factor is determined so as to preserve the following relation in an isolated pincell:

$$\frac{\langle \sigma(E)\phi(E)\rangle}{\langle \phi(E)\rangle} = \frac{\langle \sigma(E)\phi_a(E)\rangle}{\langle \phi_a(E)\rangle} \tag{4}$$

where the bracket $<>$ refers to an integral on energy. The integral calculations on the left hand side of Eq.(4) are performed with the sub-group method.
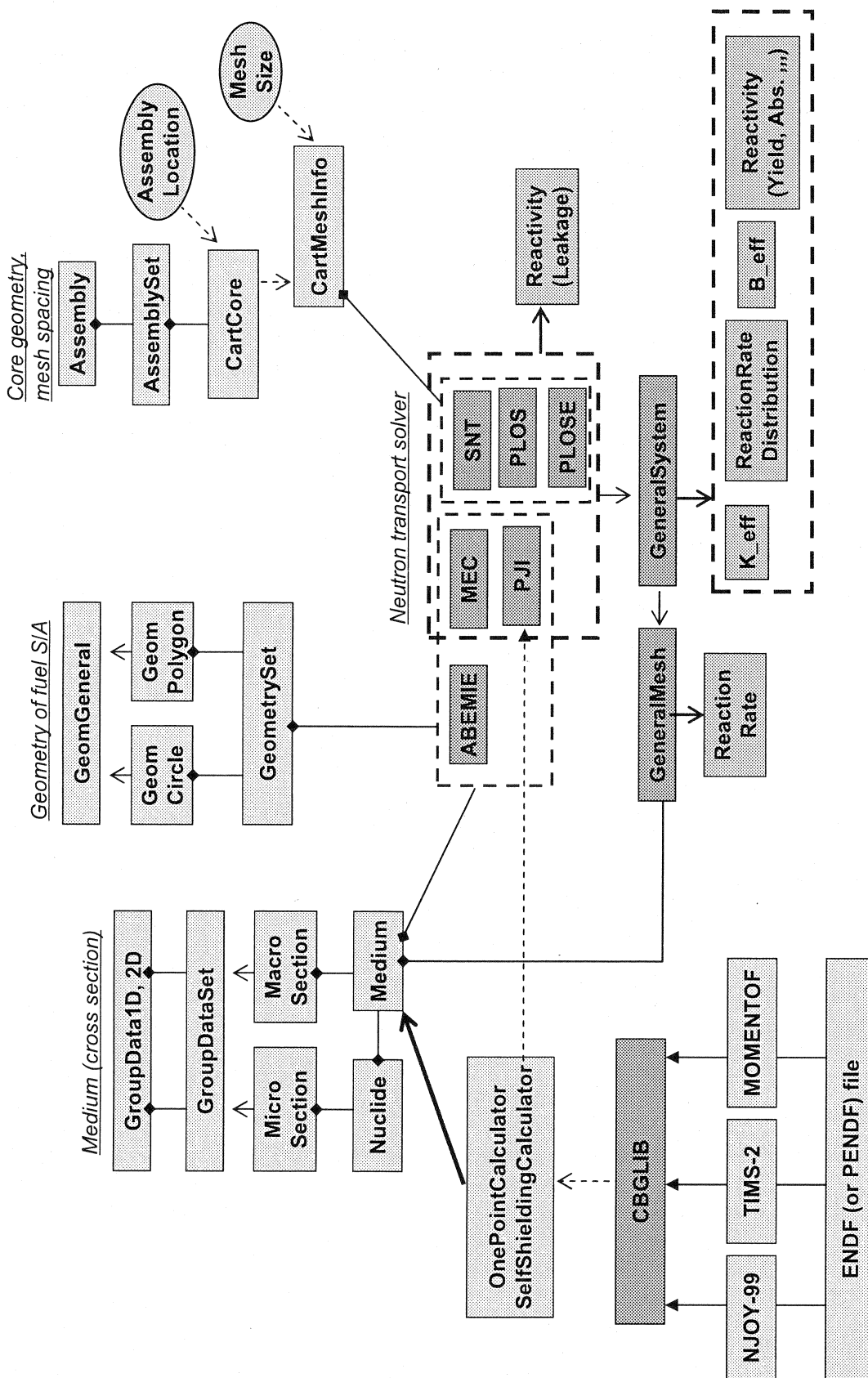
Fig.1 Brief description of CBG

2 Multiple R-parameters

Normally, multi-group libraries cannot consider a resonance interference (RI) between different nuclei. An R-parameter method for JAERI Fast Set-3(JFS-3) or a G-table method for MGCL is to overcome this difficulty of multi-group libraries.

In a usual f-table method, f-factors are calculated in advance at several points of temperature T and dilution cross section σ_0. The R-parameter method adds another parameter, R-parameter, into f-tables. Let us consider a case to prepare an f-table for nuclide i. When we consider RI with nuclide j, the R-parameter is defined as N_j/N_i in which N denotes a number density. In CBGLIB, f-factors are prepared at seven points of R-parameters. The concept of the G-table method is the same.

Both R-parameters of JFS-3 and a G-table of MGCL consider RIs between uranium-238 and other nuclei. In the specific energy range, however, RIs between different plutonium isotopes or between uranium-235 and plutonium isotope are important. Hence, nuclide j, with which RI is considered, depends on nuclide i and energy group in CBGLIB.

When we have to consider RIs to several nuclei, CBGLIB can approximately treat them with the following procedure (we call this a 'multiple R-parameter method'):

$$\sigma_{eff} = \left(\prod_{j=1}^{J} \frac{\sigma_{eff}^i}{\sigma_{eff}^{w/oRI}} \right) \cdot \sigma_{eff}^{w/oRI} \tag{5}$$

where σ_{eff} is a RIs-corrected cross section, σ_{eff}^j is a shielded cross section considering RI with nuclide j, and $\sigma_{eff}^{w/oRI}$ is a shielded cross section without considering RI. This multiple R-parameter method is based on an assumption that RI with a nuclide is independent on RIs with other nuclei.

3 Adjustment of self-scattering cross sections

It has been reported in the reference[6] that coarse group calculations with cross sections collapsed from ultra-fine group calculations do not yield the same results as the ultra-fine group calculations. This 'collapsing error in coarse group calculations' is caused by a fact that fine-group total (transport) cross sections are collapsed using neutron flux as a weight function.

Let us consider the following multi-group neutron transport equation with the transport approximation:

$$\mu \frac{\partial \phi_g(x,\mu)}{\partial x} + \Sigma_{tr,g}\phi_g(x,\mu) = \frac{1}{2}\sum_{g'}\Sigma_{g'\to g}\phi_{g'}^0(x) + \frac{1}{2}Q_g(x). \tag{6}$$

After the angular neutron flux in the second term in the left hand side of Eq.(6) is expanded by the first-order Legendre polynomials, Eq.(6) becomes

$$\mu \frac{\partial \phi_g(x,\mu)}{\partial x} + \frac{1}{2}\Sigma_{tr,g}\phi_g^0(x) + \frac{3}{2}\mu\Sigma_{tr,g}\phi_g^1(x) = \frac{1}{2}\sum_{g'}\Sigma_{g'\to g}\phi_{g'}^0(x) + \frac{1}{2}Q_g(x). \tag{7}$$

Next, we collapse the above equation as

$$\mu \frac{\partial \phi_G(x,\mu)}{\partial x} + \frac{1}{2}\Sigma_{tr,G}^0\phi_G^0(x) + \frac{3}{2}\mu\Sigma_{tr,G}^1\phi_G^1(x) = \frac{1}{2}\sum_{G'}\Sigma_{G'\to G}\phi_{G'}^0(x) + \frac{1}{2}Q_G(x) \tag{8}$$

where

$$\Sigma_{tr,G}^n = \frac{\sum\limits_{g \in G} \Sigma_{tr,g} \phi_g^n}{\sum\limits_{g \in G} \phi_g^n}. \tag{9}$$

Equation (8) can be transformed using the following approximation,

$$\frac{1}{2}\phi_G^0(x) + \frac{3}{2}\mu\phi_G^1(x) \approx \phi_G(x, \mu) \tag{10}$$

into

$$\mu\frac{\partial \phi_G(x, \mu)}{\partial x} + \Sigma_{tr,G}^1 \phi_G(x, \mu) = \frac{1}{2}\sum_{G'}\left[\Sigma_{G' \to G} + \delta_{GG'}(\Sigma_{tr,G}^1 - \Sigma_{tr,G}^0)\right]\phi_{G'}^0(x) + \frac{1}{2}Q_G(x). \tag{11}$$

The above discussion suggests that the transport cross sections should be collapsed with neutron current as a weight function.

In order to validate the above suggestion, we perform a simple numerical test. We prepare a fine 454-group library ($\Delta u = 0.01$ from 1.8554eV to 101.3eV, no thermal scattering), and calculate pincell problems of a 'LWR next generation fuel benchmark(7)' with this fine-group library. After that, the fine-group cross sections are collapsed into coarse 70-group ones, and calculate the same problems with the coarse-group cross sections. In this cross section collapsing, neutron flux or current is used for transport cross sections as a weight function. These pincell calculations are performed with a MOC solver MEC to obtain neutron current. Results are shown in **table 1**.

Table 1: Infinite multiplication factors of pincell problems

	454-group	70-group (flux-weight)	70-group (current-weight)
UO$_2$	1.47760	1.47298	1.47787
MOX	1.23287	1.23080	1.23324

This result clearly shows that a current-weight cross section collapsing results in good agreement between fine- and coarse-group calculations.

Large differences between $\Sigma_{tr,G}^0$ and $\Sigma_{tr,G}^1$ are observed in energy groups in which the large resonances of uranium-238 exist. **Table 2** shows a ratio of σ_{tr}^1 to σ_{tr}^0 of uranium-238.

Table 2: Ratio of σ_{tr}^1 to σ_{tr}^0 of uranium-238

Energy group (energy range)	UO$_2$	MOX
51 (29.0-37.3eV)	3.74	5.28
53 (17.6-22.6eV)	3.14	2.84
57 (6.5-8.3eV)	5.68	3.22

From this result, current-weighted cross sections take larger value than flux-weighted cross sections.

This 'current-weighted' cross section is difficult to calculate within a framework of multi-group libraries since the equivalent theory cannot be applied to 'current-weighted' cross section calculations. Hence, we prepare correction factors which are multiplied by 'flux-weighted' total cross sections to obtain 'current-weighted' total (or transport) cross sections. Values of this factor are set as $\sigma_{tr}^1/\sigma_{tr}^0$ of the UO$_2$ pincell result shown in table 2 only for group 51, 53 and 57 in CBGLIB.

IV Numerical results

Firstly, we calculate the UO$_2$ pincell of the benchmark problem[7] with CBG and CBGLIB. Self-shielded resonance cross sections are calculated by Dancoff factor method. Neutron slowing-down by heavy nuclides below 30eV is treated similar to the WR approximation: *i.e.* only absorption cross sections are considered as dilution cross sections. With the calculated self-shielded resonance cross sections, eigenvalue calculation is performed with a collision probability solver PJI. Thermal scattering is considered below 3.92eV.

Reference self-shielded cross sections are obtained with SRAC/PEACO, and a reference eigenvalue calculation is also carried out with PJI.

We estimate an effect of a difference in self-shielded cross sections on eigenvalues by the collision probabiity-based perturbation theory[8]. **Figure 2** shows an energy breakdown of error contribution to k_∞ for the UO$_2$ pincell. We can see an improvement induced by the adoption of R-parameters in this table.
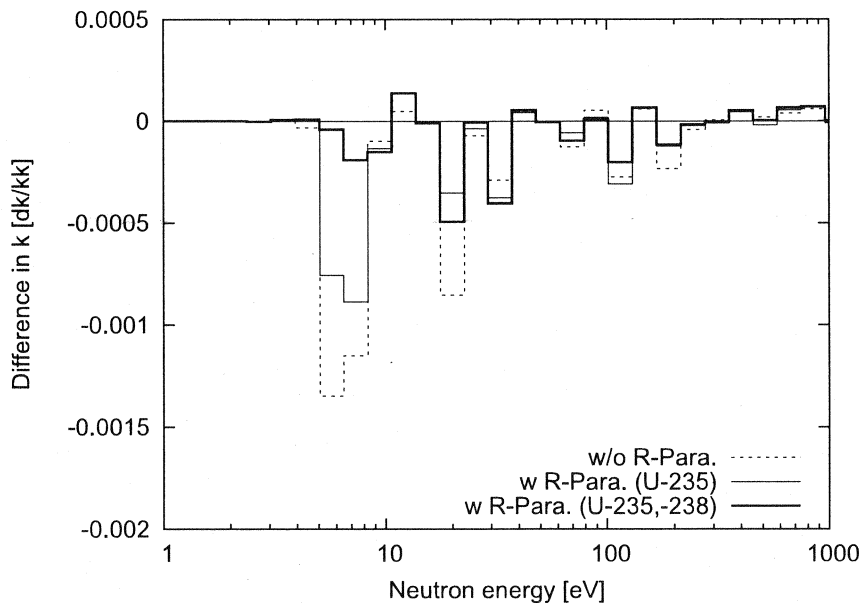
Fig.2: Energy breakdown of error contribution to infinite multiplication factor (UO$_2$ pincell)

Next, we compare k_∞ calculated by CBG with continuous-energy Monte-Carlo solu-

tions. The result is shown in **table 3**. In order to estimate an efficiency of the techniques

Table 3: Comparison in infinite multiplication factors

	UO$_2$	MOX
Reference	1.4312	1.1909
CBG	1.42871 (-0.17%)	1.19193 (+0.09%)
CBG (w/o the present techniques)	1.41619 (-1.05%)	1.18477 (-0.51%)

described in the present paper, results obtained without the present techniques are also shown in this table.

CBG results obtained with the present techniques agree with the references within $0.2\%\Delta k/k$. This numerical result shows a good performance of CBGLIB.

V Conclusion

A multi-group neutron library CBGLIB has been developed. The following techniques are developed and implemented into CBGLIB: (1) nuclide- and energy group-dependent Bell factors, (2) multiple R-parameters, and (3) adjustment of self-scattering cross sections to consider angular-moment dependence of total cross sections. A numerical test for pincell problems has been performed. Infinite multiplication factors calculated with CBGLIB agree with reference Monte-Carlo solutions within $0.2\%\Delta k/k$.

Acknowledgment

References

[1] T.Hazama, et al., J. Nucl. Sci. Technol., **43**, p.908 (2006).

[2] K.Okumura, et al., 'SRAC2006: A Comprehensive Neutronics Calculation Code System,' JAEA-Data/Code 2007-004, (2007).

[3] G.Chiba, et al., 'Benchmark Test of Evaluated Nuclear Data Files for Fast Reactor Neutronics Application,' JAEA-Research 2007-051, (2007)[in Japanese].

[4] G.Chiba, Y.Shimazu, J. Nucl. Sci. Technol., **44**, p.1526 (2007).

[5] G.Chiba, Proc. of spring Mtg. of AESJ, Nagoya, (2007)[in Japanese].

[6] N.Sugimura, A.Yamamoto, J. Nucl. Sci. Technol., **44**, p.958 (2007).

[7] A.Yamamoto, et al., J. Nucl. Sci. Technol., **39**, p.900 (2002).

[8] M.L.Williams, CRC Handbook of Nuclear Reactor Calculations, Vol.3, p.63, CRC Press (1986).

Appendix: Participants Lists

AKINO Fujiyoshi			MAKII Hiroyuki	JAEA
ANDO Yoshihira	JNES		MARUYAMA Hiromi	HGNE
ANDOH Masaki	JAEA		MATSUOKA Masao	NFI
ASAMI Mitsufumi	NMRI		MIZUMOTO Motoharu	Tokyo Inst. of Tech.
CHIBA Go	JAEA		MURATA Toru	
CHIBA Satoshi	JAEA		NAGAI Yasuki	
FUKAHORI Tokio	JAEA		NAGAYA Yasunobu	JAEA
FUKUI Yoshinori	Kyushu Univ.		NAKAGAWA Tsuneo	JAEA
FURUTA Masataka	Nagoya Univ.		NAKAJIMA Ken	Kyoto Univ.
FURUTAKA Kazuyoshi	JAEA		NAKAMURA Shoji	JAEA
GOKO Shinji	JAEA		NIITA K	RIST
HAGURA Naoto	Musashi-tech		OHNISHI Seiki	JAEA
HARADA Hideo	JAEA		OKADA Koichi	JAEA
HARADA Masahide	JAEA		OKUMURA Keisuke	JAEA
HAYASHI Masateru	Kyushu Univ.		OSHITA Hironori	JAEA
HIRANO Go	TEPSYS		OTSUKA Naohiko	JAEA
ICHIHARA Akira	JAEA		SAITO Kosuke	JAEA
IGASHIRA Masayuki	Tokyo Inst. of Tech.		SASAKI Kenji	MFBR
IKEHARA Tadashi	GNF-J		SATO Satoshi	JAEA
INOSHITA Sunya	JAEA		SEGAWA Mariko	JAEA
ISHII Kazuya	Hitachi Ltd.		SHIBATA Keiichi	JAEA
ISHIKAWA Makoto	JAEA		SUGITA Takeshi	SSL
ITOH Takuya	NFI		Sun Weili	IAPCM
IWAMOTO Nobuyuki	JAEA		SUYAMA Kenya	JAEA
IWAMOTO Osamu	JAEA		TAHARA Yoshihisa	EDC
KAISE Yoichiro	MFBR		TAKAHASHI Hiroshi	
KATABUCHI Tatsuya	Tokyo Inst. of Tech.		TAKAKURA Kosuke	JAEA
KATAKURA Jun-ichi	JAEA		TAKANO Hideki	NAIS
KIMURA Atsushi	JAEA		TOISHIGAWA Akiko	GNF-J
KIN Tadahiro	JAEA		UOZUMI Yusuke	Kyushu Univ.
KIYANAGI Yoshiaki	Hokkaido Univ.		WAKABAYASHI G.	Kyushu Univ.
KOBA Yusuke	Kyushu Univ.		WATANABE Yukinobu	Kyushu Univ.
KOBAYASHI K..			YAKATA Tomoyoshi	Univ. of Tokyo
KOIZUMI Mitsuo	JAEA		YAMAUCHI Michinori	JAEA
KONNO Chikara	JAEA		Ye Tao	Kyushu Univ.
KOSAKO Kazuaki	SHIMZ		YOKOYAMA Kenji	JAEA
KOURA Hiroyuki	JAEA		YOSHIDA Tadashi	MIT
KUNIEDA Satoshi	JAEA		ZUKERAN Atsushi	NAIS

This is a blank page.

国際単位系（SI）

表１．SI 基本単位

基本量	SI 基本単位 名称	記号
長　　さ	メートル	m
質　　量	キログラム	kg
時　　間	秒	s
電　　流	アンペア	A
熱力学温度	ケルビン	K
物　質　量	モル	mol
光　　度	カンデラ	cd

表２．基本単位を用いて表されるSI組立単位の例

組立量	SI 基本単位 名称	記号
面　　　　積	平方メートル	m^2
体　　　　積	立法メートル	m^3
速さ，速度	メートル毎秒	m/s
加　速　度	メートル毎秒毎秒	m/s^2
波　　　数	毎メートル	m^{-1}
密度（質量密度）	キログラム毎立法メートル	kg/m^3
質量体積（比体積）	立法メートル毎キログラム	m^3/kg
電　流　密　度	アンペア毎平方メートル	A/m^2
磁界の強さ	アンペア毎メートル	A/m
（物質量の）濃度	モル毎立方メートル	mol/m^3
輝　　　　度	カンデラ毎平方メートル	cd/m^2
屈　折　率	（数の）1	1

表５．SI 接頭語

乗数	接頭語	記号	乗数	接頭語	記号
10^{24}	ヨタ	Y	10^{-1}	デシ	d
10^{21}	ゼタ	Z	10^{-2}	センチ	c
10^{18}	エクサ	E	10^{-3}	ミリ	m
10^{15}	ペタ	P	10^{-6}	マイクロ	μ
10^{12}	テラ	T	10^{-9}	ナノ	n
10^{9}	ギガ	G	10^{-12}	ピコ	p
10^{6}	メガ	M	10^{-15}	フェムト	f
10^{3}	キロ	k	10^{-18}	アト	a
10^{2}	ヘクト	h	10^{-21}	ゼプト	z
10^{1}	デカ	da	10^{-24}	ヨクト	y

表３．固有の名称とその独自の記号で表されるSI組立単位

組立量	SI 組立単位 名称	記号	他のSI単位による表し方	SI基本単位による表し方
平　面　角	ラジアン[a]	rad		$m \cdot m^{-1}=1$ [b]
立　体　角	ステラジアン[a]	sr[c]		$m^2 \cdot m^{-2}=1$ [b]
周　波　数	ヘルツ	Hz		s^{-1}
力	ニュートン	N		$m \cdot kg \cdot s^{-2}$
圧力，応力	パスカル	Pa	N/m^2	$m^{-1} \cdot kg \cdot s^{-2}$
エネルギー，仕事，熱量	ジュール	J	$N \cdot m$	$m^2 \cdot kg \cdot s^{-2}$
工率，放射束	ワット	W	J/s	$m^2 \cdot kg \cdot s^{-3}$
電荷，電気量	クーロン	C		$s \cdot A$
電位差（電圧），起電力	ボルト	V	W/A	$m^2 \cdot kg \cdot s^{-3} \cdot A^{-1}$
静　電　容　量	ファラド	F	C/V	$m^{-2} \cdot kg^{-1} \cdot s^4 \cdot A^2$
電　気　抵　抗	オーム	Ω	V/A	$m^2 \cdot kg \cdot s^{-3} \cdot A^{-2}$
コンダクタンス	ジーメンス	S	A/V	$m^{-2} \cdot kg^{-1} \cdot s^3 \cdot A^2$
磁　　　束	ウェーバ	Wb	$V \cdot s$	$m^2 \cdot kg \cdot s^{-2} \cdot A^{-1}$
磁　束　密　度	テスラ	T	Wb/m^2	$kg \cdot s^{-2} \cdot A^{-1}$
インダクタンス	ヘンリー	H	Wb/A	$m^2 \cdot kg \cdot s^{-2} \cdot A^{-2}$
セルシウス温度	セルシウス度[d]	℃		K
光　　　束	ルーメン	lm	$cd \cdot sr$ [c]	$m^2 \cdot m^{-2} \cdot cd=cd$
照　　　度	ルクス	lx	lm/m^2	$m^2 \cdot m^{-4} \cdot cd=m^{-2} \cdot cd$
（放射性核種の）放射能	ベクレル	Bq		s^{-1}
吸収線量，質量エネルギー分与，カーマ	グレイ	Gy	J/kg	$m^2 \cdot s^{-2}$
線量当量，周辺線量当量，方向性線量当量，個人線量当量，組織線量当	シーベルト	Sv	J/kg	$m^2 \cdot s^{-2}$

(a)ラジアン及びステラジアンの使用は、同じ次元であっても異なった性質をもった量を区別するときの組立単位の表し方として利点がある。組立単位を形作るときのいくつかの用例は表４に示されている。

(b)実際には、使用する時には記号rad及びsrが用いられるが、習慣として組立単位としての記号“1”は明示されない。

(c)測光学では、ステラジアンの名称と記号srを単位の表し方の中にそのまま維持している。

(d)この単位は、例としてミリセルシウス度m℃のようにSI接頭語を伴って用いても良い。

表６．国際単位系と併用されるが国際単位系に属さない単位

名称	記号	SI 単位による値
分	min	1 min=60s
時	h	1h =60 min=3600 s
日	d	1 d=24 h=86400 s
度	°	1°＝(π/180) rad
分	′	1’=(1/60)°＝(π/10800) rad
秒	”	1”=(1/60)’＝(π/648000) rad
リットル	l、L	1l=1 $dm^3=10^{-3}m^3$
トン	t	$1t=10^3$ kg
ネーパ	Np	1Np=1
ベル	B	1B=(1/2)ln10(Np)

表７．国際単位系と併用されこれに属さない単位で SI単位で表される数値が実験的に得られるもの

名称	記号	SI 単位であらわされる数値
電　子　ボ　ル　ト	eV	$1eV=1.60217733(49) \times 10^{-19}J$
統一原子質量単位	u	$1u=1.6605402(10) \times 10^{-27}kg$
天　文　単　位	ua	$1ua=1.49597870691(30) \times 10^{11}m$

表８．国際単位系に属さないが国際単位系と併用されるその他の単位

名称	記号	SI 単位であらわされる数値
海　　　里		1海里=1852m
ノ　ッ　ト		1ノット＝1 海里毎時＝(1852/3600)m/s
ア　ー　ル	a	1a=1 $dam^2=10^2m^2$
ヘクタール	ha	1 ha=1 $hm^2=10^4m^2$
バ　ー　ル	bar	1 bar=0.1MPa=100kPa=1000hPa=10^5Pa
オングストローム	Å	1 Å=0.1nm=10^{-10}m
バ　ー　ン	b	1 b=100$fm^2=10^{-28}m^2$

表４．単位の中に固有の名称とその独自の記号を含むSI組立単位の例

組立量	SI 組立単位 名称	記号	SI 基本単位による表し方
粘　　　　度	パスカル秒	$Pa \cdot s$	$m^{-1} \cdot kg \cdot s^{-1}$
力のモーメント	ニュートンメートル	$N \cdot m$	$m^2 \cdot kg \cdot s^{-2}$
表　面　張　力	ニュートン毎メートル	N/m	$kg \cdot s^{-2}$
角　速　度	ラジアン毎秒	rad/s	$m \cdot m^{-1} \cdot s^{-1}=s^{-1}$
角　加　速　度	ラジアン毎平方秒	rad/s^2	$m \cdot m^{-1} \cdot s^{-2}=s^{-2}$
熱流密度，放射照度	ワット毎平方メートル	W/m^2	$kg \cdot s^{-3}$
熱容量，エントロピー	ジュール毎ケルビン	J/K	$m^2 \cdot kg \cdot s^{-2} \cdot K^{-1}$
質量熱容量（比熱容量），質量エントロピー	ジュール毎キログラム毎ケルビン	$J/(kg \cdot K)$	$m^2 \cdot s^{-2} \cdot K^{-1}$
質量エネルギー（比エネルギー）	ジュール毎キログラム	J/kg	$m^2 \cdot s^{-2}$
熱　伝　導　率	ワット毎メートル毎ケルビン	$W/(m \cdot K)$	$m \cdot kg \cdot s^{-3} \cdot K^{-1}$
体　積　エネルギー	ジュール毎立方メートル	J/m^3	$m^{-1} \cdot kg \cdot s^{-2}$
電　界　の　強　さ	ボルト毎メートル	V/m	$m \cdot kg \cdot s^{-3} \cdot A^{-1}$
体　積　電　荷	クーロン毎立方メートル	C/m^3	$m^{-3} \cdot s \cdot A$
電　気　変　位	クーロン毎平方メートル	C/m^2	$m^{-2} \cdot s \cdot A$
誘　電　率	ファラド毎メートル	F/m	$m^{-3} \cdot kg^{-1} \cdot s^4 \cdot A^2$
透　磁　率	ヘンリー毎メートル	H/m	$m \cdot kg \cdot s^{-2} \cdot A^{-2}$
モルエネルギー	ジュール毎モル	J/mol	$m^2 \cdot kg \cdot s^{-2} \cdot mol^{-1}$
モルエントロピー，モル熱容量	ジュール毎モル毎ケルビン	$J/(mol \cdot K)$	$m^2 \cdot kg \cdot s^{-2} \cdot K^{-1} \cdot mol^{-1}$
照射線量（X線及びγ線）	クーロン毎キログラム	C/kg	$kg^{-1} \cdot s \cdot A$
吸　収　線　量　率	グレイ毎秒	Gy/s	$m^2 \cdot s^{-3}$
放　射　強　度	ワット毎ステラジアン	W/sr	$m^4 \cdot m^{-2} \cdot kg \cdot s^{-3}=m^2 \cdot kg \cdot s^{-3}$
放　射　輝　度	ワット毎平方メートル毎ステラジアン	$W/(m^2 \cdot sr)$	$m^2 \cdot m^{-2} \cdot kg \cdot s^{-3}=kg \cdot s^{-3}$

表９．固有の名称を含むCGS組立単位

名称	記号	SI 単位であらわされる数値
エ　ル　グ	erg	1 $erg=10^{-7}$ J
ダ　イ　ン	dyn	1 $dyn=10^{-5}N$
ポ　ア　ズ	P	1 P=1 $dyn \cdot s/cm^2=0.1Pa \cdot s$
ス　ト　ー　ク　ス	St	1 St $=1cm^2/s=10^{-4}m^2/s$
ガ　ウ　ス	G	1 G $\triangleq 10^{-4}T$
エルステッド	Oe	1 Oe $\triangleq (1000/4\pi)A/m$
マ　ク　ス　ウ　ェ　ル	Mx	1 Mx $\triangleq 10^{-8}Wb$
ス　チ　ル　ブ	sb	1 sb $=1cd/cm^2=10^4cd/m^2$
ホ　ト	ph	1 $ph=10^4lx$
ガ　ル	Gal	1 Gal $=1cm/s^2=10^{-2}m/s^2$

表10．国際単位に属さないその他の単位の例

名称	記号	SI 単位であらわされる数値
キ　ュ　リ　ー	Ci	1 Ci=3.7×10^{10}Bq
レ　ン　ト　ゲ　ン	R	1 R = 2.58×10^{-4}C/kg
ラ　　　ド	rad	1 rad=1cGy=10^{-2}Gy
レ　　　ム	rem	1 rem=1 cSv=10^{-2}Sv
X　線　単　位		1X unit=1.002×10^{-4}nm
ガ　ン　マ	γ	1 γ=1 nT=10^{-9}T
ジ　ャ　ン　ス　キ　ー	Jy	1 Jy=$10^{-26}W \cdot m^{-2} \cdot Hz^{-1}$
フ　ェ　ル　ミ		1 fermi=1 fm=10^{-15}m
メートル系カラット		1 metric carat = 200 mg = 2×10^{-4}kg
ト　　　ル	Torr	1 Torr = (101 325/760) Pa
標　準　大　気　圧	atm	1 atm = 101 325 Pa
カ　ロ　リ　ー	cal	
ミ　ク　ロ　ン	μ	1 μ =1μm=10^{-6}m